

## ABSTRACT

HADER, JOHN DANIEL. Propagating, Cloud-eroding Boundaries in Southeast Atlantic Marine Stratocumulus. (Under the direction of Sandra Yuter).

Marine stratocumulus clouds form large, persistent cloud decks over the eastern subtropical oceans. These low clouds have a net cooling effect on Earth's radiation budget. Various physical processes change the areal extent of marine stratocumulus on annual, multi-day, and daily timescales. The southeast Atlantic exhibits a lower average cloud fraction in March-April-May than occurs in any season in the other two marine stratocumulus regions in the southeast Pacific and northeast Pacific. We present observations of a previously undocumented modulator of cloud fraction on multiday timescales in the southeast Atlantic that may account for the low seasonal cloud fraction. Sharp, westward-moving cloudiness transitions occur frequently in the southeast Atlantic marine stratocumulus, causing complete or partial erosion of the cloud deck that extends for hundreds to roughly one thousand kilometers in length. The cloudiness boundaries first become visible in infrared satellite imagery immediately adjacent to the coast around local midnight and move westward, roughly perpendicular to the mean southerly flow, at roughly  $10 \text{ ms}^{-1}$ . High resolution visible satellite imagery reveals that the transition to reduced cloudiness occurs over spatial scales of a few to a few tens of kilometers and can be accompanied by wave-like features parallel to the cloud boundary. These westward-moving cloud boundaries have a distinct annual frequency of occurrence with a peak in May (roughly 20 per month) and a minimum in January (roughly 1 per month). The presence of wave-like features with the boundaries and their movement perpendicular to the mean flow strongly suggest the cloud erosion is caused by a gravity wave rather than advection. The timing, direction of motion, and

associated synoptic patterns of these gravity waves contrast sharply with the characteristics of previously documented gravity waves in the southeast Pacific marine stratocumulus. Comparison to other coastally-generated gravity waves, that generate rather than erode cloud, suggests that a possible triggering mechanism for the gravity waves may be the strong land breeze and/or downslope flow off of the high coastal terrain interacting with the stable marine boundary layer. An initial analysis of available sounding and reanalysis data suggests, but does not conclusively show, that the cloud deck may be more susceptible to erosion by entrainment of warm and dry free tropospheric air with the passage of the gravity wave in May than in January.

© Copyright 2016 John Daniel Hader

All Rights Reserved

Propagating, Cloud-eroding Boundaries in Southeast Atlantic Marine Stratocumulus

by  
John Daniel Hader

A thesis submitted to the Graduate Faculty of  
North Carolina State University  
in partial fulfillment of the  
requirements for the degree of  
Master of Science

Marine, Earth, and Atmospheric Sciences

Raleigh, North Carolina

2016

APPROVED BY:

---

Dr. Sandra Yuter  
Committee Chair

---

Dr. Walter Robinson

---

Dr. Matthew Parker

---

Dr. David Mechem

## ACKNOWLEDGMENTS

The author wishes to express many thanks to Dr. Sandra Yuter for her mentoring and all of her time, effort, and support in the production of this thesis. The author also wishes to thank the members of the thesis committee: Dr. David Mechem, Dr. Matthew Parker, and Dr. Walter Robinson for their useful discussion and input regarding the thesis. Dr. Matthew Miller provided large amounts of technical support as well as several of the figures, and is greatly thanked. The members of the Cloud and Precipitation Processes and Patterns Group are also thanked for their support and help throughout the project, including several (Michael Tai Bryant, Edward Chan, Levi Lovell, Dr. Matthew Miller, Emma Scott, and Laura Tomkins) who aided in the manual detection of the westward-moving cloud eroding boundaries for the annual frequency analysis. Dr. Casey Burleyson is also thanked for providing useful discussion and follow-up research support. Matthew Wilbanks also provided useful discussion throughout the research process, and is thanked for his contribution. Thanks also go to Dr. Roland Vogt of the University of Basel for providing the meteorological data from Gobabeb, Namibia. The author also thanks Yemi Adebisi for supplying the St. Helena sounding data in an easy-to-use format. The author also wishes to thank the crew of the International Space Station, as well as Mike Trenchard of the Earth Science and Remote Sensing Unit, NASA Johnson Space Centers, for their work in acquiring the images of the cloud boundary aboard the International Space Station presented in the thesis. This work was funded by DOE ASR Grant: DE-SC0006701.

## TABLE OF CONTENTS

LIST OF TABLES .....	v
LIST OF FIGURES.....	vi
INTRODUCTION .....	1
DATA AND METHODS.....	4
Satellite data .....	4
Sharp Cloud Boundary Climatology .....	5
Reanalysis data.....	7
Surface and upper air obs.....	9
RESULTS.....	13
Morphology of cloud erosion along propagating boundaries .....	13
Synoptic scale features.....	13
Small scale features along the boundaries .....	18
Abrupt transitions.....	18
Small wavelength bands parallel to main propagating boundaries...20	
Small wavelength cloud bands not parallel to main propagating boundaries .....	21
Cloud boundary monthly frequency .....	21
Large scale conditions for the maximum and minimum cloud boundary months .....	22
Atmospheric profiles from St. Helena Island .....	27
DISCUSSION .....	29
Comparison to known marine low cloud gravity waves.....	29
Gravity waves in central U.S.....	32
Discussion of possible triggering mechanisms .....	32
Additional considerations for gravity wave versus advection .....	34
Cloud erosion .....	38
CONCLUSIONS.....	40
REFERENCES .....	43
Appendices .....	49
Appendix A.....	50
Appendix B.....	52

## LIST OF TABLES

Table 1.1 Various known transitions in marine cloudiness .....	53
Table 3.1 Estimated radiative impact of various degrees of cloud erosion .....	54
Table 4.1 Intrinsic gravity wave phase speeds for various parameter values .....	55
Table 4.2 Estimated density current speeds .....	56

## LIST OF FIGURES

Figure 1.1 Marine stratocumulus region inter-seasonal variability .....	57
Figure 1.2 Referenced studies' analysis regions.....	58
Figure 2.1 Hovmöller diagram analysis region .....	59
Figure 2.2 Manual cloud boundary climatology analysis region.....	60
Figure 2.3 Examples of categorization of cloud scene pairs .....	61
Figure 2.4 Demonstration of lower tropospheric stability variability analysis .....	62
Figure 2.5 Schematic of stable layer top and bottom identification .....	63
Figure 3.1 Corrected reflectance examples of complete clearing 1 .....	64
Figure 3.2 Corrected reflectance examples of complete clearing 2 .....	65
Figure 3.3 Corrected reflectance examples of partial clearing 1.....	66
Figure 3.4 Corrected reflectance examples of partial clearing 2.....	67
Figure 3.5 Meteosat visible stills close-up .....	68
Animation 3.6 Partial erosion of cloud.....	52
Animation 3.7 Regeneration of cloud .....	52
Animation 3.8 Partial erosion and regeneration of cloud.....	52
Animation 3.9 Mean flow-tracked cloud boundary propagation.....	52
Figure 3.10 Brightness temperature nocturnal coastal detachment stills.....	69
Animation 3.11 Brightness temperature nocturnal coastal detachment example 1.....	52
Animation 3.12 Brightness temperature nocturnal coastal detachment example 2.....	52
Figure 3.13 May versus January 2014 Hovmöller diagrams.....	70
Animation 3.14 Visible cloud boundary close-up: Rapid removal of cloud .....	52
Animation 3.15 Visible cloud boundary close-up: Evidence against open cells.....	52
Figure 3.16 Drizzle detection in vicinity of sharp cloud boundary .....	71
Figure 3.17 Sharp cloud boundary images from International Space Station .....	72
Animation 3.18 Southward moving gravity waves.....	52
Animation 3.19 Gravity waves in southeast Atlantic marine stratocumulus region.....	52
Figure 3.20 Monthly histogram of westward-moving cloud boundary days .....	73
Figure 3.21 Annual cycle in Southeast Atlantic total cloud fraction .....	74
Figure 3.22 May versus January sea surface temperatures 2000 through 2011.....	75
Animation 3.23 Monthly MERRA sea level pressure and 1000 hPa winds .....	52
Animation 3.24 Monthly MERRA estimated inversion strength .....	52
Animation 3.25 Monthly MERRA 700 hPa pressure vertical velocity.....	52
Figure 3.26 May versus January MERRA reanalysis sea level pressure and 1000 hPa winds .....	76
Figure 3.27 MERRA reanalysis composites of boundary vs. non-boundary days .....	77
Figure 3.28 May versus January MERRA reanalysis estimated inversion strength.....	78
Figure 3.29 May versus January MERRA reanalysis omega 700 hPa .....	79
Figure 3.30 MERRA reanalysis annual cycle in EIS and omega 700 .....	80
Figure 3.31 Drizzle frequency austral fall versus summer .....	81
Figure 3.32 May versus January inversion height histograms.....	82
Figure 3.33 May versus January average inversion relative soundings.....	83
Figure 3.34 Annual Brunt Väisälä frequency and Richardson number .....	84
Figure 4.1 Upsidence wave diagram .....	85

Figure 4.2 Northwestern Australia cloud line triggering mechanism.....	86
Figure 4.3 Diurnal variability in coastal winds .....	87
Figure 4.4 Southwestern Africa coastal terrain .....	88
Figure 4.5 Corrected reflectance propagating cloud boundary near Gobabeb, Namibia .....	89
Animation 4.6 Brightness temperature propagating cloud boundary near Gobabeb, Namibia.....	52
Figure 4.7 Surface meteorological data around time of cloud boundary near Gobabeb, Namibia.....	90
Figure 4.8 Reference map for wind direction analysis.....	91
Figure 4.9 Wind direction analysis .....	92
Figure 4.10 MODIS aerosol optical depth around cloud boundaries.....	93
Figure 4.11 Hypothesized gravity wave triggering schematic.....	94
Figure B1 Yes, no, and maybe cloud boundary days histogram .....	95

## **1.) Introduction**

Marine low clouds have a net cooling effect on Earth's radiation budget since they reflect more incoming shortwave radiation than they emit at infrared wavelengths (Hartmann et al., 1992). An increase in the long-term mean areal coverage of these clouds would act to offset warming due to anthropogenic carbon dioxide while a decrease in marine low cloud area would exacerbate warming. Marine stratocumulus cloud decks are located over the eastern portions of subtropical ocean basins where cool, equatorward-moving water coincides with the descending branch of the Hadley cell (Klein and Hartmann, 1993). Despite intensive modeling and observational work in the last few decades, numerical models still struggle to reproduce key characteristics of the marine stratocumulus clouds with fidelity (e.g. Wyant et al., 2010; O'Dell et al., 2008; Medeiros et al. 2012; Zheng and Li., 2013) and low marine cloud feedbacks remain a large source of uncertainty in climate projections (Bony et al.2006; IPCC report 2013).

Cloud fraction is determined over a specific area and time and represents how much of an area is covered by clouds. In marine stratocumulus regions, the cloud fraction exhibits well-documented cycles of variability on diurnal, multi-day, seasonal, and inter-annual time scales (e.g. Klein and Hartmann, 1993; de Szoeke et al., 2016; Burleyson and Yuter 2015a & b). Recent work by de Szoeke et al. (2016), found that cloudiness variance at multi-day (~3-50 days) timescales exceeds the seasonal variance in the subtropical southeast Atlantic and northeast Pacific and is substantial, but slightly lower than the seasonal magnitude, in the southeast Pacific.

The amplitude of variation of cloud fraction at different time scales varies as a function of geographical region. In a comparison of satellite infrared (IR) derived cloud fractions among the northeast Pacific, southeast Pacific, and southeast Atlantic, Burleyson and Yuter (2015b) found that the southeast Atlantic had the largest interseasonal variability in the diurnal cycle of cloud fraction. The highest average diurnal cloud fraction occurred in September/October/November and the lowest in March/April/May (Figure 1.1; see also Figure 1.2 for a reference map of their analysis region). Compared to the minimum season in the other two basins, the southeast

Atlantic has the lowest diurnally-averaged cloud fraction (compare panels a, b, and c of Figure 1.1).

Superimposed on the diurnal and seasonally forced variations in marine stratocumulus are several types of sub-daily, daily, and multi-day transitions in mesoscale cloud fraction (Table 1.1). Stevens et al. (2005) documented pockets of open-cellular clouds surrounded by closed-cellular clouds in marine stratocumulus. They found these regions of reduced cloud fraction to be associated with precipitation and to persist in the cloud field for time scales on the order of 10 hours. Pockets of open cells were also seen to be associated with ‘rifts’ in marine stratocumulus clouds; large areas of reduced cloud fraction that can extend up to thousands of kilometers and persist for days (Sharon et al., 2006). Both of these features were found to advect with the mean wind in the boundary layer (Stevens et al., 2005; Sharon et al., 2006). Cloud clearing in regions over 100 kilometers wide is observed to move equatorward with the mean flow in the northeast Pacific immediately along the west coast of the United States at a rate  $\leq 10 \text{ ms}^{-1}$  (Kloesel, 1992; Crosbie et al., 2016). These clearings are likely the result of changes in the position of the subtropical high and the direction of the mean flow relative to the adjacent continent. Crosbie et al. (2016) suggest that coastal mesoscale dynamics (i.e. land/sea breeze circulations) may also play into the erosion of the cloud.

Two kinds of gravity waves have been previously identified as modulators of cloudiness and liquid water path in the marine stratocumulus clouds of the southeast Pacific. Neither wave propagates in the same direction as the mean flow. The ‘upsidence’ wave, first described in a modeling study by Garreaud and Muñoz (2004), is a gravity wave associated with the upward motion caused by diurnal heating of the Andes. An area of upward motion moves away from the South American coast around 1700 LT and propagates southwestward over the marine stratocumulus (see Section 4.1 for further discussion). Gravity wave trains, first identified in satellite observations by Allen et al. (2012), originate with sharply divergent flows in the subtropical jet and propagate north and east against the mean flow. Outside of the subtropical marine stratocumulus cloud decks, gravity waves are known to create cloud lines in several coastal regions. Perhaps the most well-known example of a coastally-generated gravity

wave is the Morning Glory of the Gulf of Carpentaria along the northeast coast of Australia (e.g. Clarke, 1972; Clarke et al. 1981; Christie, 1992; Goler and Reeder, 2004). The interaction of the colliding east coast and west coast sea breezes along the Cape York Peninsula can generate a bore that propagates along the marine boundary layer to the south and east (e.g. Goler and Reeder, 2004). The upward motion associated with the leading edges and undulations of these bores can trigger the formation of cloud lines (e.g. Clarke, 1972; Clarke et al. 1981; Christie, 1992). A similar phenomenon has been documented along the northwest coast of Australia by Birch and Reeder (2013), where the land breeze/accelerating southeasterly flow impinging upon the sea breeze and marine stable layer generates undulations that propagate north and west from the coast. As with the Morning Glories, the crests of these gravity waves can generate sets of linear cloud features. Da Silva and Magalhães (2009) and Magalhães et al. (2011) documented marine boundary layer gravity wave trains in the Mozambique Channel and the Red Sea. In both of these regions, coastal diurnal wind circulations were proposed as possible wave-triggering mechanisms. In all of these marine gravity wave cases, the wave guide for the propagating disturbances is the inversion at the top of the stable atmospheric boundary layer.

In this study, we examine previously undocumented westward-moving sharp transitions in cloudiness in the southeast Atlantic that can be more than 1,000 km long. We present evidence that strongly suggests that these instances of westward-moving cloud erosion are the result of coastally-generated gravity waves. The cloud erosion happens along exceedingly sharp boundaries and the disturbance can either partially or completely remove cloud over a time span of less than 15 minutes. Cloud recovery can take up to approximately one day. Our observations imply that diurnal and multi-day processes originating external to the marine stratocumulus cloud deck are playing an important role in modulating cloud fraction on seasonal time scales in the southeast Atlantic.

## **2.) Data and methods**

### **2.1. Satellite data**

We use both polar-orbiting and geosynchronous satellite data in our analysis. A primary data set is the relatively high spatial resolution Moderate Resolution Imaging Spectroradiometer (MODIS) corrected reflectance true color data from the NASA Aqua and Terra satellites. These data are obtained from NASA's Earth Observing System Data and Information System (EOSDIS) Worldview tool (<https://worldview.earthdata.nasa.gov>). The MODIS instrument has a swath width of 2330 km. The corrected reflectance data have an approximate pixel size of 250 meters. The sun-synchronous orbits of the Terra and Aqua satellites result in data over the subtropical southeast Atlantic twice daily during daylight hours at roughly 10:30 LT (Terra) and 13:30 LT (Aqua; see <http://modis.gsfc.nasa.gov/about/specifications.php> and [https://earthdata.nasa.gov/files/MODIS\\_True\\_Color.pdf](https://earthdata.nasa.gov/files/MODIS_True_Color.pdf)). Note that along the southwestern African coast, the local time is one hour ahead of UTC, while between a few degrees longitude west of the southwestern African coast and St. Helena Island (~ -5.7° longitude) the local time aligns with UTC. The small discrepancy between UTC time and local time in the region of interest is generally ignored in this study.

To observe the time-varying small scale features of the marine stratocumulus erosion during daylight hours, High Rate Spinning Enhanced Visible and IR Imager (SEVIRI) Level 1.5 visible satellite data from the Meteosat 10 geosynchronous satellite (centered at 0° latitude, 0° longitude) were obtained from the European Organization for the Exploitation of Meteorological Satellites (EUMETSAT; see [http://navigator.eumetsat.int/discovery/Start/DirectSearch/DetailResult.do?f\(r0\)=EO:EUM:DAT:MSG:HRSEVIRI](http://navigator.eumetsat.int/discovery/Start/DirectSearch/DetailResult.do?f(r0)=EO:EUM:DAT:MSG:HRSEVIRI) ). Full-Earth scans are available roughly every 15 minutes with a pixel size between 3.1 and 4 km in the region of interest (see MSG Level 1.5 Image Data Format Description: <http://www.eumetsat.int/website/home/Data/TechnicalDocuments/index.html>, Müller et al., 2013). Three-channel visible images using the 0.6  $\mu\text{m}$ , 0.8  $\mu\text{m}$ , and 1.6  $\mu\text{m}$  channels were retrieved from the EUMET Earth Observing Portal for this study.

Half-hourly global merged infrared (IR) satellite data were obtained from NASA's Goddard Earth Sciences Data and Information Services Center (GES DISC: see [http://disc.sci.gsfc.nasa.gov/precipitation/data-holdings/Globally\\_merged\\_IR.shtml](http://disc.sci.gsfc.nasa.gov/precipitation/data-holdings/Globally_merged_IR.shtml)). This merged IR product is created by combining brightness temperature data from multiple geostationary satellites into a globally complete brightness temperature data set on a uniform global grid with a pixel size of  $\sim 4$  km (Janowiak et al., 2001). The geosynchronous IR data are used to examine the brightness temperatures over the southeast Atlantic and southern Africa throughout the diurnal cycle.

In order to analyze multiple, successive days of IR satellite data, Hovmöller diagrams of the IR satellite data were generated for the region between  $-20^{\circ}$  and  $-10^{\circ}$  latitude and  $-6.0^{\circ}$  and  $13.0^{\circ}$  longitude (Figure 2.1). Brightness temperature values within the analysis region were averaged meridionally for each 30-min time step. The Hovmöller diagrams show the time-varying meridional average of brightness temperature for the region. The plots are broken up into periods of 10 days for display. These Hovmöller diagrams are used to estimate the westward speed of the cloudiness transitions, and these speeds are compared to speeds estimated from the corresponding Aqua and Terra corrected reflectance images.

Satellite-derived sea surface temperature (SST) data were obtained from Remote Sensing Systems (<http://www.remss.com/measurements/sea-surface-temperature>). We use the optimally interpolated microwave-only daily SST data product which employs measurements from the TMI, AMSR-E, AMSR2, and WindSat satellites. These measurements are blended together using the interpolation scheme outlined in Reynolds and Smith (1994) resulting in a pixel size of roughly 25 km (see <http://www.remss.com/measurements/sea-surface-temperature/oisst-description> for full details). The daily maps of interpolated SSTs are used to calculate multi-year averages on a monthly basis.

## **2.2. Sharp cloud boundary climatology**

A sharp cloud boundary was defined as an abrupt (on the order of a few to a few tens of kilometers) transition between visually obvious regions of cloudiness and

decreased cloudiness (or complete clearing). To fit our definition of a westward-moving cloud boundary, the boundary had to be at least  $\sim 200$  km in length ( $2^\circ$  latitude/longitude) and have a predominantly westward component of motion. In accordance with the latter criterion, most of the boundaries were oriented roughly in a north-south direction.

We used visual examination of pairs of satellite images to tabulate days on which at least one westward-moving, cloud-eroding boundary occurred for the period from 08 May 2012 through 01 November 2015 in the region bounded by  $-10^\circ$  and  $-20^\circ$  latitude and  $0^\circ$  and  $12^\circ$  degrees longitude (see Figure 2.2 for a reference map of this region). The pairs of MODIS Aqua and Terra corrected reflectance images for each day (subsequently referred to as a 'cloud scene pair') were visually examined by a total of seven analysts. John Hader trained each person on the specific visual cues required to identify and categorize the boundaries and supervised their practice on real examples. Most individuals analyzed 10-12 months of cloud scene pairs. To mitigate potential classification biases among individual analysts, cloud scene pairs for each day were analyzed by two people. The Terra and Aqua overpasses were analyzed in tandem to ascertain the movement of the boundary between the two overpasses ( $\sim 3$  hours apart). The days (cloud scene pairs) were categorized as definitely having a sharp cloud boundary present ('yes'), definitely not having a sharp cloud boundary present ('no'), or possibly having a sharp cloud boundary present ('maybe'). In instances where the swath of the MODIS instrument missed a portion of the cloud deck, a 'yes', 'no', or 'maybe' decision was still made with the available information.

After this first round of cloud scene pair categorization, the two decisions for each cloud scene were compared. Scenes for which both analysts agreed on either a 'yes' or 'no' categorization were placed into the respective categories. For instances in which the analyzers disagreed or at least one analyzer indicated a 'maybe' categorization, the cloud scene pair was put into a temporary 'maybe' category. These 'maybe' cloud scene pairs were subsequently analyzed by John Hader and Dr. Matthew Miller (a satellite data expert) to see if a final decision could be reached on their classification. Based on the discussion between the experts, if the scene clearly either did or did not have a

westward-moving cloud boundary, it was placed into the respective category. If a definitive decision could still not be made, the scene remained in the ‘maybe’ category. Figure 2.3 illustrates examples of cloud scene pairs that were categorized as ‘yes’, ‘no’, and ‘maybe’.

For the roughly 3 ½ year data set, the frequency occurrence of ‘yes’ classified days was used to generate a daily probability for a given calendar month. This daily probability was used to generate an average number of days per calendar month on which ‘yes’ classified days occurred. We consider the ‘yes’ subset of cloud scene pairs a robust underestimate of the actual number of cloud boundaries since it does not take into account multiple boundaries occurring on a single day or the ‘maybe’ cloud boundary category. Note that while qualitatively different, subjective analysis of satellite images to determine the occurrence frequency of gravity waves has previously been done many times in the literature (e.g. Désalmand et al., 2003; da Silva and Magalhães, 2009; Magalhães et al. 2011; Birch and Reeder, 2013).

### 2.3 Reanalysis data

Data from the Modern-Era Retrospective Analysis for Research and Application (MERRA; Rienecker et al., 2011) were obtained through NASA’s GES DISC. 3-hourly instantaneous fields were analyzed, with a grid spacing of 0.5° latitude by 0.625° longitude, for the period 01 January 2000 through 31 December 2015. Monthly averages of sea level pressure, 1000 hPa winds, 700 hPa pressure vertical velocity, and estimated inversion strength (EIS; Wood and Bretherton, 2006) were computed from the daily-averaged meteorological variables to facilitate comparisons among different calendar months. EIS, a measurement of the strength of the inversion in the lower atmosphere that has been shown to correlate positively with cloud fraction on seasonal time scales in the marine stratocumulus regions (Wood and Bretherton, 2006), was calculated from the reanalysis fields over the southeast Atlantic:

$$EIS = LTS - \Gamma_m^{850}(z_{700} - LCL) \quad (2.1)$$

where the *LTS* is the lower tropospheric stability,  $\Gamma_m^{850}$  is the moist-adiabatic potential temperature gradient at 850 hPa,  $z_{700}$  is the height of the 700 hPa level, and *LCL* is the lifting condensation level.

The *LTS* is calculated following Klein and Hartmann (1993):

$$LTS = \theta_{700 \text{ mb}} - \theta_{1000 \text{ mb}} \quad (2.2)$$

where  $\theta$  is the potential temperature calculated as:

$$\theta = T \left( \frac{p_0}{p} \right)^{\frac{R_a}{c_p}} \quad (2.3)$$

where  $T$  is the temperature,  $p_0$  is the pressure at 1000 hPa,  $p$  is the pressure,  $R_a$  is the dry air gas constant, and  $c_p$  is the specific heat of dry air at constant pressure (Wallace and Hobbs, 2006, pg. 78). The moist-adiabatic potential temperature gradient at 850 hPa is calculated as in Wood and Bretherton (2006):

$$\Gamma_m^{850} = \left( \frac{g}{c_p} \right) * \left( 1 - \frac{1 + \frac{L_v q_s}{R_a T}}{1 + \frac{L_v^2 q_s}{c_p R_v T^2}} \right) \quad (2.4)$$

where  $g$  is the gravitational acceleration,  $L_v$  is the latent heat of vaporization (at 273 K; taken to be constant with temperature),  $q_s$  is the saturation mixing ratio, and  $R_v$  is the gas constant of water vapor. The height of the 700 hPa level is calculated as in Wood and Bretherton (2006):

$$z_{700} = \left( \frac{R_a T_o}{g} \right) * \ln \left( \frac{p_o}{700 \text{ hPa}} \right) \quad (2.5)$$

where  $T_o$  and  $p_o$  are the temperature and pressure, respectively, at 1000 hPa. The *LCL* is calculated as:

$$LCL = 125 * (T - T_d) \quad (2.6)$$

(as in Lawrence, 2006; citing Epsy (n.d.)) where the temperature  $T$  and dew point temperature  $T_d$  are taken at 1000 hPa.

## **2.4 Surface and upper air observations**

The coastal region of southwestern Africa where the sharp westward-moving cloud boundaries originate has very few operational meteorological observations. The closest marine operational upper-air sounding location is at St. Helena Island (-15.942° latitude, -5.776° longitude), roughly 1,900 kilometers west of the southwestern African coast. High resolution sounding data from this location were obtained from the UK Met Office's British Atmospheric Data Center (found at: <http://catalogue.ceda.ac.uk/uuid/f7f3478135e81472e056889935d284d7>; Met Office, 2007) for the period 01 January 2000 through 31 December 2011. These soundings are launched roughly once per day usually at 11:00 LT from an altitude of 436 meters (the sounding site is on top of a hill). The sounding reports data every 2 seconds (~ every 10 m).

While the sharp cloud boundaries can move hundreds of kilometers west of the African coast, most of the time they do not reach as far west as St. Helena Island. Hence, it cannot be reasonably expected that the soundings from St. Helena represent with fidelity the conditions of the atmosphere through which the sharp cloud boundaries are moving. These soundings do provide information on atmospheric conditions along the edge of the climatological marine stratocumulus field (e.g. Burleyson and Yuter, 2015a) and hence physically constrain conditions closer to the coast.

To identify the subset of soundings from St. Helena that was more likely representative of the adjacent marine stratocumulus region, we analyzed individual available soundings in the following way. The daily-averaged (i.e. not the average of the 3-hourly product, but a different daily mean product from NASA's GES DISC) lower tropospheric stability (LTS) was calculated for all MERRA reanalysis grid points along -16° latitude from -5.625° longitude to 10° longitude (roughly between St. Helena and the southwest African coast) on the same days as the available soundings. When the reanalysis LTS values along this transect varied by 3 K or less, the sounding for that day

was deemed 'representative' of the adjacent marine stratocumulus region and was included in the subsequent analysis. Figure 2.4 shows a schematic illustrating this algorithm. Note that the value of 3 K was chosen to keep the variability across the transect relatively low but also to allow for a relatively large number of usable soundings (e.g. a value of 2 K would produce 48 and 25 usable soundings for January and May, respectively, compared to 115 and 65 soundings for the value of 3 K).

A further quality control step identified the subset of 'representative' soundings that exhibited a strong low-level inversion. A strong inversion is necessary for a marine stratocumulus cloud-topped boundary layer (Klein and Hartmann, 1993). We define a strong inversion as a change in potential temperature of at least 8 K within a 300 m layer. Similar to the LTS change requirement, the potential temperature change and layer thickness parameters controlled the subset of soundings we analyzed (i.e. a higher potential temperature change or smaller layer thickness requirement would result in fewer soundings analyzed, and vice versa).

An algorithm searched for such inversions starting at the lowest point in each sounding ( $\sim 0.4$  km) and continued up to 3 km. If an inversion was found, the height of the inversion was estimated as the approximate top of the 300 m layer, and the sounding was used in the subsequent analysis. Varying the potential temperature change and the layer thickness requirement separately to values of 6 and 10 K and 200, 400, and 600 meters resulted in a change in the median inversion height of up to tens of meters, a change in the minimum of the monthly annual medians of the Brunt Väisälä frequency (discussed later in this section) on the order of a few  $1.0e-4$  s<sup>-1</sup>, and an even smaller change to the maximum of this parameter. The monthly-averaged Richardson number (discussed later in this section) with these varied parameters also showed values for all months above 1, as is seen with the final parameters employed. Setting the potential temperature change requirement to 15 K resulted in prohibitively too few soundings for meaningful analysis.

Monthly statistics of the upper-air conditions were calculated based on this subset of 'representative' soundings with strong inversions. However, due to the changing height of the inversion from day to day, simple averaging of the variables

between soundings would mask important features near the inversion. To overcome this, the sounding data were analyzed in 10 meter inversion-relative height bins, and the median inversion height for the month was used to normalize the inversion-relative height bins to a ‘standard’ inversion. This inversion-relative sounding analysis masks changes in soundings that co-vary with inversion height, but an analysis that would take this co-variability into account is beyond the scope of this study.

To characterize the strength of the stability in the stable layer, the square of the dry Brunt Väisälä frequency was calculated similar to Kondo et al. (1978):

$$N^2 = \frac{g}{\bar{\theta}_v} \frac{\partial \theta_v}{\partial z} \quad (2.7)$$

where  $g$  is the acceleration due to gravity,  $\bar{\theta}_v$  is the virtual potential temperature at the center of the layer,  $\theta_v$  is the virtual potential temperature, and  $z$  is the height in meters. This parameter was used to investigate wave propagation conditions from upper-air soundings in da Silva and Magalhães (2009) and Magalhães et al (2011). Note that this equation is the numerator of the Richardson number (Wallace and Hobbs, 2006, pg. 380).

We calculate  $N^2$  across the stable layer which corresponds to the inversion at the top of the marine boundary layer (see Figure 2.5 for a schematic illustrating how  $N^2$  was calculated from sounding data). The altitude bounds of the stable layer were determined in several steps. In step one, we calculate the first derivative of the virtual potential temperature with height. The height of the maximum of the first derivative value was found, and a 500 meter wide layer centered on this maximum was further considered (Figure 2.5 panel b). The minimum and maximum value of the second derivative of virtual potential temperature with height within the 500 meter wide layer were identified and taken as the top and bottom of the stable layer (Figure 2.5 panel c). Within this 500 meter wide layer, roughly where the virtual potential temperature begins to rapidly increase with height (maximum of the second derivative) is taken as the bottom of the stable layer, and where the rate of increase with height rapidly decreases (minimum of the second derivative) is taken as the top. The virtual potential

temperatures at these two altitudes were then used to calculate the dry Brunt Väisälä frequency value across the stable layer (Figure 2.5 panel d).

The Richardson number, the ratio of the consumption of turbulence versus the mechanical generation of turbulence through wind shear (Wallace and Hobbs, 2006, pg. 380) is used to investigate whether ambient conditions are conducive to turbulence. The gradient Richardson number was calculated as:

$$R_i = \frac{g}{\bar{\theta}_v} \frac{\frac{\partial \theta_v}{\partial z}}{\left(\frac{\partial u}{\partial z}\right)^2 + \left(\frac{\partial v}{\partial z}\right)^2} \quad (2.8)$$

where  $u$  and  $v$  are the wind components in the zonal and meridional directions, respectively (similar to Kondo et al., 1978). Katzwinkel et al. (2012) used in situ aircraft measurements at the top of marine stratocumulus (i.e. the cloudy-clear interface) and calculated the gradient Richardson number across vertical distances of five meters and then smoothed these values over a distance of 25 meters. Since the sounding measurements employed in the current study involve a vertical step size on the order of 10 meters, we use a vertical distance of 25 meters over which to calculate the Richardson number. This layer was centered on the top of the stable layer defined above and in effect spans from inside the inversion layer to the free atmosphere above the inversion (Figure 2.5 panel d).

Note we do not employ the use of COSMIC upper air soundings (Constellation Observing System for Meteorology, Ionosphere, and Climate; see: <http://www.cosmic.ucar.edu/>) in this analysis. The monthly-averaged boundary layer depth derived from COSMIC data has been shown to vary up to several hundred meters from the boundary layer depth determined from in situ upper air soundings as well as from MODIS cloud top height estimates for the southeast Pacific marine stratocumulus region (Wyant, et al., 2010; their Figure 10).

Surface meteorological variables were obtained from a research facility in Gobabeb, Namibia ( $\sim -23.5^\circ$  latitude,  $\sim 15.0^\circ$  longitude; data courtesy of Roland Vogt, University of Basel). 24 meter air temperature, dew point, wind direction, and wind

speed as well as 1.5 meter atmospheric pressure were analyzed for an instance of a sharp cloud boundary moving away from the coastal regions near this collection site.

### **3.) Results**

#### **3.1. Morphology of cloud erosion along westward-moving boundaries**

##### 3.1.1 Synoptic scale features

Cloud boundaries moving westward from the southwestern African coast can erode cloud to varying degrees from complete clearing (Figures 3.1 and 3.2) to partial erosion (Figures 3.3 and 3.4). The comparison between the morning Terra overpass (~10:30 LST) and the afternoon Aqua overpass (~13:30 LST) illustrates the westward movement of the boundaries and the cloud erosion behind them. The detailed morphology of erosion along these cloud boundaries can vary widely among cloud boundaries (compare above figures). Details of the cloud geometry and degree of erosion can also vary along a single boundary (e.g. Figure 3.2 panels b/e and Figure 3.3 panels c/f/i) as well as a function of time (e.g. Figure 3.3 panels b/e). The horizontal extent of the westward-moving boundaries can range from hundreds to ~ 1,000 kilometers long. Oftentimes the boundary shape roughly resembles the geometry of the region of the southwestern African coast from which the boundaries move away from; though it is possible that the strong southerly winds may modify the shape of the westward-moving boundaries (e.g. Figure 3.1 panels b/e).

The variability in time and location along the boundary of the nature of the cloud erosion is further illustrated in Figure 3.5, which shows enhanced Meteosat visible satellite images (from EUMETSAT; see Section 2.1) of a westward-moving sharp cloud boundary observed off the southwestern African coast on 26 May 2012. The nature of the erosion of the cloud deck changes between the 09:00 UTC and 14:00 UTC images. Over the southern two thirds of the boundary at 09:00 UTC, the region immediately (within tens of kilometers) behind the cloud boundary is characterized by nearly complete clearing, while the northern third exhibits a transition from relatively higher to relatively lower (but non-zero) cloud fraction. As the boundary moves further

westward with time, the region of complete clearing behind the boundary narrows, shrinks, and shifts southward (see also Animation 3.9, which shows an animation of the visible satellite imagery of this cloud boundary. See Appendix A for details on animations).

A small amount of this observed change in the cloud field behind the boundary may have to do with a change in the incoming solar radiation due to the varying solar elevation angle (Kidder and Haar, 1995, pg. 79). To estimate the change in sun angle at different points near the boundary at different times, the solar elevation angle was calculated using the NOAA Solar Calculator (found here: <http://www.esrl.noaa.gov/gmd/grad/solcalc/>). The yellow points on Figure 3.5 panels a and f denote the approximate locations at which the solar zenith angle was calculated at the times of the corresponding images (note the locations of these points were chosen to capture the variation in sun angle across roughly the same latitude and longitude ranges over which the variability in the cloud boundary appearance occurs between the first and last frame).

The solar zenith angle at these points and times varies between  $\sim 38^\circ$  (at  $-13^\circ$  latitude,  $9^\circ$  longitude) and  $\sim 45^\circ$  (at  $-9^\circ$  latitude,  $10^\circ$  longitude). Following Kidder and Haar (1995, pg. 79), the incident radiation that is available to be reflected is given by:

$$L_i \cos \theta_i \quad (3.1)$$

where  $L_i$  is the incident solar radiance and  $\theta_i$  is the zenith angle of the sun. Assuming a constant solar irradiance, there would be a roughly 10% change in the radiation available to be reflected when the sun is at  $\sim 38^\circ$  compared to when it is at  $\sim 45^\circ$ . Additionally, while the enhancement of these images to allow for easier viewing of the changes to the cloud field does produce a modification in the way the clouds are perceived, this modification is expected to vary minimally between frames.

At varying distances behind the cloud boundaries in Figures 3.1-3.4, areas of scattered low cloud are present. Based on loops of Meteosat visible images acquired every 15 minutes, we infer that some of these patchy areas represent examples where

cloud was only partially eroded when the boundary passed (e.g. Animation 3.6) while others are instances where low cloud has reappeared after being completely cleared during boundary passage (e.g. Animation 3.7). In some instances, both of these processes seem to be at work, with adjacent regions behind the boundary containing cloud that was partially eroded and cloud that was regenerated after clearing (e.g. Animation 3.8).

The clouds nearest the coast are influenced by the westward-moving boundaries while it is still dark. The determination of cloud versus sea surface is somewhat ambiguous from infrared brightness temperature (IR) data, particularly for low thin cloud, and so the degree of the cloud deck's initial erosion along the coast is difficult to discern from the IR data alone. Additionally, some areas behind the boundary with scattered cloud in the morning Terra overpass are clear in the afternoon Aqua overpass (e.g. Figure 3.1 panels a/d). These daytime clearings likely indicate shortwave radiative erosion of thin cloud.

The loops of Meteosat visible images provide clear evidence that the main westward-moving boundaries are the result of gravity waves rather than the result of advection in the boundary layer. Animation 3.9 displays a particularly clear example of this. In order to track the movement of the cloud deck, a discrete cloud element ahead of the cloud boundary has been identified using an orange circle and its location has been tracked by eye throughout the animation. This has also been done with a cloud element in the wake of the cloud boundary that appears roughly halfway through the animation. The cloud advection, as evidenced by the movement of the detailed features within the cloud field, is generally from the south, consistent with the mean low level flow (see Figure 3.26). The cloud-eroding boundary moves generally from the east to the west. A similar relationship between the movement of the cloud deck and the direction of motion of the boundary is a common feature in all the animations we have examined (not shown). It is worth noting though that the direction of the background flow at cloud level and the direction of motion of the cloud boundaries are not strictly parallel.

IR satellite imagery reveals the cloud boundaries as they first become observable in the marine stratocumulus near the coast around 00:00 UTC. Figure 3.10 and Animation 3.11 show the IR data for the two days spanning 13 June 2014 to 14 June 2014 to illustrate the nature of the cloud boundaries around their time of generation. Over the ocean (i.e. to the west of the black outline of the African coast) clouds are observable as IR brightness temperatures of  $\sim 280$  K or lower, while the darker ( $\sim 290$  K and above) brightness temperatures are the underlying sea surface. At 20:00 UTC, the coastal region of Angola in the vicinity of  $12.5^\circ$  longitude and  $-12^\circ$  latitude is characterized by cloudy conditions (evidenced by brightness temperatures of  $\sim 280$  K). By 22:00 UTC, a very small region of cloud clearing is observable adjacent to the coast, as brightness temperatures transition from  $\sim 280$  K to  $\sim 290$  K. At 00:00 UTC, the region of cloud clearing has increased in area and is spreading toward the north and west. From 02:00 UTC to 06:00 UTC, this sharp cloud boundary continues to move north and westward, away from the coast. The animation of another cloud boundary (shown in Animation 3.12) shows a general location and speed of motion for the cloud boundary consistent with its movement away from the coast occurring around 00:00 UTC.

In order to more easily analyze multiple, successive days of IR satellite data, Hovmöller diagrams of these data covering the region bounded by  $-20^\circ$  and  $-10^\circ$  latitude and  $-6^\circ$  and  $13^\circ$  longitude for January and May of 2014 are shown in Figure 3.13. The eastern bound of the analysis region encompasses a portion of the southwest coast of Africa, and the diurnal cycle in land temperature shows up clearly as high brightness temperatures during daylight hours and lower brightness temperatures during the night. The diurnal cycle in cloud fraction (e.g. Burleyson and Yuter, 2015a) is evident as horizontal bands of lower brightness temperatures (higher cloud fraction) at night and higher brightness temperatures (lower cloud fraction) during the day. An orange bracket indicates the low cloud fraction portion of one of these diurnal cycles between January 8<sup>th</sup> and January 9<sup>th</sup> (Figure 3.13 panel d). Especially in January, this region occasionally contains high clouds, mainly from deep convection originating over the nearby continent (brightness temperatures  $\sim 270$  K; see Figure 3.13 panels e and f).

Clearing of the cloud deck from east to west (such as would occur with the sharp cloud boundaries of interest) manifests in the Hovmöller diagrams as diagonal gradients in brightness temperatures. These transitions in brightness temperature associated with westward-moving boundaries are highlighted with yellow arrows in the Hovmöller diagrams. January represents a time of year with few westward-moving cloud boundaries, while on average many more occur in May (see Section 3.2). Many of these transitions to higher brightness temperatures become apparent in the cloud field within a few hours of 00:00 UTC and within a few degrees longitude of the coast, consistent with the IR animations showing a nocturnal, coastal origin of the cloud boundaries.

The westward speed of motion of the boundaries can be estimated from the distance traversed in degrees longitude by these cloud clearings over a specified time in the Hovmöller diagrams (i.e. the slope of the brightness temperature gradient). Based on five examples from May 2014, the average westerly component of motion is  $\sim 11 \text{ ms}^{-1}$  with specific examples varying from  $\sim 8$  to  $\sim 14 \text{ ms}^{-1}$ . Using the Terra and Aqua MODIS corrected reflectance images to compare the westward component of the speed of the cloud boundaries for these five examples results in a similar average speed of motion around  $10 \text{ ms}^{-1}$  (varying between  $\sim 9$  and  $\sim 11 \text{ ms}^{-1}$ ) with the differences between the corresponding Hovmöller-derived speeds and those speeds derived from the MODIS images ranging from 1 to  $5 \text{ ms}^{-1}$  difference. Note that these Terra and Aqua corrected reflectance speeds are based on speeds between two distinct points, while the Hovmöller speeds are based on a meridional average. Future work will delve into determining a more robust westward speed of the cloud boundaries.

We also calculate a rough estimate of the radiative impact this cloud erosion could have by comparing the amount of incident solar energy that is not radiated back to space under various scenarios of cloud clearing. We compute the area-averaged increase in net radiation as:

$$\Delta rad = \frac{A_T Q(1 - \alpha_c) - (A_C Q(1 - \alpha_c) + A_O Q(1 - \alpha_o))}{A_T} \quad (3.2)$$

where  $A$  denotes the area,  $\alpha$  the albedo, and  $Q$  the total solar insolation. The subscript  $T$  denotes the total area, the subscript  $C$  denotes the cloudy area and cloud albedo, and the subscript  $O$  denotes the ocean area and ocean albedo. Bender et al. (2011, their Figure 1) used a combination of MODIS cloud fraction measurements and CERES (Clouds and the Earth's Radiant Energy System) top of atmosphere shortwave radiative fluxes to determine the albedo of marine stratocumulus (over  $2.5^\circ \times 2.5^\circ$  grid boxes) in the southeast Atlantic. For 100% cloud fraction, they found slightly different cloud albedo values using MODIS Aqua (0.35) versus MODIS Terra (0.39). We use the lower number as the value of  $\alpha_c$  in our analysis to achieve a conservative estimate of radiative impact. We assume a value of  $Q$  of  $400 \text{ Wm}^{-2}$  (Engström et al., 2014) and a value of  $\alpha_o$  of 0.06 (National Snow and Ice Data Center: <https://nsidc.org/cryosphere/seaice/processes/albedo.html>). Using Eq. 3.2, we then calculate the area-averaged shortwave radiative flux change over a  $300\text{km} \times 300\text{km}$  region with different proportions of the total area containing cloudy versus clear skies. Table 3.1 displays the results of these estimates, with radiative impacts ranging from  $116 \text{ Wm}^{-2}$  for complete clearing of the cloud field to roughly  $23 \text{ Wm}^{-2}$  for a clearing of 20% of the cloud field.

The preceding still images and animations of IR data, as well as the Hovmöller diagrams, have shown that cloud clearing along these sharp boundaries occurs not just during daylight hours but also during the night. While shortwave fluxes likely aid in cloud removal, they are not required for the erosion of cloud along the sharp cloud boundaries. This is in contrast to the Connelly et al. (2013) modeling study of cloud clearing associated with gravity waves originating from a disturbed subtropical jet, where short wave fluxes were required to remove cloud.

### 3.1.2 Small scale features along the boundary

#### a. Abrupt transitions

Close-up images along the cloud boundaries often show a sharp and abrupt transition from overcast to clear or from overcast to broken cloud over spatial scales of a few kilometers or less (e.g. Figure 3.1 panels g, h, and i, Figure 3.2 panel h, and Figure 3.3 panel g). Along some cloud boundaries, the sharp transition from cloudy to less

cloudy conditions occurs along a sharp edge. Close-ups reveal that individual clouds appear to be bisected by the cloud boundary, in the sense that the portion of the cloud on the eastern side of the boundary is missing rather than the entire cloud being modified (e.g. Figure 3.1 panels h and i and Figure 3.4 panels h and i). These examples of sharp boundaries suggest very rapid removal of cloud. Animated loops of visible satellite imagery reveal that cloud is removed in 15 minutes or less (e.g. Animation 3.14).

Detailed examination of examples where the cloud field transitions from overcast to broken conditions along the boundary do not suggest a fundamental change in the overturning cellular structure of the convection. For instance, the cloud boundary on 05 May 2014 shown in Figure 3.4 panels c/f/i and Animation 3.15 contains features that resemble open cells behind the boundary. However, analysis of the cloud field before, during, and after erosion suggests that the thinner portions of the closed cellular convection are being eroded and the thicker portions of the cloud are retained. We do not see clear evidence of a change in the cloud pattern consistent with a change in mesoscale circulation as would be required for a true transition from closed to open cellular convection (Atkinson and Zhang, 1996).

To explore the possibility that precipitation is occurring along an example of a cloudiness transition, we employ the heavy drizzle detection methodology of Miller and Yuter (2013). Figure 3.16 displays the binary drizzle detection (panel a) in the region of a westward-moving cloud boundary on 01 May, 2010 based off of the 1 km MODIS Aqua liquid water path measurements (LWP, panel b). Comparison with the corrected reflectance image of the cloud boundary (panel c) shows there is no detectable heavy drizzle present along the sharp transition in cloudiness. Based off of this and several other cases of this drizzle detection algorithm applied to cloudiness boundaries, no detectable precipitation is occurring along the edge of the cloudiness boundaries. Additionally, based off of the 1 km MODIS liquid water path measurements, there is no enhancement of the LWP in the vicinity of the boundary (see Section 4.5). Future work will investigate the precipitation properties along a larger number of cloudiness transitions to determine if this is a representative characteristic of the boundaries.

As an additional way to observe the cloud boundaries, our research group requested astronauts on board the International Space Station (via the Earth Science and Remote Sensing Unit, NASA Johnson Space Center, see: <http://eol.jsc.nasa.gov/>) obtain images of the sharp cloud boundaries in the southeast Atlantic. An example of this astronaut photography of a westward-moving cloud boundary on 21 May 2016 is shown in Figure 3.17. While these images do not reveal characteristics of the cloud boundary that were not observable in the Terra and Aqua MODIS corrected reflectance images, they do provide a unique oblique view of the boundary that is not possible with the nadir imaging of the MODIS instrument. Close-up images of cloud boundaries serendipitously captured by astronauts in the future could be used to investigate the smaller-scale features of the boundaries not possible with the images from the MODIS instrument, as NASA has reported a pixel size down to 3 meters (see: <http://eol.jsc.nasa.gov/FAQ/>) compared to 250 meters for MODIS images.

b. Small wavelength bands parallel to main cloudiness boundary

Frequently occurring features near the cloud boundaries are sets of narrow  $\sim 10$  km or less wavelength elongated, banded features roughly parallel to the cloud boundary. These features can be observed on the cloudy sides of the sharp cloud boundaries (e.g. Figure 3.1 panel h) as well as on the sides with reduced cloud fraction (e.g. Figure 3.2 panels g and i and Figure 3.3 panel h). These features are usually only visible along a portion of the main westward-moving boundary.

The ribbed nature of the clear and cloudy regions is qualitatively similar to previously documented cloud-generating gravity waves in the marine boundary layer (e.g. da Silva and Magalhães (2009); Désalmand et al (2003); Zheng et al. (1998)), with wavelengths in the same general range ( $\leq 10$  kilometers in the aforementioned studies). The overall structure of the wave trains trailing a larger perturbation (i.e. the sharp cloud boundary itself) is generally more comparable to undular bores (e.g. Clarke et al. 1981, Koch et al. 2008). While we do not systematically examine the liquid water path associated with the cloud boundaries, Figure 3.16 panel b does not show any evidence of liquid water path enhancement along the supposed leading edge of the bore (as would be expected for a bore; e.g. Martin and Johnson, 2008).

### 3.1.3 Small wavelength cloud bands not parallel to main cloudiness boundary

Small-scale cloud wave trains that are not directly associated with the main westward-moving boundary can also occur in the southeast Atlantic regional cloud field. Many of these wave trains move south or northeast. An example of this phenomenon is shown in Figure 3.4 a/d, where several large, southward-moving gravity wave trains are faintly visible in the northern and central parts of the image (see also the Meteosat visible images animated loop for this day in Animation 3.18). A further illustration is shown in Animation 3.19 where cloud wave trains apparently propagate from several directions and overlap each other. While highly speculative, a potential source for southward moving gravity waves is tropical deep convection (Mapes 1993), as western equatorial Africa is a highly active convective region (e.g. Blanc et al., 2014). Birch and Reeder (2013) documented similar cloud wave trains off the northwest coast of Australia during seasons when deep convection was common over the nearby continent (note: here we refer to the convectively-generated cloud lines in their study, and not the bore-like cloud lines they describe). While also highly speculative, the wave trains moving northeast may be associated with extratropical cyclones poleward of the subtropical cloud deck similar to those seen in Allen et al. (2012). This discussion of cloud bands likely from gravity waves not associated with the main cloud boundary is mainly intended as an illustration of the previously-undocumented variability of the cloud deck, the ability for mechanisms originating from outside the cloud deck to impact the cloudiness in this region, and to illustrate that the boundary layer in this region is conducive to the propagation of gravity waves.

### 3.2. Cloud boundary monthly frequency

Pairs of MODIS corrected reflectance true color images from the morning Terra and afternoon Aqua overpasses for the period 08 May 2012 to 01 Nov 2015 were examined to determine how frequently westward-moving cloud-eroding boundaries occur in each month (Figure 3.20). All months were observed to have an average of at least 1 westward-moving cloud boundary per month. There are two local maxima in the frequency occurrence of monthly cloud boundaries, during the months of April, May,

and June and in November and December. May has the highest average number of cloud boundaries identified with ~ 20 boundaries per month. April has ~ 12 cloud boundaries per month and June roughly 8. The frequency of cloud boundary occurrence decreases from May until August (~ 3 per month) and then increases to ~ 6 per month in November and ~ 5 per month in December. The boundaries enumerated in Figure 3.20 are the subset that were clearly and unambiguously moving westward and eroding cloud (see Section 2.2). Hence, the frequency of occurrence shown in Figure 3.20 represents a robust lower bound. There were additional boundaries present whose degree of clearing and/or westward motion was ambiguous. Details on these boundaries, as well as cloud scene pairs that exhibited no cloud boundaries are discussed in Appendix B.

### **3.3 Large scale conditions for the maximum and minimum cloud boundary months**

In this section, the large scale conditions in May, the month with the highest number of cloud boundaries, and January, the month with the lowest number of cloud boundaries, are compared. We examine the average cloud fraction, sea surface temperatures (SSTs), sea level pressure and wind vectors, 700 hPa pressure vertical velocity, and estimated inversion strength (EIS, Wood and Bretherton, 2006). While the impacts of the SSTs on the marine boundary layer environment are seen in the EIS, we examine SST mainly for additional context of the environment in which the cloud boundaries occur more and less frequently.

The ISCPP-derived total cloud fraction across the annual cycle in the southeast Atlantic (Fig. 3.21, from Zhang and Li, 2013) shows a clear annual cycle in cloud fraction with a peak in August and a minimum in May. January shows a relatively low cloud fraction.

The spatial patterns of the average sea surface temperatures in the months of May and January for the period 2000 through 2011 are compared in Figure 3.22. The SSTs along the eastern region of the south Atlantic are strongly influenced by the cold Benguela current year-round, as well as by a region of cold upwelling water

immediately adjacent to the southwestern coast of Africa (Peterson and Stramma, 1991 and references therein). The SSTs for May show the cold current with the lowest temperatures ( $\sim 16^\circ \text{C}$ ) occurring in the upwelling region along the coast between roughly  $-30^\circ$  and  $-20^\circ$  latitude. Along the coast and near  $-15^\circ$  latitude, there exists a sharp transition to warmer temperatures ( $\sim 25^\circ \text{C}$  and above) known as the Angola-Benguela Frontal Zone (e.g. Veitch et al., 2006). This SST front decreases in strength with increasing distance from the coast (Veitch et al., 2006). The spatial gradient in SSTs from roughly  $-15^\circ$  latitude to several degrees latitude north of this increases along the coast from May to January (Figure 3.22), broadly consistent with Veitch et al. (2006). While the region of upwelling along the coast is not as strong in January as in May, in January cold water ( $\sim 20\text{-}23^\circ \text{C}$ ) extends further to the north and west toward the vicinity of St. Helena Island. Again, while the SSTs were mainly analyzed herein for environmental context, future work will explore the differences in the temperature differential between the sea surface and the adjacent land surface (i.e. the driver of the sea/land breeze circulation) between May and January as a possible contributor to the observed monthly variations in cloud boundary frequency.

Animations showing MERRA-derived monthly mean sea level pressure and 1000 hPa winds, EIS, and pressure vertical velocity at 700 hPa through the annual cycle (Section 2.3) are displayed in Animations 3.23 - 3.25. The patterns in these animations correspond to well-documented annual large-scale changes in the location of the semi-persistent south Atlantic high, the position of the ITCZ, and the strength of the Hadley cell (e.g. Ahrens, 2009, pgs. 263-266). The pressure vertical velocity at 700 hPa is also in broad agreement with that of the modeling study of Painemal et al. (2014) for the months September through November, however the core of the strongest EIS presented herein is a few degrees longitude south of the core of the strongest inversion (defined differently) than that in the Painemal et al. (2014) study for the September through November period. We now focus on the MERRA-derived large-scale differences between May and January.

The positions of the semi-permanent high over the southeast Atlantic, as well as those of mesoscale pressure systems over the African continent, could play into the

meteorological conditions that are conducive to the formation of the cloud-eroding boundaries. The monthly-averaged sea level pressure (Figure 3.26) for May shows the southeast Atlantic subtropical high to be centered at roughly  $-28^{\circ}$  latitude,  $-5^{\circ}$  longitude with a mean central pressure of  $\sim 1020$  hPa with pressures decreasing to the north and east. Over land, a gradual pressure gradient exists with higher pressures (between 1015 to 1020 hPa) in the southeastern region of southern Africa which gradually decrease to below 1010 hPa in central Africa. Compared to May, the January southeast Atlantic subtropical high is roughly the same strength, though it has shifted to the south and west to be centered near  $-31^{\circ}$  latitude,  $-7^{\circ}$  longitude. Over the African continent, the most drastic change from May is present as a region of low average pressure (approaching 1005 hPa) associated with the thermal low over the Namib desert, consistent with Peterson and Stramma (1991; citing Höflich, 1984). Mainly north of  $-15^{\circ}$  latitude and within  $\sim 10^{\circ}$  longitude west of the coast, the wind vectors are stronger in May than in January.

To further investigate how the sea level pressure is associated with the occurrences of the cloud boundaries, the three-hourly instantaneous MERRA reanalysis data were used to generate composites of sea level pressure for the period April through June 2013. Composites were generated at 00 UTC for days on which westward-moving cloud boundaries were and were not definitively identified in the Terra and Aqua MODIS corrected reflectance images (i.e. 'maybe' days were included in the days without cloud boundaries). During this ninety-one day period, there were 48 days on which westward-moving cloud boundaries were identified. Figure 3.27 displays the composite of mean sea level pressure, as well as the composites of the inner quartile range of the sea level pressure, at each grid point for this period.

On days on which cloud boundaries were detected, the mean semi-permanent high over the southeast Atlantic has a central pressure of  $\sim 1020$  hPa, while the high on days on which cloud boundaries were not detected has a mean central pressure of  $\sim 1023$  hPa (panels a and c). These regions of composited high pressure occur in a region where the inner quartile of the composited pressure values ranges from  $\sim 2$  to  $\sim 13$  hPa (Figure 3.27, panels b and d). Future work will further investigate the statistical

significance between differences in the mean meteorological conditions on boundary and non-boundary days, as well as the potential ramifications of these conditions with regards to their impact on the frequency of the cloud-eroding features.

In addition to the fact that the estimated inversion strength (EIS) has been shown to correlate with cloud fraction on seasonal time scales (Wood and Bretherton, 2006), the strength of the inversion would also have implications for the conduciveness of the inversion to propagate gravity waves. We investigate this parameter for these reasons, as well as the fact that an increase in EIS has been found to climatologically increase cloud fraction and cloud thickness in the marine stratocumulus regions (employing grid point sizes of  $2.5^{\circ} \times 2.5^{\circ}$ ; Myers and Norris, 2013). EIS is therefore a parameter that could indicate a more or less robust cloud deck (implying a lower or higher likelihood of erosion along the observed cloud boundaries) with higher values implying a likely more robust cloud deck and lower values implying a likely less robust cloud deck. Figure 3.28 shows the MERRA reanalysis-derived mean EIS for the southeast Atlantic for May and January, 2000 through 2015. Overall, monthly average EIS values are quite similar in the subtropical southeast Atlantic in January and May, though the core of the highest EIS values (located around  $-20^{\circ}$  latitude,  $0^{\circ}$  longitude in May) is slightly stronger and shifted to the southeast several degrees latitude and longitude in January compared to that in May.

Myers and Norris (2013) also found that, climatologically, an increase in the pressure vertical velocity at 700 hPa results in a net decrease in cloud fraction and cloud thickness. We investigate this as another parameter that could be a possible contributor to a more or less robust cloud deck (i.e. one that would be less or more conducive to erosion along the observed cloud boundaries) with larger values implying a likely less robust cloud deck and lower values implying a likely more robust cloud deck. Two broad swaths of relatively strong positive 700 hPa vertical pressure velocity exist over the southeast Atlantic in May (Figure 3.29 panel a). The larger of these has a maximum (0.06 Pa/sec or larger) along the coast just north of  $-15^{\circ}$  latitude which weakens as it extends with a wide swath (on the order of  $\sim 10^{\circ}$  latitude wide) far to the west-northwest past St. Helena. The second, weaker (.04 to .05 Pa/sec at its maximum)

and smaller downward motion maximum is centered further to the south around  $-30^\circ$  latitude. Pockets of both upward and downward motion exist over the central and coastal regions of southern Africa. In January, much of the central part of the subtropical southeast Atlantic is dominated by slightly positive vertical velocities on the order of  $0.03 \text{ Pa/sec}$ . A large region of more intense downward motion (between  $0.04$  and  $0.06 \text{ Pa/sec}$ ) is located in the southeastern region of the southeast Atlantic south of  $\sim -20^\circ$  latitude. This region (which appears to be bimodal) extends down to  $-40^\circ$  latitude. Much of the coastal and interior region of southwestern Africa is now dominated by upward motion of  $-0.04 \text{ Pa/sec}$  or larger with some pockets of values closer to zero (note the constraint of the color map to make the details of the vertical velocities over the ocean visible).

Figure 3.30 displays the spatial median and inner quartile range of the monthly-averaged EIS and pressure vertical velocity at  $700 \text{ hPa}$  values for the region bounded by  $0^\circ$  to  $10^\circ$  longitude and  $-10^\circ$  to  $-20^\circ$  latitude (i.e. the spatial statistics in this region of the plots in Figures 3.28 and 3.29, but for all months). Note that the y axis for the pressure vertical velocity is flipped so that values decrease with height. This enables a clear comparison between factors that have been found, on a climatological timescale, to cause an increase in cloud fraction and cloud thickness (higher EIS and lower  $700 \text{ hPa}$  pressure vertical velocity) and a decrease in cloud fraction and cloud thickness (lower EIS and higher  $700 \text{ hPa}$  pressure vertical velocity; Myers and Norris, 2013). The favorable and unfavorable conditions for higher cloud fraction, based on the EIS and  $700 \text{ hPa}$  pressure vertical velocity, correspond well with the observed monthly cloud fractions in Figure 3.21. From a spatially averaged perspective though, the differences between the May and January EIS (difference of  $\sim 2 \text{ K}$ ) and pressure vertical velocity at  $700 \text{ hPa}$  (difference of  $\sim 0.02 \text{ Pa/s}$ ) are small. They are, however, consistent with a less robust cloud deck in May as compared to January (lower EIS and larger pressure vertical velocity at  $700 \text{ hPa}$ ).

There is no clear large-scale signal as to why May is a favored month for cloud-eroding boundaries to occur. Stability is stronger in January, which favors wave propagation when the fewest boundaries occur. The EIS and subsidence also suggest a

less robust cloud deck in May than in January. While these and other fields do show some monthly differences (i.e. the position of the semi-permanent high between May and January) future work will be necessary to determine the statistical significance of these differences and whether or not they have a causative association with the cloud boundaries.

Figure 3.31 shows the average frequency of heavy drizzle for the March/April/May and December/January/February seasons for night and day, following the method of Miller and Yuter (2013). As expected, the frequency of drizzle is higher during the night (e.g. Burleyson et al., 2013). March/April/May has a higher drizzle frequency day and night as compared to December/January/February. Connelly et al. (2013) in their modeling study did not find that large drizzle rates significantly contributed to cloud susceptibility to erosion by gravity waves in the southeast Pacific.

### **3.4 Atmospheric profiles from St. Helena Island**

As described in Section 2.4, the UK Met office operates a roughly 11:00 UTC operational upper air sounding station at St. Helena Island (Met Office, 2007) which is the only regular atmospheric profile in the subtropical southeast Atlantic region. No operational upper air soundings are available from the coasts of Namibia or Angola. The data from the St. Helena soundings are ~ 1,900 km from the coast and are therefore used to compare the large scale conditions along the outer edge of the marine stratocumulus region in May and January. In order to focus our analysis on soundings that are likely more representative of the adjacent marine stratocumulus to the east of St. Helena, soundings were only used in the aggregated monthly profile data set if they displayed a 'strong' inversion and occurred in an environment where the MERRA-derived lower tropospheric stability on the day of the sounding varied no more than 3 K between St. Helena and the African coast (see Section 2.4). For the period 2000 through 2011, this constraint yields 65 daily soundings for May and 115 for January for the respective aggregated monthly profile data sets. Figure 3.32 displays histograms of the inversion heights for May and January.

The mean and median sounding data derived from the inversion-relative analysis described in Section 2.4 are displayed in Figure 3.33. In May, a strong inversion is present with a median height of  $\sim 1,800$  meters as potential temperatures increase from  $\sim 296$  K to  $\sim 310$  K over a vertical distance of 500 meters. Mixing ratio values also decrease dramatically from below the inversion ( $\sim 10$  g/kg) to above the inversion ( $\sim 1$  to  $2$  g/kg). In January, the median height of the inversion decreases to  $\sim 1,750$  meters and potential temperature values above and below the inversion shift to slightly higher temperatures (austral summer in January compared to austral fall in May). The increase in potential temperature across the inversion is comparable to that in May. The mixing ratios, particularly above the inversion, show a noticeable difference as both the mean and median values in January above the inversion are 1 to 2 g/kg higher than the mixing ratios above the inversion in May. This drier air above the inversion in May could imply a greater likelihood of erosion of cloud from entrainment of free tropospheric air into the cloud deck in May than in January (see Section 4.5). Note however that the median inversion height for May is  $\sim 50$  meters higher than that for January, and it is possible that this higher inversion height may be contributing some to the observed drier conditions above the inversion in May.

Figure 3.34 shows the monthly median and inner/outer quartiles of the Brunt Väisälä frequency and Richardson number calculated from 'representative' soundings with a 'strong' inversion launched from St. Helena Island during our analysis period (see Section 2.4). A distinct annual cycle in the Brunt Väisälä frequency (or how rapidly an induced perturbation will oscillate; e.g. Wallace and Hobbs, 2006, pg. 89) is evident, with a minimum between January and April ( $\sim 1.6\text{E-}3$  s<sup>-2</sup>) and a maximum between September and October ( $\sim 2.7\text{E-}3$  s<sup>-2</sup>). These values imply greater stability in these later months, consistent with the MERRA-derived EIS (Figure 3.30) and the higher cloud fraction observed (Zheng and Li, 2013; Figure 3.21). Based on the St. Helena sounding-derived median Richardson number being  $> 1$  throughout the year, Kelvin Helmholtz instability at the top of the boundary layer is unsurprisingly not a feature of the large scale environment.

## **4.) Discussion**

### **4.1 Comparison to known marine low cloud gravity waves**

Gravity waves propagating through layers of marine stratocumulus clouds are a well-known phenomenon. The impact of gravity waves on low marine cloud decks has been explored by various observation and modelling studies (e.g. Allen et al., 2012; Garreaud and Muñoz, 2004; Connolly et al. 2013; Jiang and Wang, 2012) and the impact of gravity waves on the marine boundary layer in regions without a persistent cloud deck have been explored as well (e.g. Birch and Reeder, 2013; Clarke et al, 1981; da Silva and Magalhães 2009; Magalhães et al., 2011; Désalmand et al., 2003). The upward motion in the crest of a gravity wave can enhance the liquid water path in the cloud (e.g. Garreaud and Muñoz, 2004). Downward motion yields warming and reduction of cloud and liquid water path. Additionally, the vertical perturbations associated with gravity wave passage can result in enhanced entrainment of warm and dry air from above the inversion into the cloudy layer (Garreaud and Muñoz, 2004; Connolly et al. 2013; Jiang and Wang, 2012). The evaporation of cloud also has ramifications for the radiative dynamics at cloud top. At night, removal of cloud results in the loss of radiative cooling, less coupling between the cloud and the sea surface, and less moisture transport to the cloud. During the day, erosion of cloud results in a strengthening of the shortwave flux to the sea surface, and cloud regeneration being unlikely as the mechanism for moisture transport to the top of the marine boundary layer (i.e. turbulent mixing due to cloud top radiative cooling) is not present (e.g. Connolly et al., 2013).

Allen et al. (2012) documented observations of gravity waves caused by geostrophic adjustment of disturbed jet streams in the southeast Pacific. These gravity waves propagated northeastward toward the South American coast. Allen et al. (2012) documented increases in LWP and in frequency of heavy drizzle associated with these waves as well as patches where cloud cover transitioned from overcast to broken. The modeling study of Connolly et al. (2013) found that multiple gravity waves (150 m amplitude) propagating through a cloud layer resulted in more dramatic clearing than that from just one wave. The key differences that suggest that the Allen et al. (2012)

gravity waves and the sharp cloud-eroding boundaries in the southeast Atlantic are separate phenomena are the direction of motion and the frequency occurrence of the waves. Allen et al. (2012) only documented three gravity wave sets in October 2008 during the VOCALS campaign consistent with the set of conditions that needs to co-occur within transient disturbances on synoptic time and spatial scales for the generation of the gravity waves documented therein. In contrast, the cloud-eroding boundaries in the southeast Atlantic have a fixed, diurnal, and coastally-generated source of energy for the gravity waves.

The ‘upsidence wave’ described by Garreaud and Muñoz (2004) is a coastally-generated gravity wave that is induced by heating of the Peruvian highlands adjacent to the southeast Pacific marine stratocumulus. This heating results in southerly flow along the coast of Chile being accelerated northward, causing a zone of upward motion along the Peruvian coast (Garreaud and Muñoz, 2004). This upward motion disturbance typically breaks away from the southern Peruvian coast around 17:00 local time and propagates southwest out over the adjacent ocean (see Figure 4.1 for a diagram from Rahn and Garreaud, 2010 illustrating this phenomenon). Upward motion associated with the crest of this ‘upsidence’ gravity wave enhances the cloud depth and liquid water path of the marine stratocumulus (Garreaud and Muñoz, 2004, O’Dell et al. 2008). At longitudes closer to the coast where the passage of the wave is in sync with daytime shortwave radiative fluxes, the enhanced entrainment caused by the deepening of the boundary layer with the passage of the wave can cause a decrease in the marine stratocumulus cloud fraction (e.g. O’Dell et al., 2008). The daytime heating origin and the propagation speed of the ‘upsidence’ wave ( $\sim 30 \text{ ms}^{-1}$ ) contrast strongly with the cloud-eroding boundaries in the southeast Atlantic. The near 00:00 local time occurrence of the southeast Atlantic cloud boundary moving away from the coast discounts the possibility that the observed feature is triggered by day-time heating of the coastal highlands in Angola and Namibia. Modeling studies are needed to examine if an ‘upsidence’ wave is triggered further inland during the diurnal heating of the interior highlands, propagates westward, and takes until around 00:00 local time to cross the coast.

A well-known instance of a coastally-generated gravity wave is the Morning Glory of northeastern Australia (e.g. Clarke, 1972; Clarke et al. 1981; Christie, 1992). This phenomenon is a propagating undular bore whose waveguide is the nocturnal boundary layer (Clarke et al. 1981). The formation of cloud lines can often occur at the crests of the wave train accompanying the bore (e.g. Clarke, 1972 and Clarke et al. 1981). These undular bores are caused by the interaction of the west coast sea breeze and east coast sea breeze when they meet inland along the Cape York Peninsula. The perturbations caused by their interaction propagate as an undular bore along the marine stable layer to the south and east of the Peninsula (e.g. Goler and Reeder, 2004).

Birch and Reeder (2013) investigated the mechanisms triggering cloud lines off the northwest coast of Australia. These cloud lines occur roughly two to three times per month. While some gravity waves were associated with deep convection (Mapes, 1993), most were observed (as cloud lines) near the coast between 08:00 and 11:00 local time and propagated northwestward over the ocean (Birch and Reeder, 2013; see also Smith, 1986). Figure 4.2 shows Birch and Reeder's Figure 13 illustrating the formation of these waves. In a modeling case study, Birch and Reeder (2013) found that the gravity waves could be generated by southeasterly winds from over the continent interacting with the stable marine boundary layer. An elevated inversion over the ocean acted as the wave guide for two different perturbations. Overnight, the southeasterlies/land breeze accelerated to the northwest and interacted with the sea breeze/marine stable layer at 22:00 local time, rode up and over the stable layer, and generated a wave that traveled along the elevated inversion out over the ocean (see panel b of Figure 4.2). In the morning, gravity waves were caused by the southeasterly winds/land breeze pushing the sea breeze backwards out over the ocean near 07:00 local time, and these perturbations propagated northwestward away from the coast (see panel c of Figure 4.1). The rising motion in these waves lifted parcels to their lifting condensation levels, where the cloud lines were formed.

Da Silva and Magalhães (2009) presented observations of atmospheric gravity wave trains in the Mozambique Channel (between Madagascar and southeastern Africa). Using data from the MODIS instruments on the Terra and Aqua satellites covering a

period of 6 months, they observed 83 instances of daytime propagating wave trains, most of which occurred during the austral winter months. Their analysis of nearby upper air soundings from along the east African coast or Madagascar revealed stable layers (Scorer parameter decreasing with height) capable of acting as waveguides. One of the possible wave-generating mechanisms they suggested was a sea breeze along the coast of Madagascar.

Magalhães et al. (2011) documented the occurrence of gravity waves over the Red Sea, and found that they occurred in this region most frequently between April and July and in September. In addition to the possibility of a sea/land breeze acting as the triggering mechanism for these gravity waves, the authors proposed that downslope gap flow perpendicular to the roughly north-south axis of the Red Sea coast (Jiang et al., 2009) may also be a wave-triggering mechanism.

#### **Section 4.2 Gravity waves in the central United States**

Gravity waves and their relationship with convection have been studied extensively over the central United States (e.g. Fovell et al., 2006; Parker, 2008). Fovell et al. (2006) found that high-frequency gravity waves travel through the stable layer formed by the anvil and can trigger clouds and occasionally convection ahead of the parent system, the so-called “action at a distance”. Parker (2008) found that lifting ahead of a squall line can transition from density-current-like lifting to bore-like lifting as the boundary layer cools overnight and becomes more stable. In observations of bores in the vicinity of convection over the Great Plains, Koch et al. (2008) found that mixing behind the leading edge of a bore caused significant entrainment from above the boundary layer, resulting in substantial drying (-2 g/kg) at the surface.

#### **Section 4.3 Discussion of possible triggering mechanisms**

While the spatial cloud patterns associated with the coastal gravity waves off Australia, Mozambique, and the Arabian Peninsula differ in detail, all involve flow from the land toward the sea, elevated topography within a few hundred kilometers of the coast (though this topography is not required for the formation of the Morning Glories

of northeastern Australia; e.g. Goler and Reeder, 2004), and a waveguide in the form of a marine stable layer less than 2 km deep (deeper for da Silva and Magalhães, 2009 though). We hypothesize that the mechanism for the generation of gravity waves along the southwestern coast of Africa involves a similar interaction of nocturnal offshore flow (land breeze and/or downslope flow) with the marine stable layer.

Gille et al. (2005) used SeaWinds scatterometer data from the QuickScat and ADEOS-II satellites to investigate sea/land breezes globally for the period April to October 2003. They found the presence of a particularly strong diurnal wind cycle along most of the coast of Angola; particularly in the bay region between roughly  $-15^{\circ}$  and  $-8^{\circ}$  latitude (see Figure 4.3 for their Figure 1 a displaying the results of their analysis in the vicinity of Africa). They found the diurnal wind cycle along the Angolan coast to be more pronounced than the diurnal cycle of winds along the Namibian coast.

The southern portion of Africa is dominated by the South African plateau that drops sharply at the coasts of Namibia and Angola (Figure 4.4). Between the coast and  $\sim 100$  km inland, the elevation increases by  $\sim 1,000$  meters. Lindsay and Tyson (1990) documented the boundary layer wind characteristics of the Namib Desert in west-central Namibia near Gobabeb (see Figure 4.4). They presented evidence that this region experiences a marked diurnal cycle in the pattern of near-surface airflow. The sea breeze initiates near the coast around 09:00 to 12:00 local time and in winter penetrates the coastal regions up to the escarpment (between 100 and 200 km inland) by 18:00 local time where it lasts for only a few hours. During winter months, the inland town of Gobabeb (roughly 60 kilometers inland from the coast) begins to experience a southeasterly mountain-to-plain flow (mountain breeze) around 22:00 local time which continues until 10:00 to 12:00 local time the next day (note mountain-to-plain flow occurs in the summer as well, though it is shallower and shorter lived than its winter-time counterpart). Consistent with the observation that the cloud-eroding waves are seen to move away from the coast around local midnight, it is our hypothesis that offshore flow combining the locally-forced mountain breeze and land breeze is a plausible cause of the perturbation initiating the gravity waves/bore in the marine stable layer.

To investigate whether there is evidence for a downslope flow concomitant with a sharp cloud boundary, we analyze in situ measurements from near the coast over the period 01 August 2012 to 02 August 2012 (see Figure 4.5 for satellite imagery of the cloud boundary from this day and Animation 4.6 for an animation of the IR data for this period). Meteorological variables from a 24 meter tall tower were obtained from a research facility near Gobabeb, Namibia (data courtesy of Roland Vogt, University of Basel, Switzerland). The wind direction and temperature (at 24 meters) and pressure (at 1.5 meters) for the two-day period from 01 August 2014 to 02 August 2014 are shown in Figure 4.7. A sharp westward-moving cloud boundary is apparent in the cloud deck to the west of Gobabeb several hours after 00:00 UTC on 02 August 2014, and while the wind direction shifts from northerly to southeasterly in the time between 00:00 UTC and 03:00 UTC (implying a possible downslope flow off of the elevated terrain to the southeast; Figure 4.4) it remains unclear whether the sharp cloud boundary observed was a result of this flow pattern.

#### **Section 4.4 Additional considerations for gravity wave versus advection**

In this section we provide further evidence that supports the hypothesis that the observed phenomenon could be the result of gravity waves. The westward speed of motion of the cloud clearings, as derived from the Hovmöller diagrams as well as the Terra and Aqua MODIS corrected reflectance overpasses, was found to be roughly 10 ms<sup>-1</sup>. As a comparison to this, we calculate the intrinsic gravity wave phase speed of the environment, following Holton and Hakim (2013):

$$c = \frac{N * \left(\frac{2\pi}{L_x}\right)}{\sqrt{\left(\frac{2\pi}{L_x}\right)^2 + \left(\frac{2\pi}{L_z}\right)^2}} * \frac{1}{\left(\frac{2\pi}{L_x}\right)} \quad (4.1)$$

where  $N$  is the Brunt Väisälä frequency (square root of equation 2.7), and  $L_x$  and  $L_z$  are the horizontal and vertical wavelengths, respectively. Based on Terra and Aqua MODIS corrected reflectance images, horizontal wavelengths of 2, 5, and 8 km were used, values of 0.04 s<sup>-1</sup> and 0.052 s<sup>-1</sup> for the maximum and minimum Brunt Väisälä

frequency were employed (based on the square root of the maximum and minimum values in Figure 3.34 a), and vertical wavelengths roughly equal to the median inversion height from the St. Helena soundings in January (1750 meters; Figure 3.32), the approximate cloud top heights observed adjacent to the African coast during austral spring by Painemal et al. (2014) of 1,000 meters, and an upper bound of 10,000 meters were also employed. The resulting intrinsic gravity wave phase speeds for the combinations of these parameters are shown in Table 4.1. Excluding the results employing the 10,000 meter vertical wavelength, the phase speeds range from 5.7 to 14.1 ms<sup>-1</sup>. This is generally consistent with the westward speed of motion derived from the Hovmöller and corrected reflectance data.

An alternative possibility is that the observed clearing features are being caused by a density current that is moving from the high coastal topography out over the ocean. As a rough calculation of an expected density current's speed in this environment, we assume a cold pool temperature of 12° C (based on the overnight temperature at Gobabeb, Namibia shown in Figure 4.7) and a temperature over the adjacent ocean of 14° and 24°. These air temperature values were chosen assuming the near-surface air temperature over the ocean is equivalent to the sea surface temperatures along the coast from Figure 3.22, which is not an unreasonable assumption (Burleyson et al., 2013). Assuming a dry atmosphere at 1000 hPa that behaves like an ideal gas, the density of the density current is 1.22 kgm<sup>-3</sup> and the densities of the ambient air are 1.17 and 1.21 kgm<sup>-3</sup>. We also assume a depth of the density current to be either 100 or 500 meters. We calculate the approximate speed of density currents ( $c$ ) with these parameters following Markowski and Richardson (2010):

$$c = k \sqrt{gH \frac{\rho_2 - \rho_1}{\rho_1}} \quad (4.2)$$

where  $\rho_1$  and  $\rho_2$  are the densities of the ambient air and density current, respectively,  $H$  is the depth of the density current,  $g$  is the gravitational acceleration, and  $k$  is equal to 1 (middle of the range given by Markowski and Richardson, 2010).

Table 4.2 displays the resulting density current speeds, which ranges from 2.85 to 14.47  $\text{ms}^{-1}$ . The upper-bound of this speed is comparable to the range of observed westward-movement speeds of the cloud boundaries (between roughly 8 and 14  $\text{ms}^{-1}$ , see section 3.1.1), though the lower bound is somewhat slower than the range in observed speed. While we hypothesize that a flow similar to this may be a possible triggering mechanism for the cloud-eroding waves themselves, the perpendicular nature of the boundary motion with the observable background cloud motion (Animation 3.9) suggests strongly against this boundary layer advective feature being the actual cause of the cloud erosion.

The observation that the direction of motion of the cloud clearing and the background flow are perpendicular is based on visual analysis of satellite images; this reveals that movement of air by winds at cloud level are likely not the cause of the cloud boundaries. We also examined the MERRA reanalysis wind profiles at several locations to the west of the southwest coast of Africa along the  $-13.5^\circ$  latitude line:  $10^\circ$ ,  $7.5^\circ$ , and  $5^\circ$  longitude (see Figure 4.8 for a reference map of these locations) to determine if easterly winds either below or above the cloud layer could be plausibly associated with the cloud boundaries. Figure 4.9 shows the smallest angular difference in the MERRA reanalysis wind direction from the reference wind direction of  $90^\circ$  (i.e. easterly, or off the coast) from 1000 to 500 hPa. Painemal et al. (2014) found an approximate austral spring cloud top height for the region adjacent to the coast to be between  $\sim 0.8$  and  $\sim 1$  km, or  $\sim 920$  to  $\sim 900$  hPa. The inversion top height from St. Helena soundings has a median value of 1.8 km ( $\sim 815$  hPa) in May. Figure 4.9 illustrates two periods of eight days (21-28 May, 2014 and 03-10 July, 2014) which encompassed seven and two days (respectively) on which cloud boundaries were detected in the Aqua and Terra corrected reflectance images (the beginnings of these days are denoted in Figure 4.9 with vertical gray lines). Lower angular differences correspond to more easterly winds while higher angular differences correspond to winds that are further from being easterly.

Evidence of an advective cause of the cloud clearings would likely manifest as a sudden decrease in the wind direction difference concomitant with the occurrence of

cloud boundaries immediately along the coast ( $10^\circ$  longitude) and further to the west depending on the distance traveled by the cloud boundaries. This signal in the wind direction would be expected around local midnight (i.e. the typical occurrence time of the cloud boundaries; see Figures 3.10 and 3.13).

Figure 4.9 panels a, c, and e show two distinct features in the reanalysis wind direction difference from  $90^\circ$  during the period 21-28 May 2014. The first of these is a wide region of low wind direction difference (less than  $20^\circ$ ) that extends from the  $\sim 900$  hPa level at 22 May 2014 and increases in height by several hundred hPa by 26 May 2014. The fact that this feature increases in height over the course of several days, shows no distinct diurnal cycle, and is generally above the boundary layer suggests that it is possibly a synoptic or large-scale flow feature. The second feature is the land/sea breeze circulation realized as a recurring diurnal cycle in the wind direction difference (most clear in Figure 4.9 panel a corresponding to the near-coast grid point of  $10^\circ$  longitude). Near the surface, there is a pattern of higher wind direction difference (more onshore winds) during the afternoon and evening hours and lower wind direction difference (more offshore winds) in the morning and early afternoon hours. The return flow of the circulation is seen as an opposite pattern at a slightly higher altitude (i.e. around 925 hPa). This diurnal cycle in the sea breeze becomes less apparent at  $7.5^\circ$  longitude (Figure 4.9 panel c) and is not clearly distinguishable at  $5^\circ$  longitude (Figure 4.9 panel e). The 03-10 July 2014 period shows a less distinguishable land/sea breeze signal.

While there are easterly winds somewhere in the depth of the column between the surface and 500 hPa during cloud boundary events, there is no consistent pattern of an onset of easterly winds concomitant with the cloud boundaries at or above cloud height. The land breeze signal to some extent coincides with the occurrence of cloud boundaries, but this easterly wind does not consistently extend up to the approximate cloud level of 920 to 900 hPa. We cannot completely rule out the possibility that some kind of easterly advection plays into the westward-moving cloud boundaries, but the evidence provided by this analysis does not clearly point to a causative relationship between the wind field and the cloud boundaries.

We do not calculate the Scorer parameter, which would demonstrate the atmosphere's wave ducting ability (e.g. Magalhães et al., 2011) in a 2+ km deep layer including the cloud layer. Calculation of the Scorer parameter through the cloud layer requires the moist Brunt Väisälä frequency. The calculation of the moist Brunt Väisälä frequency (eq. 13 of Durran and Klemp, 1982) requires the total water mixing ratio which is very poorly constrained in the observations we have currently in hand.

#### **Section 4.5 Cloud erosion**

Erosion of cloud is caused by a reduction in relative humidity at cloud level. This can be achieved by either an increase in the ambient temperature, a reduction in the water vapor content of the air, or a combination of these. Entrainment of drier air can occur either from horizontally adjacent clear areas or from vertical mixing across the inversion of dry free tropospheric air. Cloud erosion is observed to occur rapidly (within 15 min, Section 3.1.2) and both during the day and night. At night there are no shortwave fluxes to erode thin cloud. The number concentration of CCN at cloud base level controls the number concentration of cloud droplets. The presence of an anomalously high number of aerosols would decrease the overall cloud droplet particle size, but increase the number of cloud droplets (e.g. Lohmann and Feichter, 2005). When dry air is entrained into cloud, larger numbers of smaller drops more readily evaporate than smaller numbers of larger drops. Cloud-eroding boundaries are observed to occur in both higher and lower aerosol concentrations (Figure 4.10) so we infer that aerosol influences are secondary to entrainment processes in cloud erosion.

The reductions in cloudiness associated with the cloud-eroding waves in the southeast Atlantic are larger and more spatially extensive than those associated with southeast Pacific gravity waves. In this section, we describe a conceptual model for how extensive cloud erosion along a gravity wave can occur (Figure 4.11).

Nocturnal cooling of the coastal highlands would result in a downslope flow off of the western side of the African continent (Lindsay and Tyson, 1990). This pool of cold air impinging upon the stable layer would generate a disturbance (Figure 4.11, panel a) that then propagates away from the coast. Mixing associated with the upward and

downward motion of the wave would entrain air into the cloud layer (e.g. Garreaud and Muñoz, 2004; Connolly et al. 2013; Jiang and Wang, 2012), resulting in evaporation of cloud droplets (Figure 4.11, panel b). Note that the exact wave-form of the perturbation presented in Figure 4.11 is questionable; as we have insufficient information to determine whether the observed perturbations in the marine stratocumulus are bores with a trailing gravity wave train or only gravity waves.

If the observed clearing phenomenon is indeed the result of a bore (which is what would likely occur with the hypothesized interaction of the downslope flow and/or land breeze with the marine boundary layer) an upward displacement of the top of the boundary layer would result (e.g. Martin and Johnson, 2008). This upward displacement would likely cause an enhancement of the cloud layer. Enhancement of the local cloud layer was seen as an increase in the liquid water path (LWP) associated with the upward motion of gravity waves in the southeast Pacific marine stratocumulus (e.g. Allen et al., 2012; Jiang and Wang, 2012). While we do not systematically examine the LWP values associated with the occurrence of cloud boundaries, the 1km MODIS LWP values surrounding several westward-moving cloud boundaries, one of which is shown in Figure 3.16, do not indicate increased LWP being associated with the boundaries. A more robust analysis of the liquid water path of the cloud field in the vicinity of the cloud boundaries would help constrain this cloud enhancement issue, and is left for future work.

Kelvin Helmholtz instability may contribute to the entrainment of dry air from the free troposphere into the marine low cloud layer local to the gravity waves. Koch et al. (2008) observed mixing taking place with a bore and associated wave trains in the central US. Future work is needed to determine if Kelvin Helmholtz instability is plausible in the local environment of the gravity waves in the southeast Atlantic (e.g. as in Martner and Ralph, 1993), and whether the results of the Koch et al. (2008) study are applicable to the southeast Atlantic marine stratocumulus environment. It is hypothesized that the entrainment of dry air into the cloud deck from the free troposphere and the subsequent erosion of cloud offsets the enhancement of cloud that

would be expected from the upward displacement of the top of the boundary layer from a bore passage (e.g. Martin and Johnson, 2008).

## **5.) Conclusions**

The occurrence of previously undocumented, sharp, propagating (assuming they are indeed the result of gravity waves) transitions in cloudiness in the subtropical southeast Atlantic marine stratocumulus have been documented using MODIS corrected reflectance data and visible and infrared brightness temperature (IR) data from polar-orbiting or geosynchronous satellites. Satellite data were used to determine the monthly frequency occurrence of the cloud-eroding gravity waves, their direction and speed, and when and where they move away from the subtropical western coast of Africa. Reanalysis data and sparsely available upper air data have been used to contrast the regional meteorological conditions prevalent in the months when the most and fewest sharp cloudiness transitions occur. Our main findings are:

- Cloud-eroding waves occur year round, with a maximum frequency in May (roughly 20 days with cloud boundaries per month, ~ 65% daily probability) and a minimum frequency in January (between 1 and 2 days with cloud boundaries per month, ~ 5% daily probability).
- Cloudiness transitions become discernable along the coast of southwestern Africa, generally within a few hours of local midnight and move westward at ~ 10 m/s.

The westward-propagating erosion of cloud is very likely due to a gravity wave rather than advection (hence the use of the term 'propagating') since prevailing low-level flow is from the south. Based on data sets analyzed, we propose that the gravity waves are triggered by the interaction of offshore flow (likely combining the nocturnal land breeze and downslope winds) and the stable marine boundary layer in a manner similar to previously-documented cloud-forming gravity waves (e.g. Birch and Reeder, 2013). The only operational sounding in the area is over 1,800 km offshore at St. Helena Island. Calculations of the Brunt Väisälä frequency across the marine boundary layer inversion layer indicate it could serve as a wave guide. Future observations taken by

either in situ measurements or next-generation satellite soundings (e.g. COSMIC-2, see: <http://www.cosmic.ucar.edu/cosmic2/index.html>, which should provide enhanced measurements over those of the current COSMIC mission) will be used to confirm the presence of a wave guide in the near-shore environment, and future modeling studies are also planned to test this hypothesis using a mesoscale model.

The mechanism for the dramatic cloud erosion associated with these gravity waves is speculative based on limited observations. The values of the Richardson number from St. Helena Island upper air soundings during May unsurprisingly indicate conditions unlikely to support mechanically induced turbulence in the background environment which would aid entrainment of dry air. We hypothesize the mechanism of erosion to be entrainment of warm and dry air from the free troposphere into the cloud layer by turbulence and mixing associated with the bore and trailing gravity waves (as in Koch et al., 2008), and that this entrainment drying offsets any enhancement of the cloud deck that might be caused by upward displacement associated with a bore passage. Future modeling studies would be very helpful in refining this conceptual model.

Examination of visible and IR time sequences throughout the year (not shown) reveal frequent gravity-wave like perturbations to the cloud field in the southeast Atlantic from multiple directions (e.g. section 3.1.3). We infer that gravity waves are common year-round but that the marine low cloudiness conditions in the subtropical southeast Atlantic in May are particularly susceptible to erosion by gravity wave perturbations. These persistent, wide area reductions in cloud fraction may likely contribute to lower cloud fraction in the March-April-May season in the southeast Atlantic compared to any season in the southeast Pacific or the northeast Pacific (Burleyson and Yuter, 2015b).

Painemal et al. (2014) found that the southeast Atlantic stratocumulus deck is thinner than that in the southeast Pacific (on the order of 200 meters thinner for the region they examined), implying a greater susceptibility to gravity wave erosion in general. Comparison of large scale meteorological conditions reveals that inversion strength, SST, and large scale subsidence conditions in May (local fall) are

unsurprisingly in between those of the summer and winter seasons. This may indicate that there is a particular set of environmental conditions that overlap to generate a ‘Goldilocks’ condition under which cloud erosion by gravity waves is very likely. The underlying reasons why the May southeast Atlantic clouds are more susceptible to erosion are a topic for future modeling and observational studies.

Aircraft measurements from both the cloudy and clear side of the transition (as in Crosbie et al., 2016) could confirm that neither advection nor changes in aerosol concentration are major players in the erosion of cloud. In situ measurements (e.g. Lenschow et al., 2000; Katzwinkel et al., 2012) and remote sensing measurements (e.g. Martner and Ralph, 1993) at the interface of the cloud top and free troposphere during gravity wave passage could also help constrain the nature of entrainment of warm and dry air into the cloud layer and the potential role of Kelvin Helmholtz instability. The NCAR C-130 aircraft equipped with dropsondes, a cloud radar, and a lidar would be an ideal tool to follow and sample the cloud-eroding boundaries as they move westward from the southwestern African coast.

Future investigations could also benefit from the development of westward-moving cloud erosion detection algorithms, which would enable rapid quantification of the frequency of these cloud clearings as well as robust estimates of the net impact that the cloudiness transitions have on climatological cloud fraction, and thus the radiation budget. The inter-annual variability in the frequency of these cloudiness transitions is also an open question that could be answered with such a methodology. We have insufficient information to speculate if the frequency of the cloud-eroding waves and associated rapid areal reduction in low cloud fractions in the southeast Atlantic would increase or decrease in a warming climate.

## REFERENCES

- Ahrens, C. D. (2009). *Meteorology Today*. (J. Warde, Ed.) (9th ed.). Brooks/Cole.
- Allen, G., Vaughan, G., Toniazzo, T., Coe, H., Connolly, P., Yuter, S. E., ... Ayers, J. K. (2012). Gravity-wave-induced perturbations in marine stratocumulus. *Quarterly Journal of the Royal Meteorological Society*, 139(670), 32–45. doi:10.1002/qj.1952
- Atkinson, B. W., & Wu Zhang, J. (1996). Mesoscale shallow convection in the atmosphere. *Reviews of Geophysics*, 34(4), 403. doi:10.1029/96RG02623
- Bender, F. A. M., Charlson, R. J., Ekman, A. M. L., & Leahy, L. V. (2011). Quantification of monthly mean regional-scale albedo of marine stratiform clouds in satellite observations and GCMs. *Journal of Applied Meteorology and Climatology*, 50(10), 2139–2148. doi:10.1175/JAMC-D-11-049.1
- Birch, C. E., & Reeder, M. J. (2013). Wave-cloud lines over northwest Australia. *Quarterly Journal of the Royal Meteorological Society*, 139, 1311–1326. doi:10.1002/qj.2043
- Blanc, E., Farges, T., Le Pichon, A., & Heinrich, P. (2014). Ten year observations of gravity waves from thunderstorms in western Africa. *Journal of Geophysical Research: Atmospheres*, 119, 2013JD020499. doi:10.1002/2013JD020499
- Bony, S., Colman, R., Kattsov, V. M., Allan, R. P., Bretherton, C. S., Dufresne, J. L., ... Webb, M. J. (2006). How well do we understand and evaluate climate change feedback processes? *Journal of Climate*, 19(15), 3445–3482. doi:10.1175/JCLI3819.1
- Burleyson, C. D., de Szoeke, S. P., Yuter, S. E., Wilbanks, M., & Brewer, W. A. (2013). Ship-Based Observations of the Diurnal Cycle of Southeast Pacific Marine Stratocumulus Clouds and Precipitation. *Journal of the Atmospheric Sciences*, 70(12), 3876–3894. doi:10.1175/JAS-D-13-01.1
- Burleyson, C. D., & Yuter, S. E. (2015a). Patterns of Diurnal Marine Stratocumulus Cloud Fraction Variability\*. *Journal of Applied Meteorology and Climatology*, 54(4), 847–866. doi:10.1175/JAMC-D-14-0178.1
- Burleyson, C. D., & Yuter, S. E. (2015b). Subdiurnal Stratocumulus Cloud Fraction Variability and Sensitivity to Precipitation\*. *Journal of Climate*, 28(8), 2968–2985. doi:10.1175/JCLI-D-14-00648.1
- Christie, D. R. (1992). The morning glory of the Gulf of Carpentaria: a paradigm for non-linear waves in the lower atmosphere. *Australian Meteorology Magazine*, 41, 21–60.
- Clarke, R. H. (1972). The Morning Glory: An atmospheric hydraulic jump. *Journal of Applied Meteorology*, 11, 304–311.

- Clarke, R. H., Smith, R. K., & Reid, D. G. (1981). The Morning Glory of the Gulf of Carpentaria: An atmospheric undular bore. *Monthly Weather Review*, 109, 1726–1750.
- Connolly, P. J., Vaughan, G., Cook, P., Allen, G., Coe, H., Choularton, T. W., ... Hill, A. (2013). Modelling the effects of gravity waves on stratocumulus clouds observed during VOCALS-UK. *Atmospheric Chemistry and Physics*, 13, 7133–7152. doi:10.5194/acp-13-7133-2013
- Crosbie, E., Wang, Z., Sorooshian, A., Chuang, P. Y., Craven, J. S., Coggon, M. M., ... Seinfeld, J. H. (2016). Stratocumulus Cloud Clearings and Notable Thermodynamic and Aerosol Contrasts across the Clear–Cloudy Interface. *Journal of the Atmospheric Sciences*, 73(3), 1083–1099. doi:10.1175/JAS-D-15-0137.1
- Da Silva, J. C. B., & Magalhaes, J. M. (2009). Satellite observations of large atmospheric gravity waves in the Mozambique Channel. *International Journal of Remote Sensing*, 30, 1161–1182. doi:Doi 10.1080/01431160802448943\rPii 910309973
- de Szoeke, S. P., Verlinden, K. L., Yuter, S. E., & Mechem, D. B. (2016). The time scales of variability of marine low clouds. *Journal of Climate*, in press.
- Désalmand, F., Szantai, A., Picon, L., & Desbois, M. (2003). Systematic observation of westward propagating cloud bands over the Arabian Sea during Indian Ocean Experiment (INDOEX) from Meteosat-5 data. *Journal of Geophysical Research*, 108(D18), 1–11. doi:10.1029/2002JD002934
- Durran, D., & Klemp, J. (1982). On the Effects of Moisture on the Brunt-Vaisala Frequency. *Journal of Atmospheric Sciences*, 39, 2152–2158.
- Engstrom, A., Bender, F. A. M., & Karlsson, J. (2014). Improved representation of marine stratocumulus cloud shortwave radiative properties in the CMIP5 climate models. *Journal of Climate*, 27(16), 6175–6188. doi:10.1175/JCLI-D-13-00755.1
- Fovell, R. G., Mullendore, G. L., & Kim, S. H. (2006). Discrete Propagation in Numerically Simulated Nocturnal Squall Lines. *Monthly Weather Review*, 134, 3735–3752.
- Garreaud, R. D., & Munoz, R. (2004). The Diurnal Cycle in Circulation and Cloudiness over the Subtropical Southeast Pacific : A Modeling Study. *Journal of Climate*, 17, 1699–1710.
- Gille, S. T., Smith, L., & Stom, N. M. (2005). Global observations of the land breeze. *Geophysical Research Letters*, 32, L05605. doi:10.1029/2004GL022139
- Goler, R. a., & Reeder, M. J. (2004). The Generation of the Morning Glory. *Journal of the Atmospheric Sciences*, 61(12), 1360–1376. doi:10.1175/1520-0469(2004)061<1360:TGOTMG>2.0.CO;2

Hartmann, D. L., Ockert-Bell, M. E., & Michelsen, M. L. (1992). The effect of cloud type on Earth's energy balance: Global analysis. *Journal of Climate*. doi:10.1175/1520-0442(1992)005<1281:TEOCTO>2.0.CO;2

Hoflich, O. (1984) Climate of the South Atlantic Ocean. In: *World Survey of Climatology, Volume 15, Climates of the Oceans*, H. Van Loon, editor, Elsevier, Amsterdam, 1-191.

Holton, J. R., & Hakim, G. J. (2013). *An introduction to Dynamic Meteorology* (5th ed.). Waltham, MA: Elsevier.

IPCC, 2013: *Climate Change 2013: The Physical Science Basis. Contribution of Working Group I to the Fifth Assessment Report of the Intergovernmental Panel on Climate Change* [Stocker, T.F., D. Qin, G.-K. Plattner, M. Tignor, S.K. Allen, J. Boschung, A. Nauels, Y. Xia, V. Bex and P.M. Midgley (eds.)].

Janowiak, J. E., Joyce, R. J., & Yarosh, Y. (2001). A real-time global half-hourly pixel-resolution infrared dataset and its applications. *Bulletin of the American Meteorological Society*, 82(2), 205–217. doi:10.1175/1520-0477(2001)082<0205:ARTGHH>2.3.CO;2

Jiang, H., Farrar, J. T., Beardsley, R. C., Chen, R., & Chen, C. (2009). Zonal surface wind jets across the Red Sea due to mountain gap forcing along both sides of the Red Sea. *Geophysical Research Letters*, 36(19), L19605. doi:10.1029/2009GL040008

Jiang, Q., & Wang, S. (2012). Impact of Gravity Waves on Marine Stratocumulus Variability. *Journal of the Atmospheric Sciences*, 69, 3633–3651. doi:10.1175/JAS-D-12-0135.1

Katzwinkel, J., Siebert, H., & Shaw, R. A. (2012). Observation of a Self-Limiting, Shear-Induced Turbulent Inversion Layer Above Marine Stratocumulus. *Boundary-Layer Meteorology*, 145, 131–143. doi:10.1007/s10546-011-9683-4

Kidder, S. Q., & Vonder Haar, T. H. (1995). *Satellite Meteorology: an introduction*. San Diego: Academic Press.

Klein, S. H., & Hartmann, D. L. (1993). The seasonal cycle of low stratiform clouds. *Journal of Climate*, 6, 1587–1606.

Kloesel, K. A. (1992). Marine stratocumulus cloud clearing episodes observed during FIRE. *Monthly Weather Review*, 120, 565–578.

Koch, S. E., Feltz, W., Fabry, F., Pagowski, M., Geerts, B., Bedka, K. M., ... Wilson, J. W. (2008). Turbulent Mixing Processes in Atmospheric Bores and Solitary Waves Deduced from Profiling Systems and Numerical Simulation. *Monthly Weather Review*, 136, 1373–1400. doi:10.1175/2007MWR2252.1

Kondo, J., Kanechika, O., & Yasuda, N. (1978). Heat and Momentum Transfers under Strong Stability in the Atmospheric Surface Layer. *Journal of the Atmospheric Sciences*, 35(6), 1012–1021. doi:10.1175/1520-0469(1978)035<1012:HAMTUS>2.0.CO;2

Lenschow, D. H., Zhou, M., Zeng, X., Chen, L., & Xu, X. (2000). Measurements of fine-scale structure at the top of marine stratocumulus. *Boundary-Layer Meteorology*, 97, 331–357.

Lindsay, J. A., & Tyson, P. D. (1990). Thermo-topographically induced boundary layer oscillations over the central Namib, Southern Africa. *International Journal of Climatology*, 10, 63–77.

Lohmann, U., & Feichter, J. (2005). Global indirect aerosol effects: a review. *Atmospheric Chemistry and Physics*, 5(3), 715–737. doi:10.5194/acp-5-715-2005

Magalhaes, J. M., Araújo, I. B., Da Silva, J. C. B., Grimshaw, R. H. J., Davis, K., & Pineda, J. (2011). Atmospheric gravity waves in the Red Sea: A new hotspot. *Nonlinear Processes in Geophysics*, 18, 71–79. doi:10.5194/npg-18-71-2011

Mapes, B. E. (1993). Gregarious Tropical Convection. *Journal of Atmospheric Chemistry*, 50(13), 2026–2037.

Markowski, P., & Richardson, Y. (2010). *Mesoscale Meteorology in Midlatitudes* (1st ed.). Chichester, UK: Wiley-Blackwell.

Martin, E. R., & Johnson, R. H. (2008). An Observational and Modeling Study of an Atmospheric Internal Bore during NAME 2004. *Monthly Weather Review*, 136(11), 4150–4167. doi:10.1175/2008MWR2486.1

Martner, B. E., & Ralph, F. M. (1993). Breaking Kelvin-Helmholtz waves and cloud-top entrainment as revealed by K-band Doppler Radar. In *Ninth conference on atmospheric and oceanic waves and stability* (pp. 71–74).

Medeiros, B., Williamson, D. L., Hannay, C., & Olson, J. G. (2012). Southeast Pacific Stratocumulus in the Community Atmosphere Model. *Journal of Climate*, 25(18), 6175–6192. doi:10.1175/JCLI-D-11-00503.1

Met Office (2007): Met Office St Helena Bottoms Wood station high resolution radiosonde data. NCAS British Atmospheric Data Centre, 2016/03/25. <http://catalogue.ceda.ac.uk/uuid/f7f3478135e81472e056889935d284d7>

Miller, M. A., & Yuter, S. E. (2013). Detection and characterization of heavy drizzle cells within subtropical marine stratocumulus using AMSR-E 89-GHz passive microwave measurements. *Atmospheric Measurement Techniques*, 6(1), 1–13. doi:10.5194/amt-6-1-2013

Miller, M.A. et al. (2016) In preparation.

Müller, J., & Et, A. (2013). MSG 1.5 Image Data Format Description. Darmstadt, Germany.

Myers, T. a, & Norris, J. R. (2013). Observational Evidence That Enhanced Subsidence Reduces Subtropical Marine Boundary Layer Cloudiness. *Journal of Climate*, 26, 7507–7524. doi:10.1175/JCLI-D-12-00736.1

O'Dell, C. W., Wentz, F. J., & Bennartz, R. (2008). Cloud Liquid Water Path from Satellite-Based Passive Microwave Observations: A New Climatology over the Global Oceans. *Journal of Climate*, 21(8), 1721–1739. doi:10.1175/2007JCLI1958.1

Painemal, D., Xu, K., Cheng, A., Minnis, P., & Palikonda, R. (2014). Mean Structure and Diurnal Cycle of Southeast Atlantic Boundary Layer Clouds : Insights from Satellite Observations and Multiscale Modeling Framework Simulations. *Journal of Climate*, 324–341. doi:10.1175/JCLI-D-14-00368.1

Parker, M. D. (2008). Response of Simulated Squall Lines to Low-Level Cooling. *Journal of the Atmospheric Sciences*. doi:10.1175/2007JAS2507.1

Peterson, R. G., & Stramma, L. (1991). Upper-level circulation in the South Atlantic Ocean. *Progress in Oceanography*, 26(1), 1–73. doi:10.1016/0079-6611(91)90006-8

Rahn, D. a., & Garreaud, R. D. (2009). Marine boundary layer over the subtropical southeast Pacific during VOCALS-REx – Part 2: Synoptic variability. *Atmospheric Chemistry and Physics Discussions*, 9(6), 26063–26094. doi:10.5194/acpd-9-26063-2009

Reynolds, R. W., & Smith, T. M. (1994). Improved global sea surface temperature analyses using optimum interpolation. *Journal of Climate*. doi:10.1175/1520-0442(1994)007<0929:IGSSTA>2.0.CO;2

Rienecker, M. M., Suarez, M. J., Gelaro, R., Todling, R., Bacmeister, J., Liu, E., ... Woollen, J. (2011). MERRA: NASA's Modern-Era Retrospective Analysis for Research and Applications. *Journal of Climate*, 24(14), 3624–3648. doi:10.1175/JCLI-D-11-00015.1

Sharon, T. M., Albrecht, B. A., Jonsson, H. H., Minnis, P., Khaiyer, M. M., van Reken., T. M., ... Flagan., R. (2006). Aerosol and cloud microphysical characteristics of rifts and gradients in maritime stratocumulus clouds. *Journal of Atmospheric Sciences*, 63, 983–997.

Smith, R. K. (1986). Evening glory wave-cloud lines in northwestern Australia. *Australian Meteorology Magazine*, 34, 27–33.

Stevens, B., Vali, G., Comstock, K., Wood, R., van Zanten, M. C., Austin, P. H., ... Lenschow, D. H. (2005). Pockets of open cells and drizzle in marine stratocumulus. *Bulletin of the American Meteorological Society*, 86(1), 51–57. doi:10.1175/BAMS-86-1-51

Veitch, J. A., Florenchie, P., & Shillington, F. A. (2006). Seasonal and interannual fluctuations of the Angola Benguela Frontal Zone ( ABFZ ) using 4.5 km resolution satellite imagery from 1982 to 1999. *International Journal of Remote Sensing*, 27(5), 1–25. doi:10.1080/01431160500127914

## APPENDICES

## Appendix A

This appendix contains captions for the animations contained in the thesis. All animations can be found through the following link:

<https://drive.google.com/drive/folders/0B1MpXAEMo1KBYnFsWnVHcVVCSXM>

Animation 3.6: 15 minute Meteosat visible imagery animation for 08 April, 2013 from 05:12 to 19:42 UTC.

Animation 3.7: 15 minute Meteosat visible imagery animation for 26 May, 2014 from 05:12 to 19:57 UTC.

Animation 3.8: 15 minute Meteosat visible imagery animation for 05 May, 2014 from 05:12 to 19:57 UTC.

Animation 3.9: 15 minute Meteosat visible imagery animation for 26 May 2012 from 03:27 to 17:27 UTC showing the locations of discrete cloud elements through the animation.

Animation 3.11: 30 minute merged infrared 12  $\mu\text{m}$  brightness temperatures for the two day period from 13 June 2014 00:00 UTC to 14 June 2014 23:30 UTC. Red denotes missing data.

Animation 3.12: 30 minute merged infrared 12  $\mu\text{m}$  brightness temperatures for the two day period from 25 May 2014 00:00 UTC to 26 May 2014 23:30 UTC. Red denotes missing data.

Animation 3.14: Zoomed-in 15 minute Meteosat visible imagery animation for 26 May, 2014 from 05:12 to 19:57 UTC.

Animation 3.15: Zoomed-in 15 minute Meteosat visible imagery animation for 05 May, 2014 from 05:12 to 19:57 UTC.

Animation 3.18: Zoomed-in 15 minute Meteosat visible imagery animation for 23 June, 2014 from 05:12 to 19:57 UTC. Gravity waves of interest are highlighted with a yellow oval.

Animation 3.19: Zoomed-in 15 minute Meteosat visible imagery animation for 12 May, 2015 from 05:12 to 19:57 UTC. Gravity waves of interest are highlighted with a yellow oval.

Animation 3.23: Animation of the annual cycle in the monthly-averaged MERRA reanalysis sea level pressure and wind vectors at 1000 hPa for the period 01 January 2000 through 31 December 2015.

Animation 3.24: Animation of the annual cycle in monthly-averaged MERRA estimated inversion strength (EIS, see Section 2.3) for the period 01 January 2000 through 31 December 2015. Gray denotes missing data.

Animation 3.25: Animation of the annual cycle in the monthly-averaged MERRA reanalysis pressure vertical velocity at 700 hPa for the period 01 January 2000 through 31 December 2015

Animation 4.6: 30 minute merged infrared 12  $\mu\text{m}$  brightness temperatures for the two day period from 01 August 2014 00:00 UTC to 02 August 2014 23:30 UTC. Red denotes missing data. The approximate location of Gobabeb, Namibia is denoted by a yellow star.

## Appendix B

Figure B1 shows a side-by-side comparison of the monthly frequency of 'yes', 'no', and 'maybe' cloud boundary days determined from the cloud boundary climatology (see Sections 2.2 and 3.2 for details). The frequency occurrence of 'no' days (panel b) is quite high year-round (above 15 days per month for all months except May which sees roughly 7 'no' days per month) with a noticeable minimum between April and June. This corresponds to the time period when cloud boundaries are most frequently occurring. 'Maybe' days occur very infrequently, with most months seeing around 1 or fewer 'maybe' days per month with the exception of May and June, on which roughly 3 and 2 (respectively) maybe days occur per month.

Table 1.1: Various known transitions in marine clouds.

Boundary type	Propagation direction	Impact on cloud	Reference
Pockets of open cells	With the wind	Erodes cloud	Stevens et al. 2005
'Upsidence' wave	Not with the wind	Can enhance but mostly erodes	Garreaud and Muñoz, 2004
Synoptically-induced waves	Not with the wind	Can enhance and erode	Allen et al. 2012
Marine stratocumulus clearings	With the wind	Erodes cloud	Kloesel 1992; Crosbie et al. 2016
Rifts in marine stratocumulus	With the wind	Erodes cloud	Sharon et al., 2006
Southeast Atlantic abrupt cloudiness transitions	Not with the wind	Erodes cloud	Present study

Table 3.1: Estimated radiative impact of various degrees of cloud erosion.

Amount of cloud deck eroded (%)	Area-averaged radiative impact ( $\text{Wm}^{-2}$ )
100	116
75	87
67	78
50	58
33	38
25	29
20	23

Table 4.1: Intrinsic gravity wave phase speeds for various parameter values (in  $\text{ms}^{-1}$ ).  $\lambda_h$  denotes horizontal wavelength,  $\lambda_v$  denotes vertical wavelength, and  $N$  denotes Brunt Väisälä frequency (see Section 4.4).

$\lambda_h$ (km)	$N = 0.04 \text{ s}^{-1}$ $\lambda_v = 1 \text{ km}$	$N = 0.04 \text{ s}^{-1}$ $\lambda_v = 1.75 \text{ km}$	$N = 0.04 \text{ s}^{-1}$ $\lambda_v = 10 \text{ km}$	$N = 0.052 \text{ s}^{-1}$ $\lambda_v = 1 \text{ km}$	$N = 0.052 \text{ s}^{-1}$ $\lambda_v = 1.75 \text{ km}$	$N = 0.052 \text{ s}^{-1}$ $\lambda_v = 10 \text{ km}$
2	5.69	8.38	12.49	7.40	10.89	16.22
5	6.24	10.52	28.47	8.11	13.66	36.98
8	6.32	10.88	39.77	8.21	14.14	51.66

Table 4.2: Estimated density current speed in the vicinity of the southwestern African coast (see Section 4.4).

Density current depth (m)	Density of ambient air ( $\text{kgm}^{-3}$ )	
	1.21	1.17
100	2.85	6.47
500	6.36	14.47

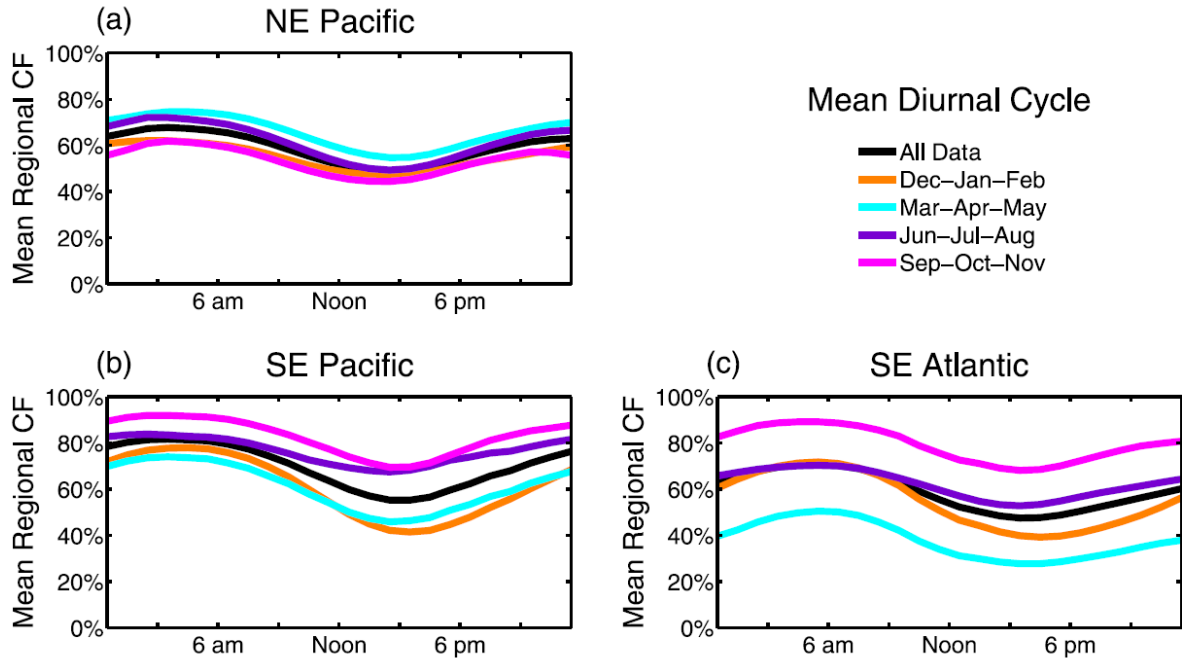


Figure 1.1: The seasonally-averaged diurnal cycle in low cloud fraction for three different marine stratocumulus basins (see Figure 1.2 for a reference map of the area of analysis). From Burleyson and Yuter, 2015b (their Fig. 4).

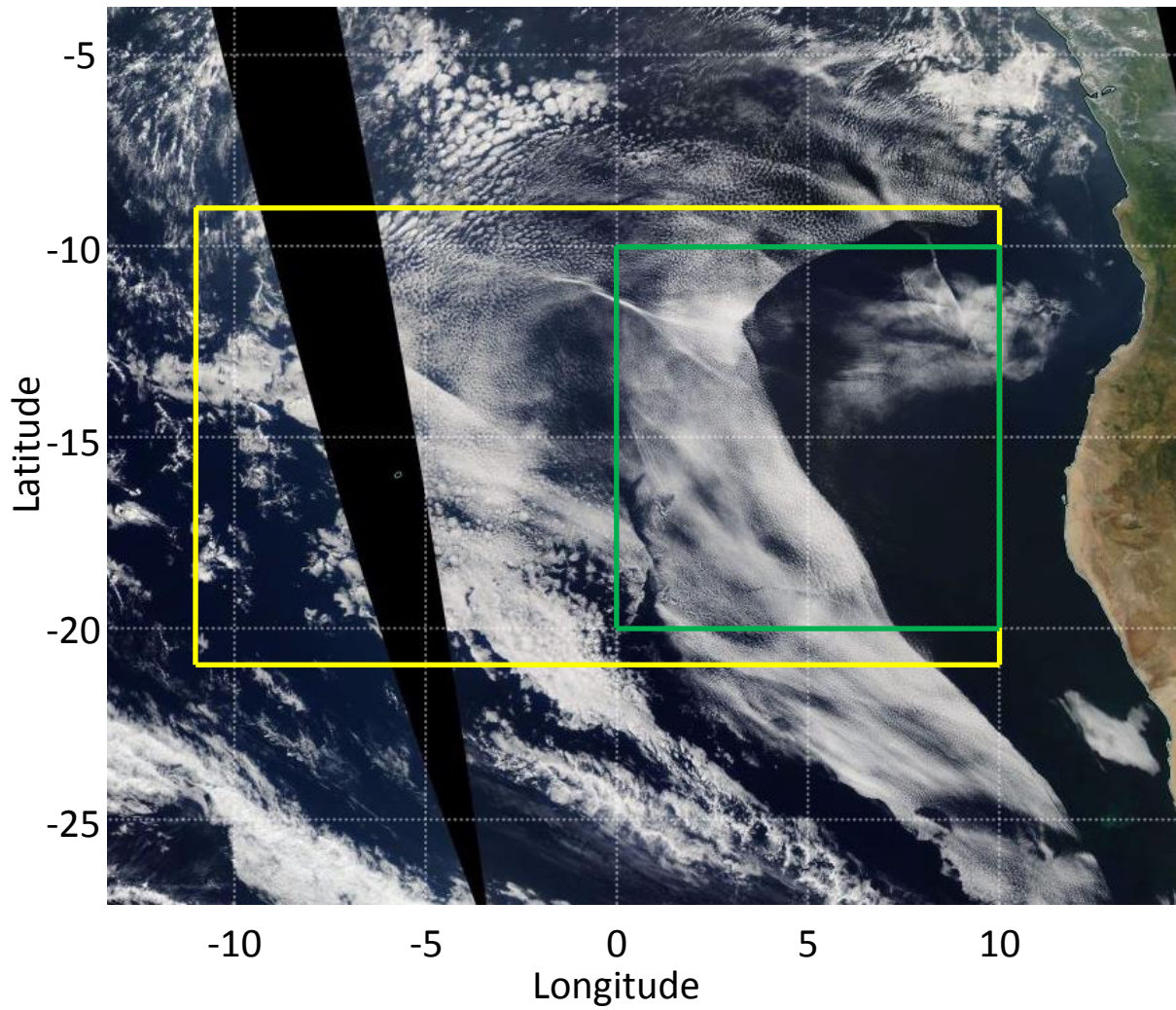


Figure 1.2: Map displaying the regions of analysis for the (green) total cloud fraction climatology of Zhang and Li (2013) and (yellow) the seasonally-averaged diurnal cycle in low cloud fraction of Burleyson and Yuter (2015b). Note the image displays the MODIS corrected reflectance true color image from the Aqua satellite on 26 May 2014 (from <https://worldview.earthdata.nasa.gov>).

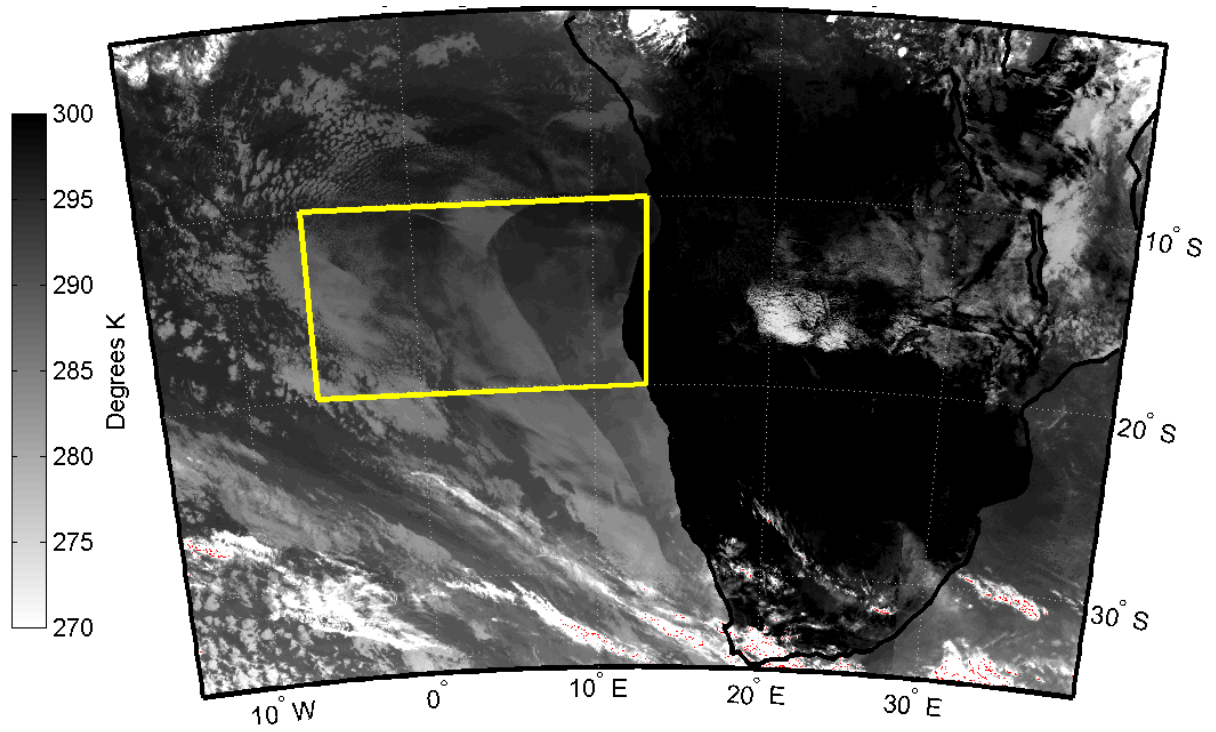


Figure 2.1: Map showing the analysis region (yellow box) over which the IR brightness temperatures were latitudinally averaged to generate the Hovmöller diagrams. This example shows the merged IR data for 26 May 2014 at 11:00 UTC.

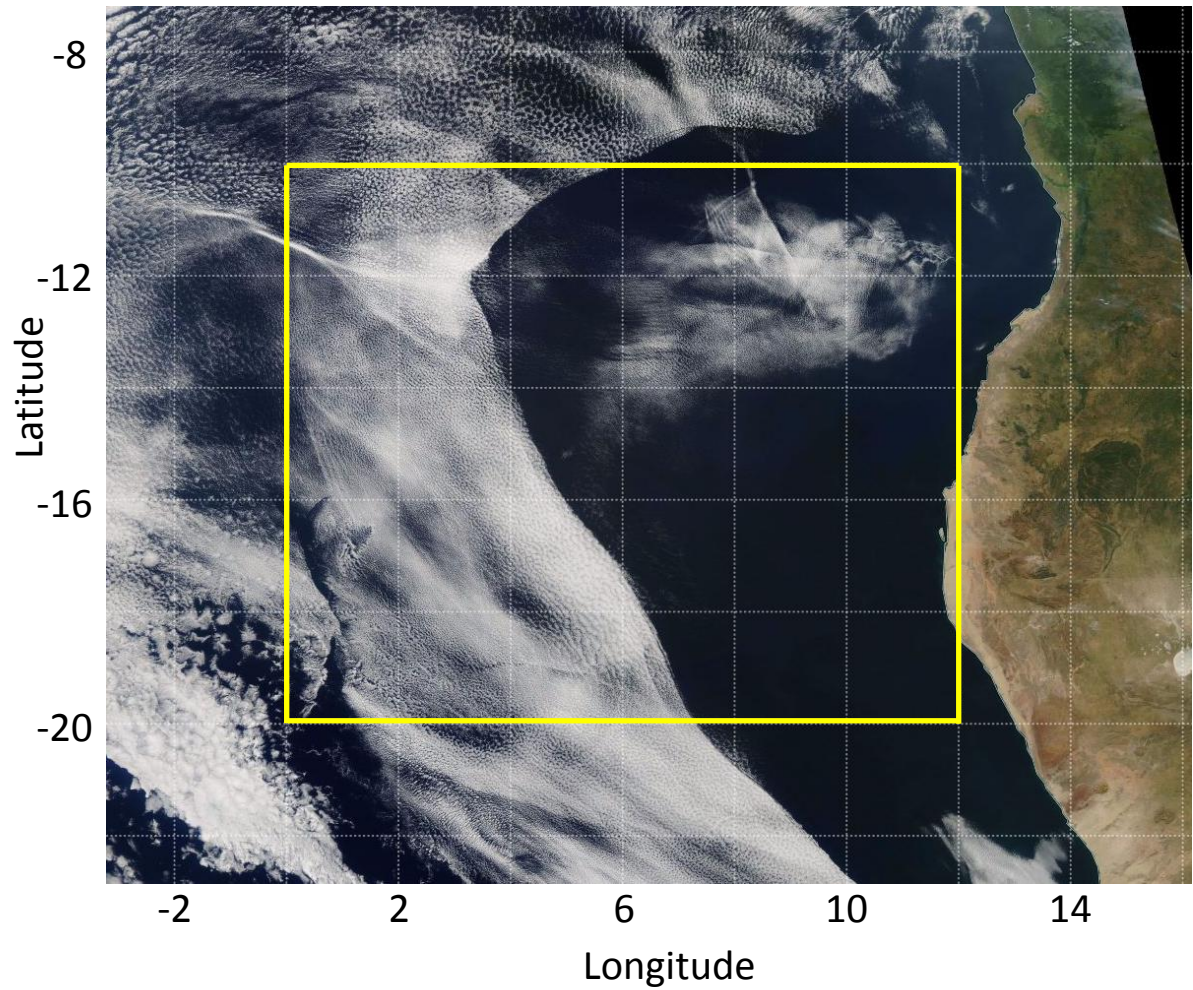


Figure 2.2: Map displaying the area of analysis (yellow box) for the sharp cloud boundary climatology described in section 2.2. The  $2^{\circ} \times 2^{\circ}$  grid boxes are a scale reference for the minimum length requirement for a sharp cloudiness transition. This example shows the MODIS corrected reflectance true color image from the Aqua satellite on 26 May 2014 (from <https://worldview.earthdata.nasa.gov>).

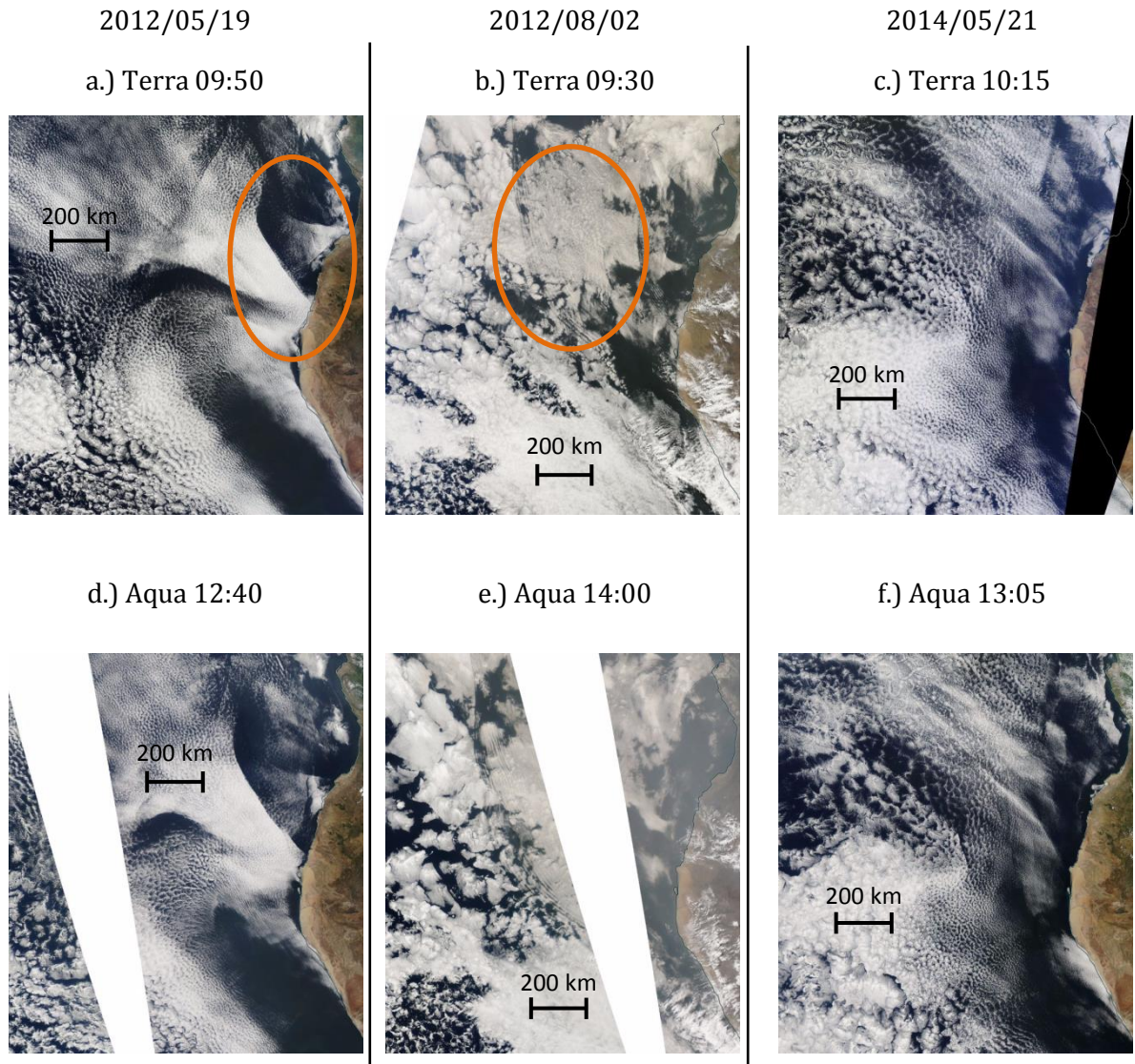


Figure 2.3: Example categorizations of cloud scene pairs in the sharp cloud boundary climatology. Panels a/d show an example of a cloud scene categorized as having a sharp cloud boundary, panels b/e show a ‘no’ categorized scene, and panels c/f show a ‘maybe’ categorized cloud scene. The imaging satellite and the approximate time of overpass are shown above each panel. Note this is only an illustration, and that the manual nature of this categorization does employ some level of subjectivity.

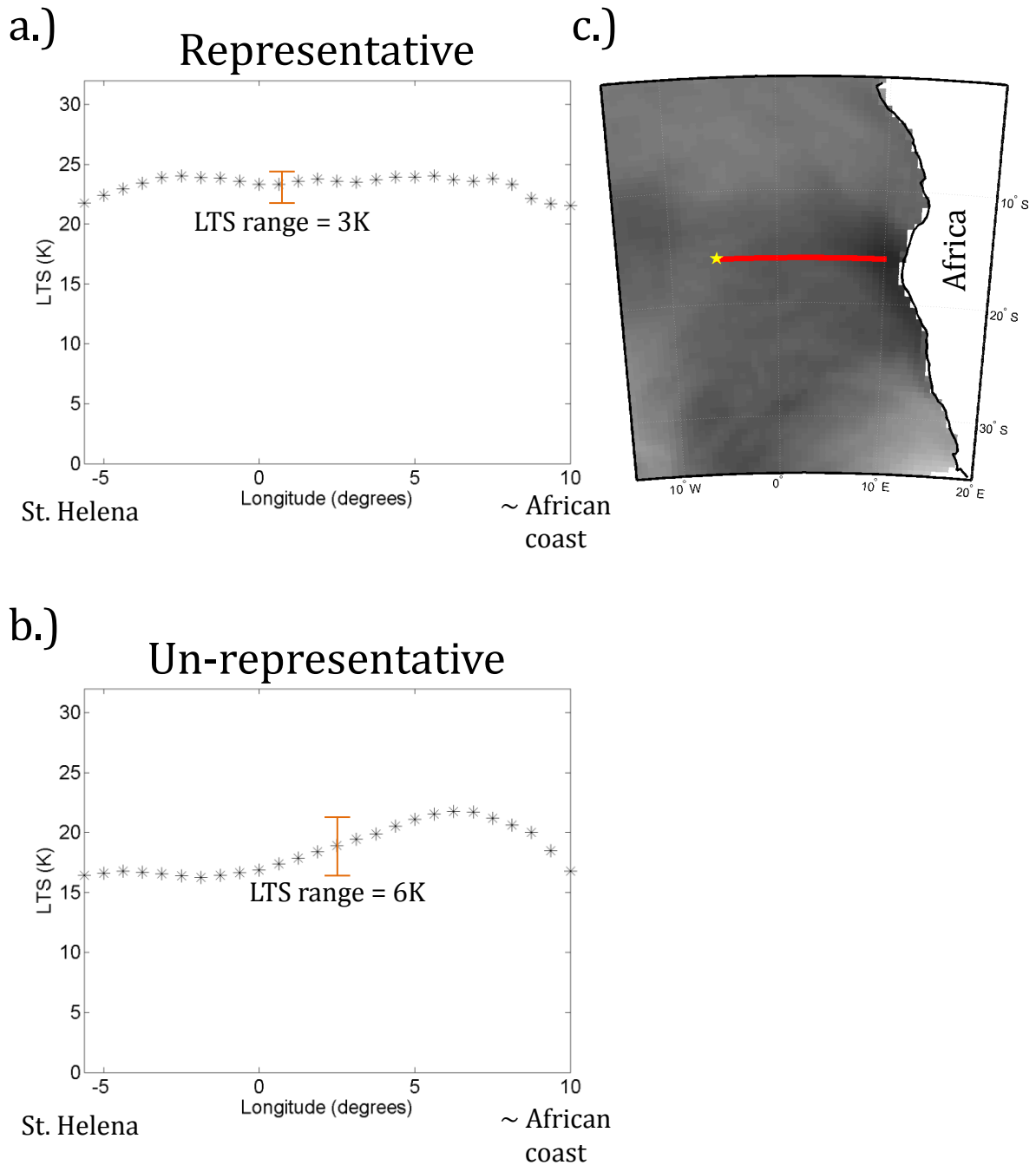


Figure 2.4: Panel a: Lower tropospheric stability (LTS) values between St. Helena and the African coast for an instance where the sounding launched from the Island would be considered 'representative'. Panel b: As in a, but for an 'un-representative' case. Panel c: Diagram showing the location of the transect (red line) between St. Helena (yellow star) and the African coast (black outline) over which the LTS was analyzed.

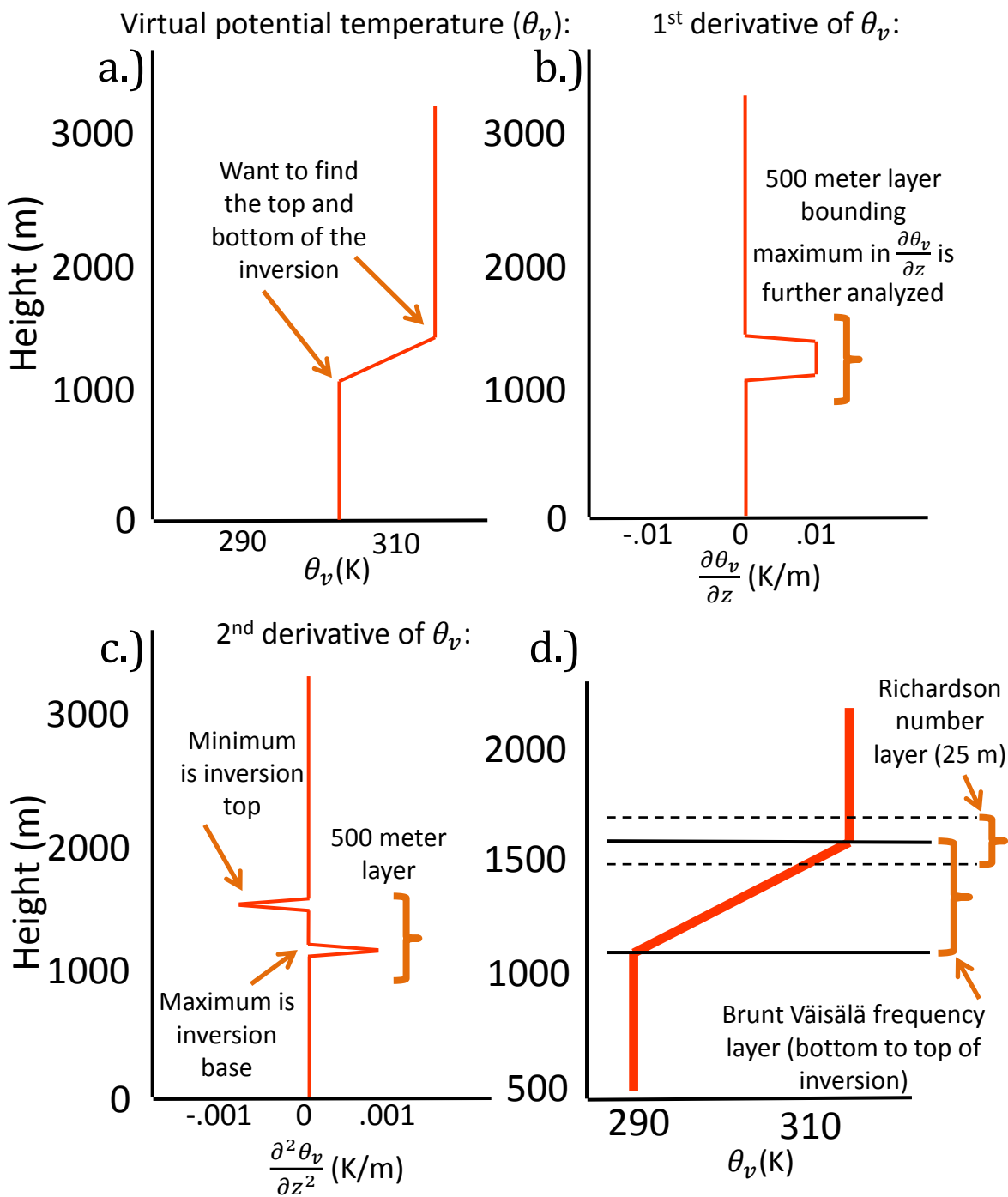


Figure 2.5: Schematic illustration of how the top and bottom of the stable layer is identified using St. Helena sounding data. a.) Virtual potential temperature b.) The first derivative of the virtual potential temperature in panel a with height. c.) The second derivative of the virtual potential temperature in panel a with height. d.) As in panel a, but for the 500 to 2,000 meter layer and with the layers across which the Brunt Väisälä frequency and Richardson number are calculated labeled. The top and bottom of the stable layer are denoted with horizontal black lines.

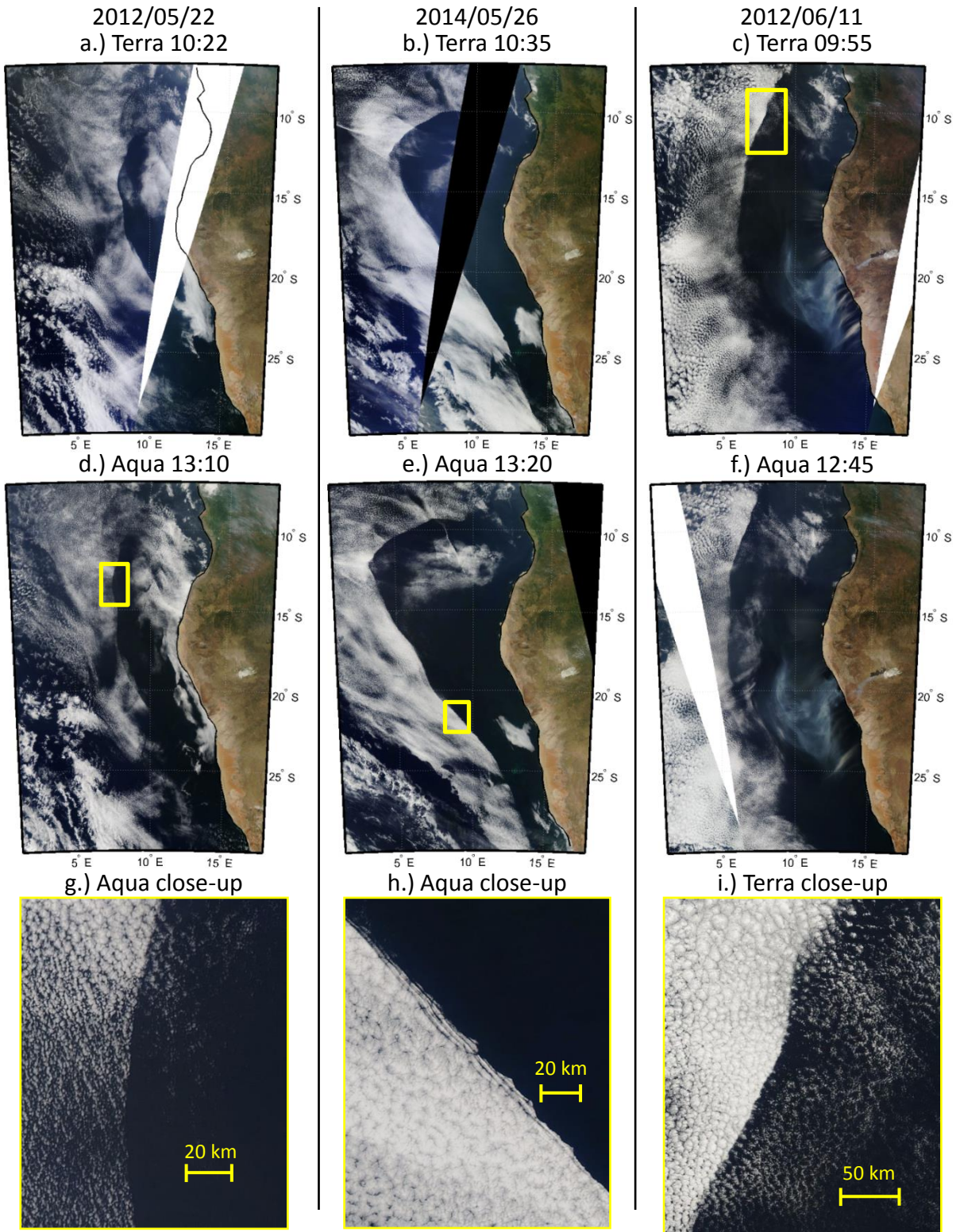


Figure 3.1: Examples of sharp cloud boundaries that resulted in complete clearing of the cloud field identified using MODIS corrected reflectance images. Terra overpass images are displayed in the top row, Aqua overpass images in the second row, and close-ups of either the Aqua or Terra overpass are in the third row. The region of the close-up is denoted by a yellow square in the corresponding satellite image. The approximate overpass times of the images are displayed above each panel.

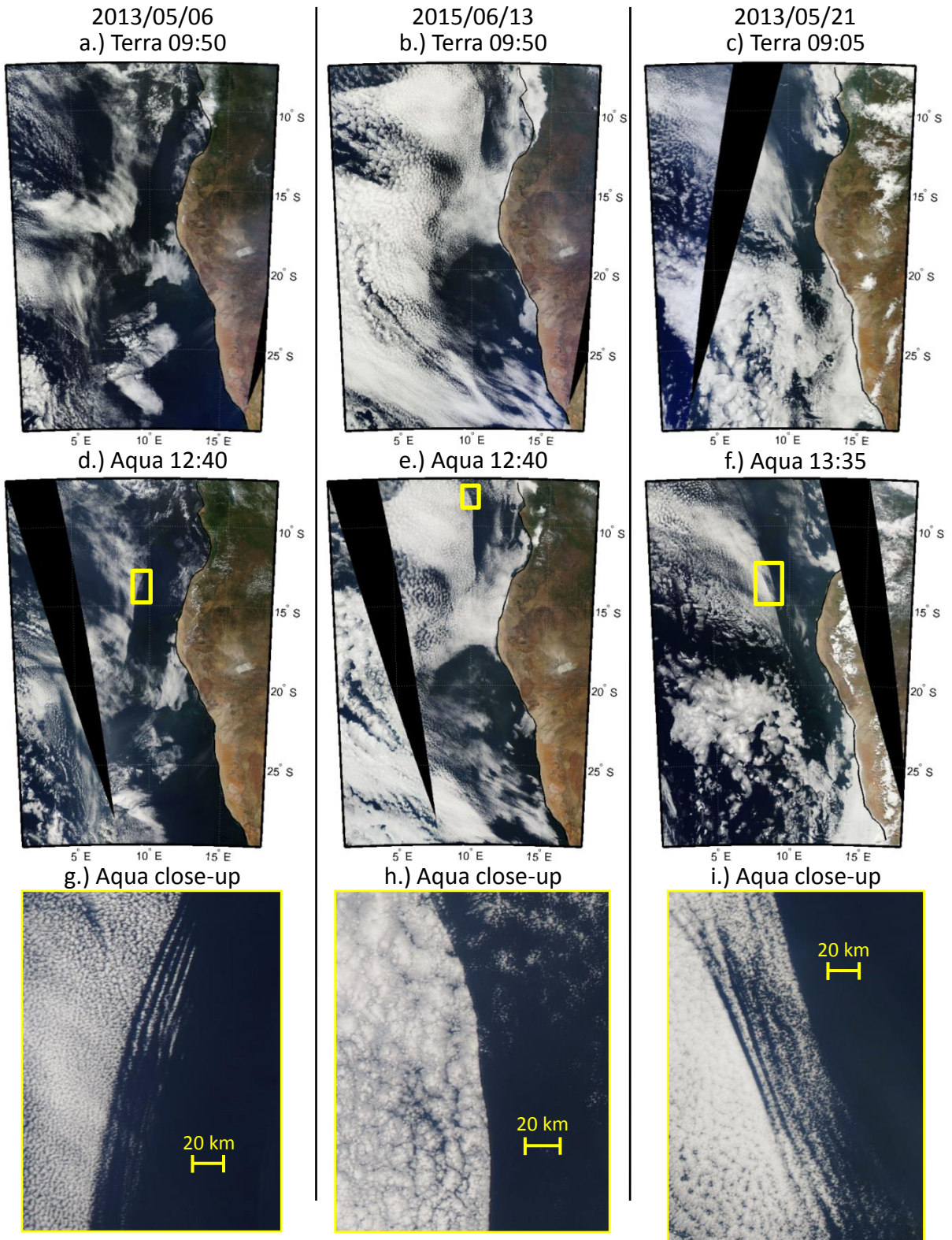


Figure 3.2: As in Figure 3.1, but for three different days.

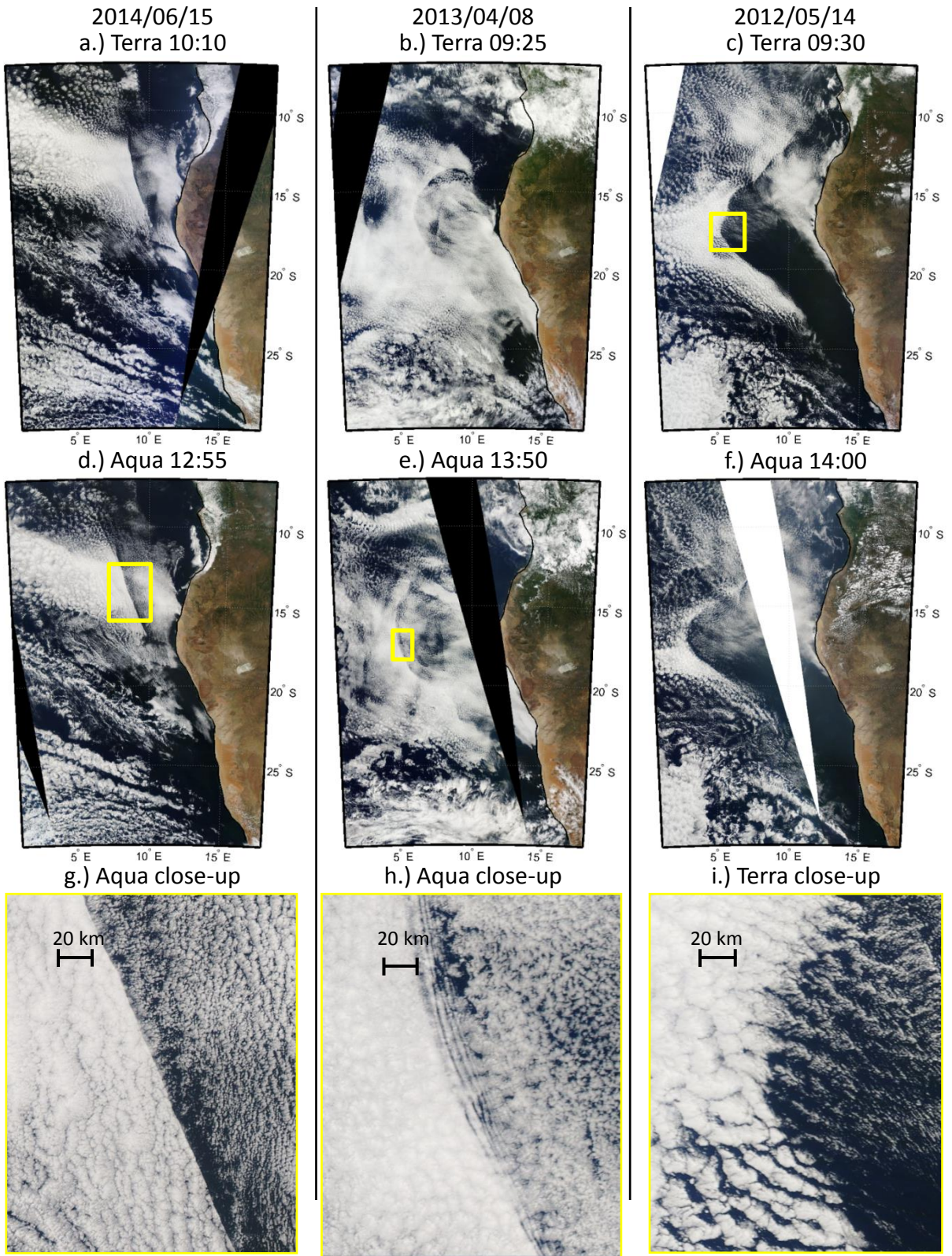


Figure 3.3: As in Figure 3.1, but for sharp cloud boundaries that resulted in partial clearing of the cloud field.

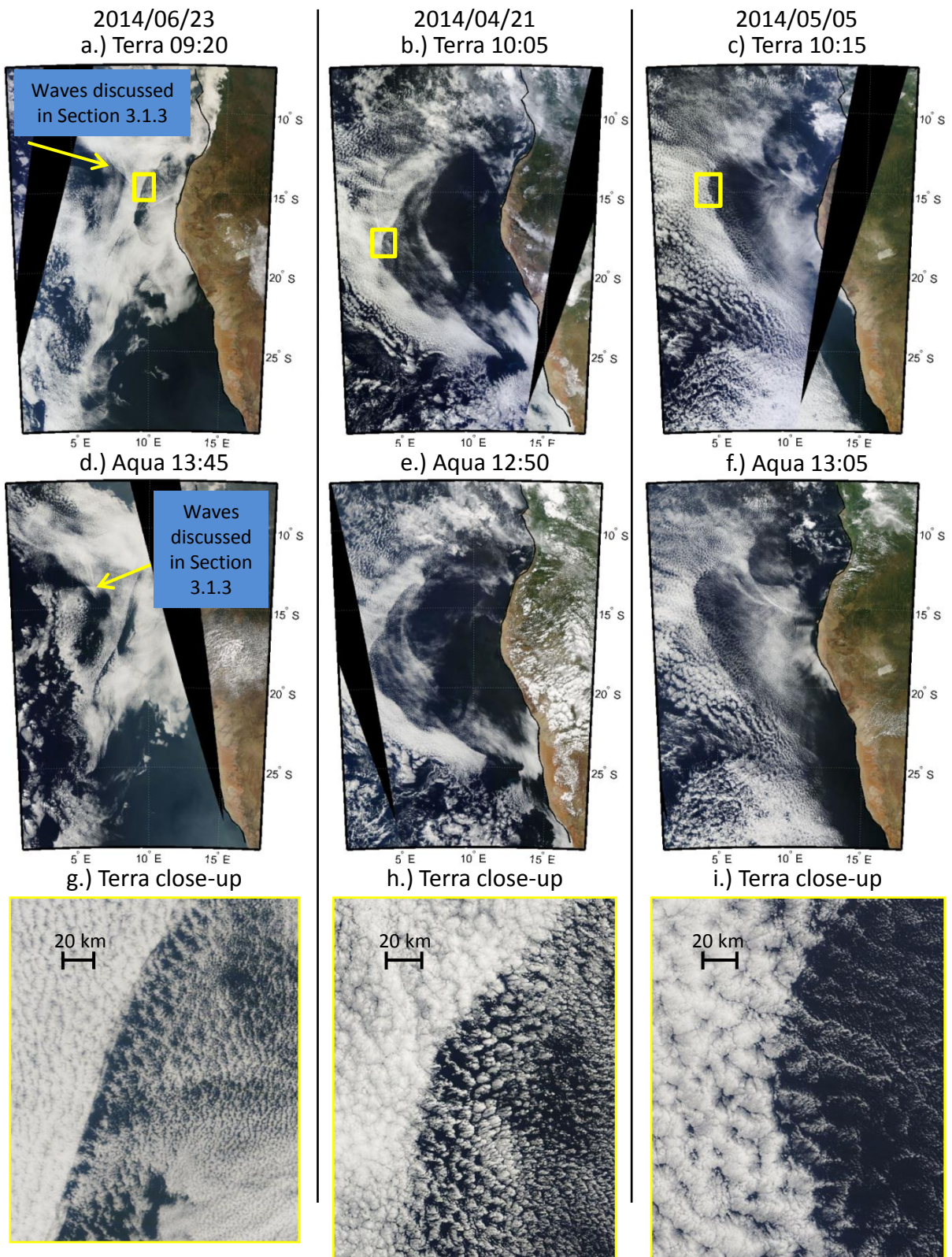


Figure 3.4: As in Figure 3.3, but for three different days.

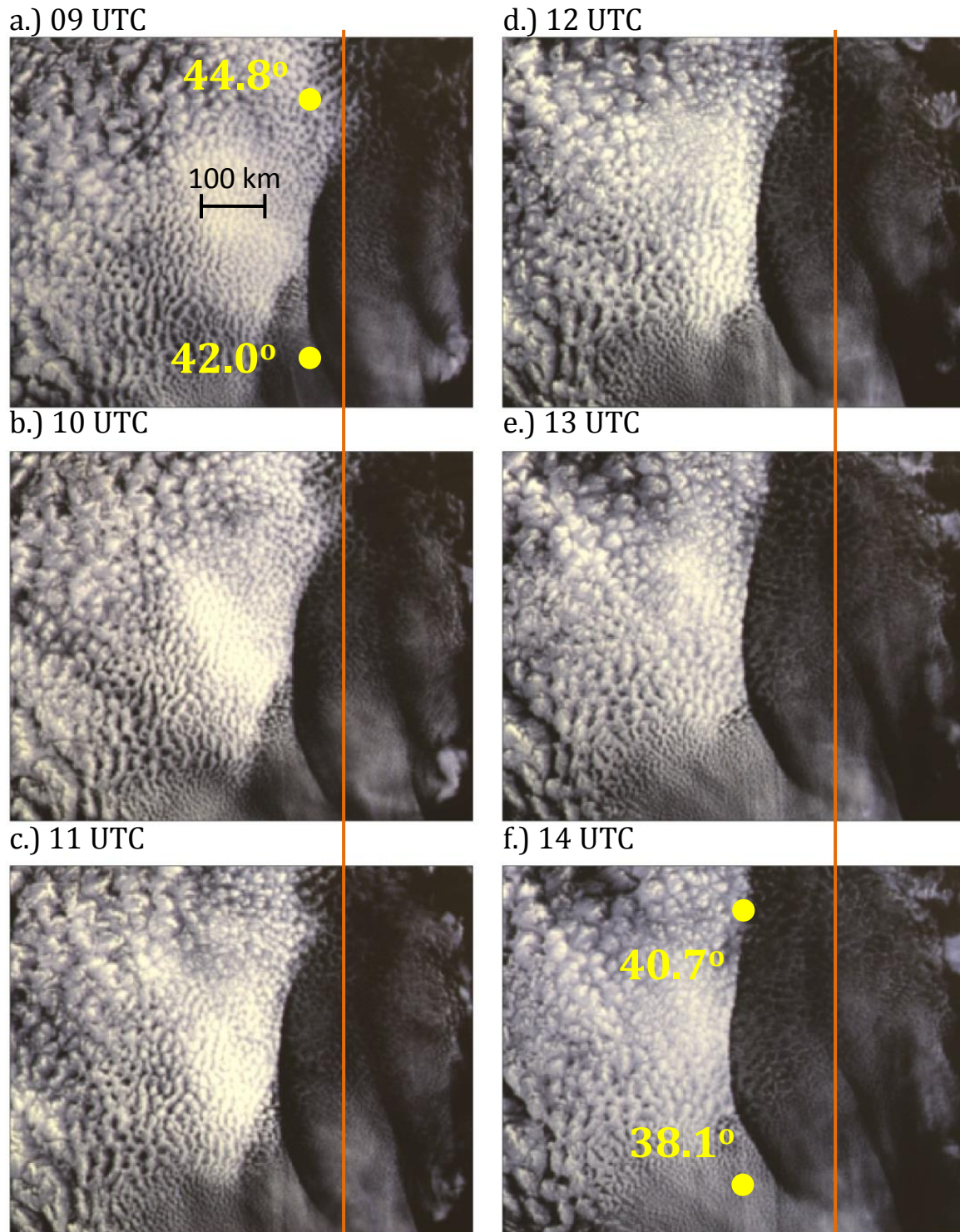
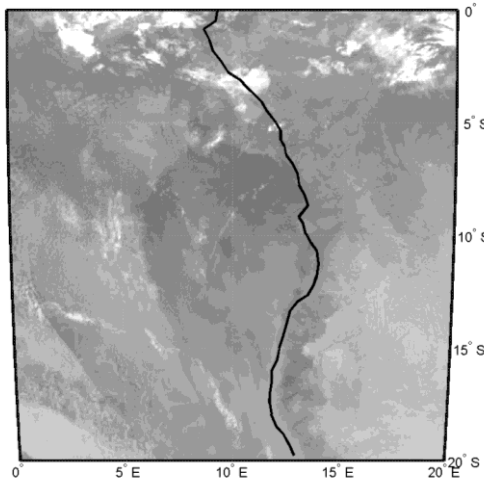
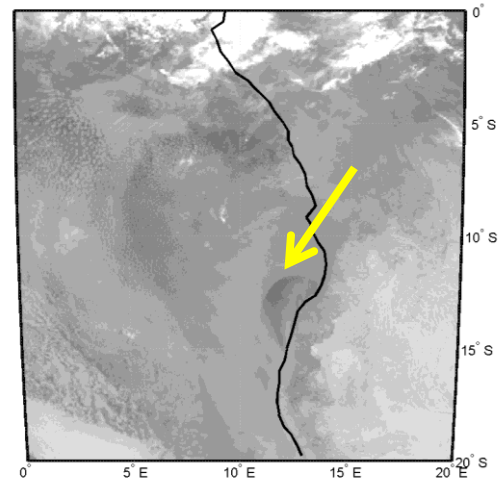


Figure 3.5: Close-up of Meteosat visible imagery of a sharp cloud boundary moving through the southeast Atlantic marine stratocumulus on 2012/05/26 (see Animation 3.9 for an animated loop of this boundary). The vertical orange line is located in the same relative location in each image to guide the eye in detecting the westward motion of the cloud boundary. The yellow dots denote the locations at which the solar elevation angles (values to the left of the dots) were calculated as discussed in Section 3.1.1. In panel a the dots are located at roughly  $-9^\circ$  and  $-13^\circ$  latitude,  $10^\circ$  longitude and the dots in panel f are roughly located at  $-9^\circ$  and  $-13^\circ$  latitude,  $9^\circ$  longitude.

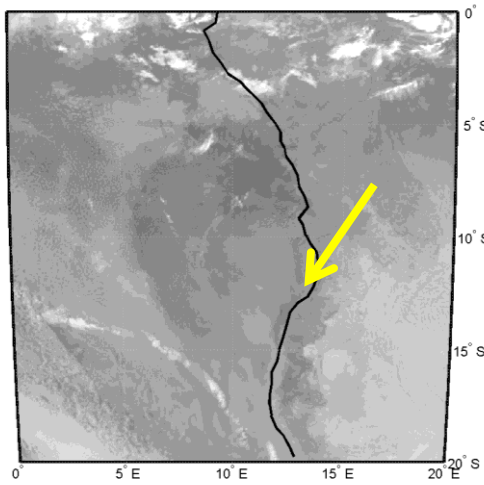
a.) 2000 UTC



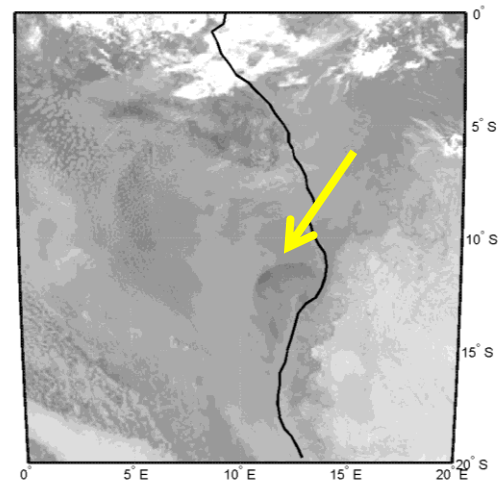
d.) 0200 UTC



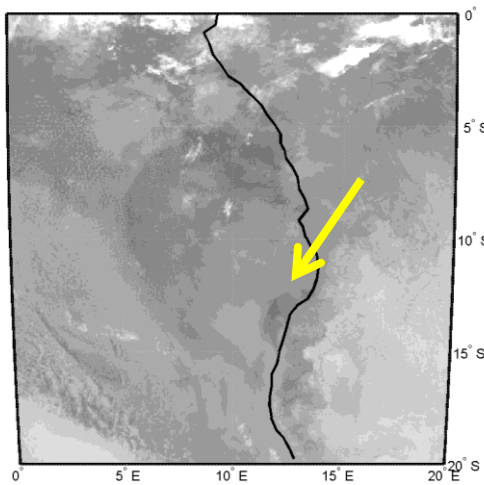
b.) 2200 UTC



e.) 0400 UTC



c.) 0000 UTC



f.) 0600 UTC

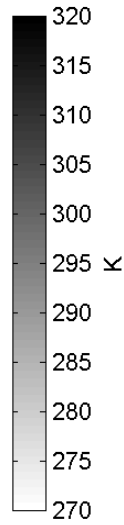
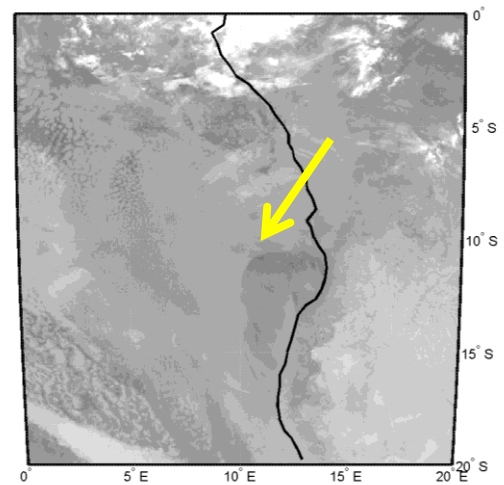


Figure 3.10: Example of a propagating sharp cloud boundary observed in merged infrared brightness temperature satellite imagery moving away from the southwest African coast around 0000 UTC between 03 June 2014 and 04 June 2014. A yellow arrow highlights the leading edge of the sharp cloud boundary in each frame.

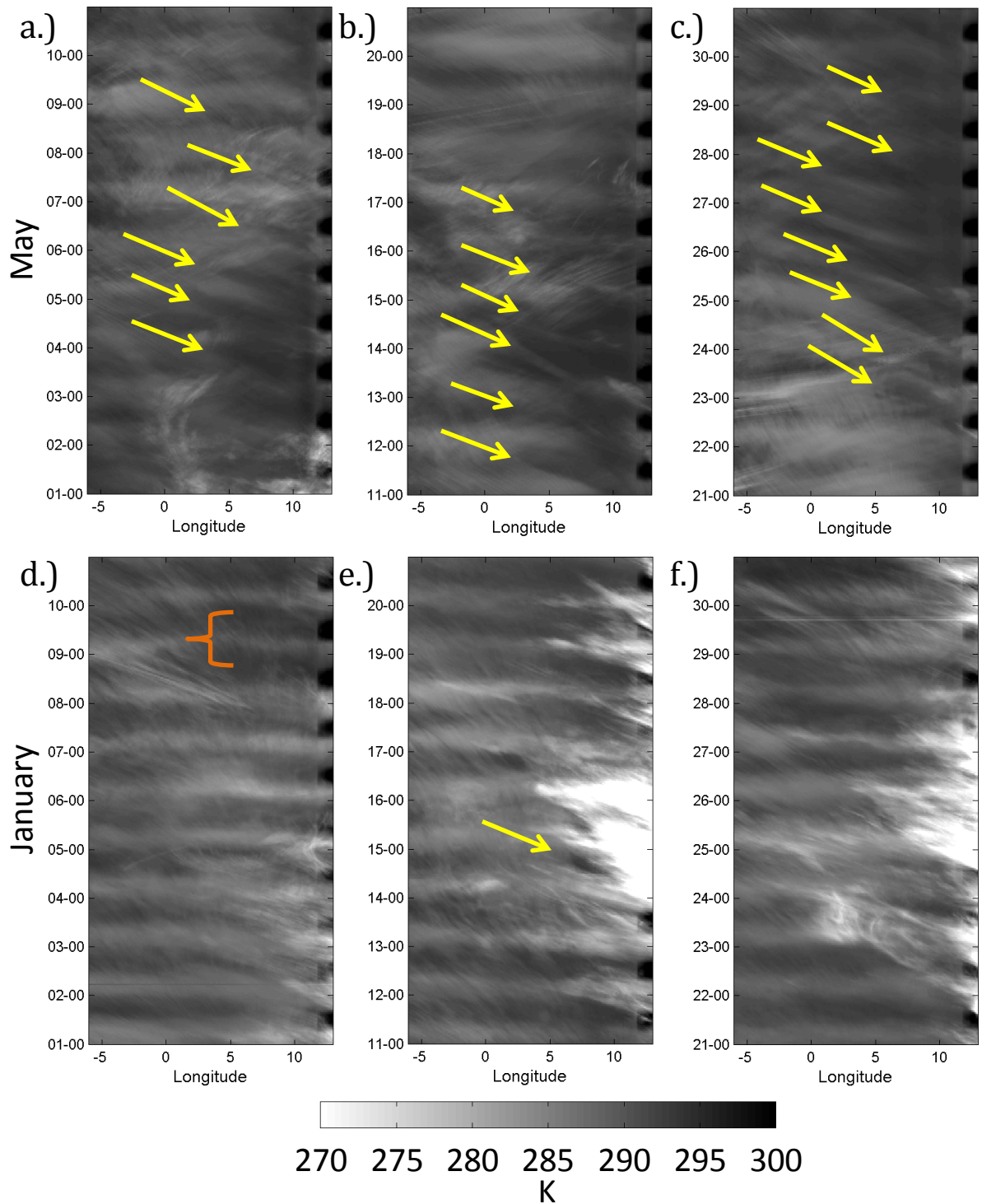


Figure 3.13: Merged infrared Hovmöller diagrams for the southeast Atlantic for (first row) May and (second row) January of 2014. The columns denote the separate thirds of each month. Refer to Figure 2.1 for a map showing the bounds of the analysis region. The labels on the time axis mark the day and hour (DD-HH UTC). Color bar is in Kelvin. Yellow arrows denote sharp cloudiness transitions (diagonally-oriented gradients in average brightness temperature) for all propagating cloud boundaries verified with MODIS Terra and Aqua image pairs. Orange bracket denotes one diurnal cycle in cloud fraction. Note that any missing data is ignored when taking the meridional average. 70

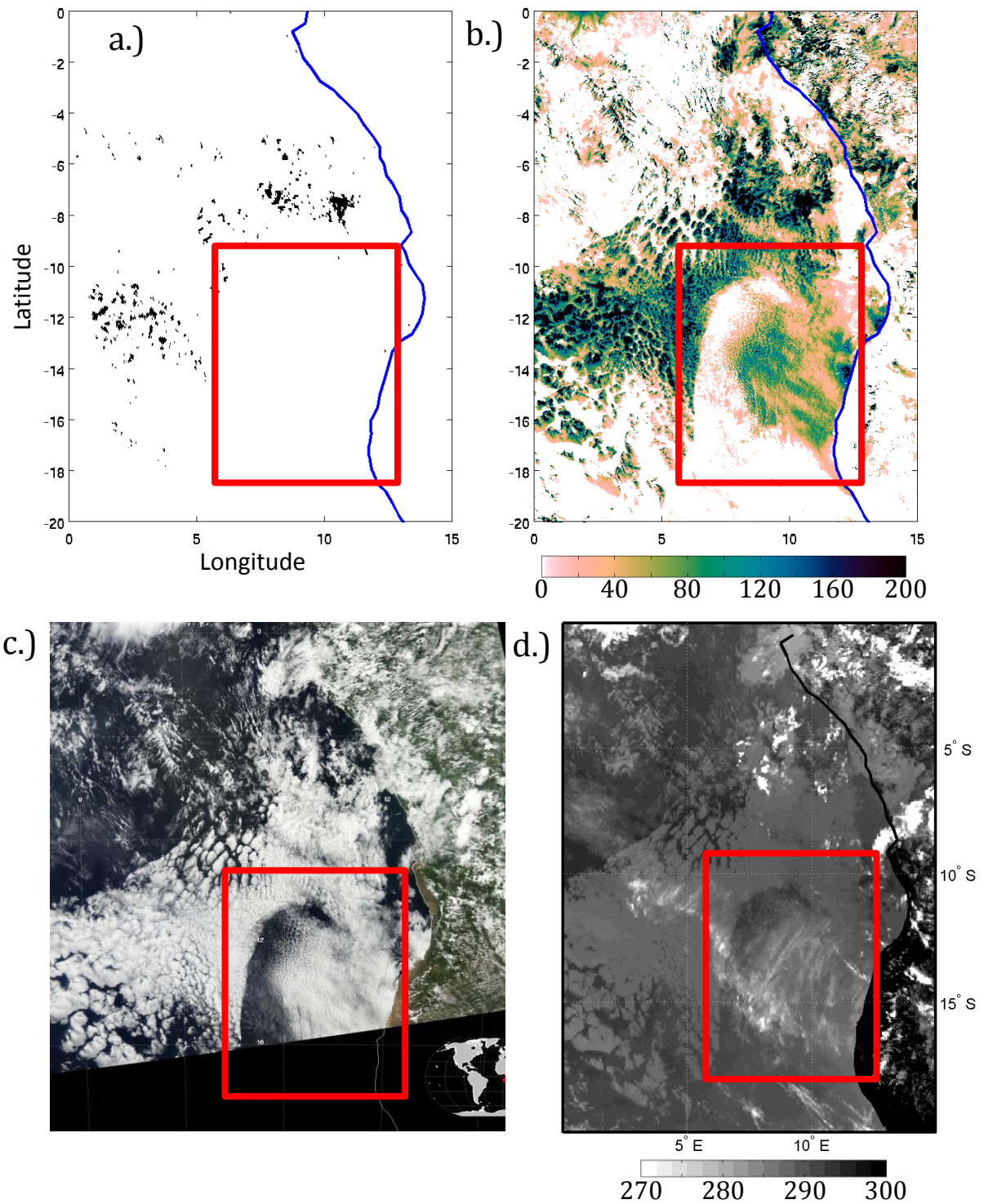


Figure 3.16: a.) Binary heavy drizzle detection of Miller and Yuter (2013) for the marine stratocumulus field in the southeast Atlantic for a westward-moving cloud boundary on 01 May, 2010 ~ 1300 UTC. Black denotes drizzle while white denotes no drizzle. b.) Liquid water path (LWP; in  $\text{gm}^{-2}$ ) values used to determine drizzle conditions in panel a. c.) True color visible image from the MODIS instrument (from [http://modis-atmos.gsfc.nasa.gov/IMAGES/index\\_L2Mosaics.html](http://modis-atmos.gsfc.nasa.gov/IMAGES/index_L2Mosaics.html)) on the Aqua satellite for approximately the same time as the heavy drizzle and LWP values. d.) Merged infrared brightness temperature (in K; see text) for roughly the same time as a-c. The red box is drawn in roughly the same geographical location in each panel. Panels a and b courtesy of Dr. Matthew Miller.

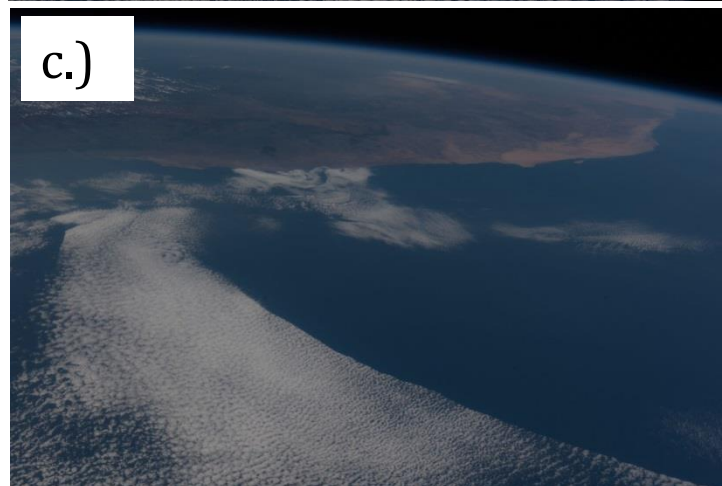
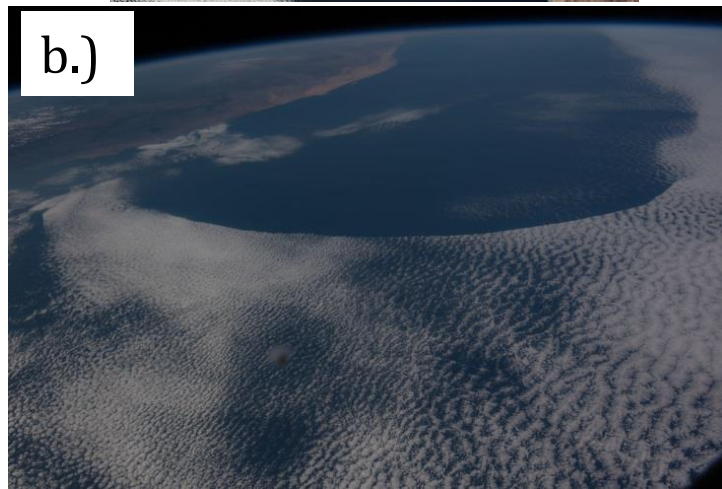
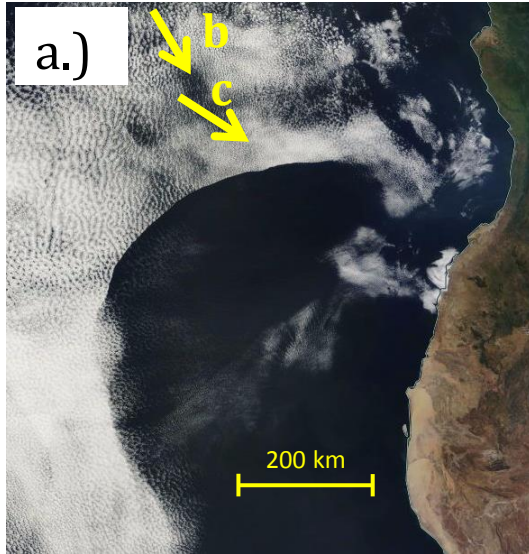


Figure 3.17. a.) Terra corrected reflectance image of a westward-moving cloud boundary on 21 May, 2016, at ~ 09:55 UTC. The approximate viewing angles of b and c are annotated with yellow arrows (note the time differences though). b.) Photograph of the westward-moving cloud boundary taken by an astronaut on the International Space Station, at roughly 08:52 UTC. c.) Same as in b but from a different angle relative to the cloud boundary. Panels b and c courtesy Earth Science and Remote Sensing Unit, NASA Johnson Space Center, see: <http://eol.jsc.nasa.gov/> .

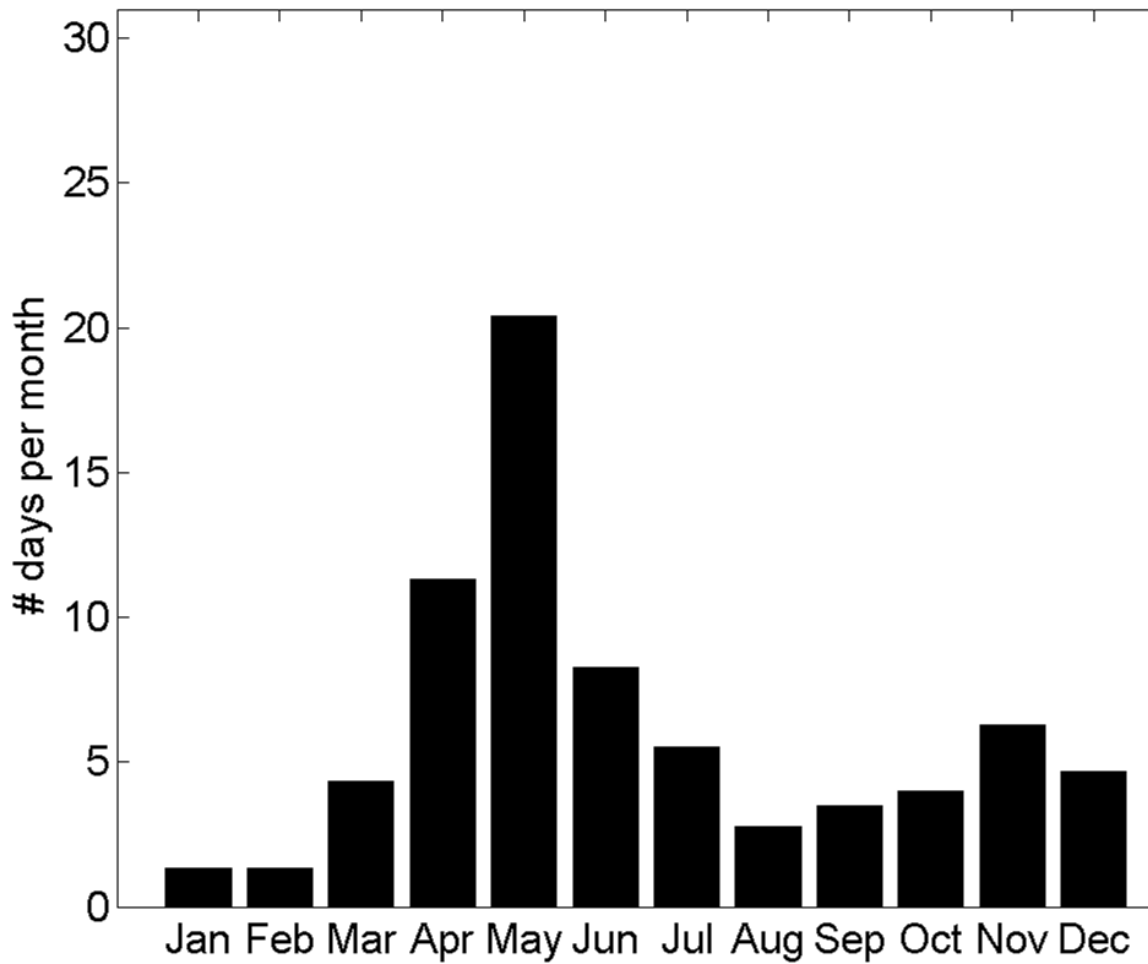


Figure 3.20: Histogram of the average number of days per month on which sharp cloud boundaries were identified in the southeast Atlantic for the period 08 May 2012 through 01 November 2015. See section 2.2 for details on the manual cloud boundary detection methodology.

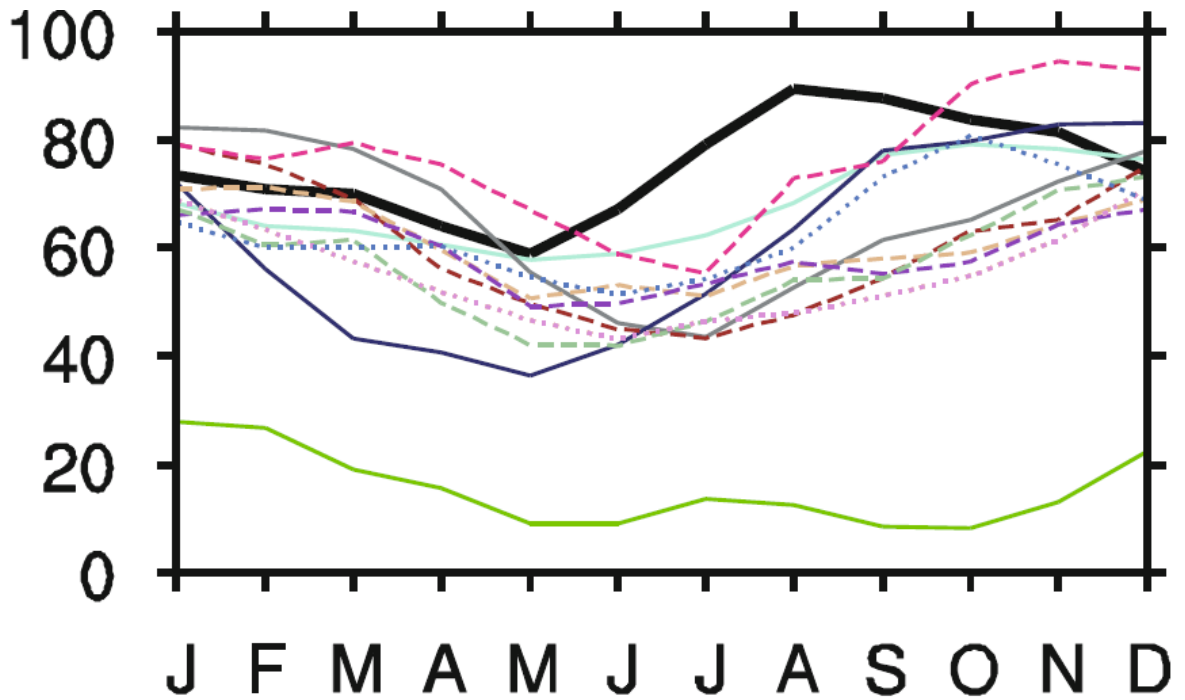


Figure 3.21: Figure 14 b of Zhang and Li (2013) showing the annual cycle of ISSCP-derived percent monthly total cloud fraction (solid black line) as well as various models (colored lines) for the region bounded by  $-10^{\circ}$  to  $-20^{\circ}$  degrees latitude and  $0^{\circ}$  to  $10^{\circ}$  longitude (see Figure 1.2 for a reference map of this analysis region).

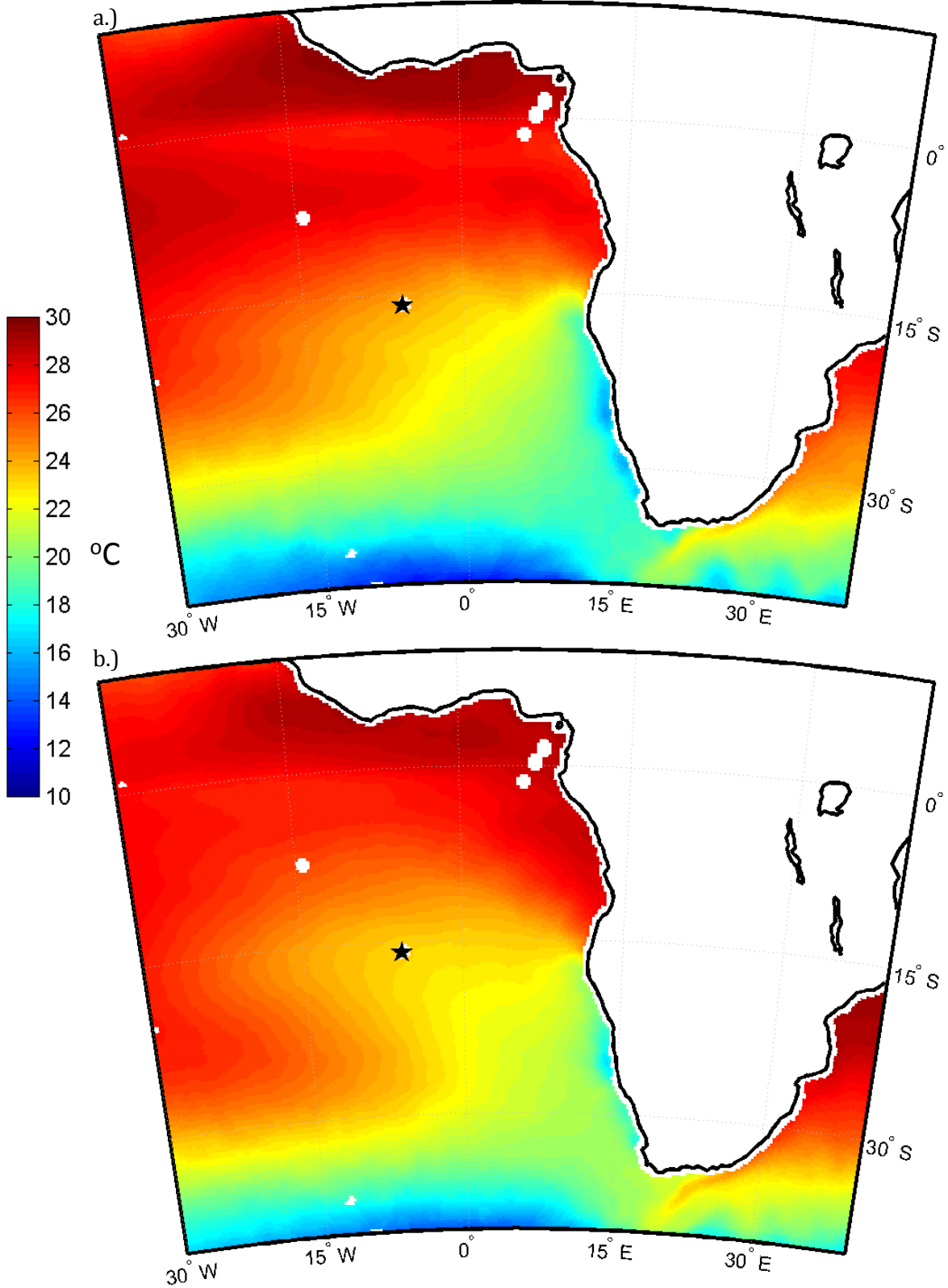


Figure 3.22: (a) May and (b) January average Remote Sensing System's optimally interpolated microwave sea surface temperatures for the years 2000 through 2011. The location of St. Helena Island is denoted by a black star. White denotes missing data.

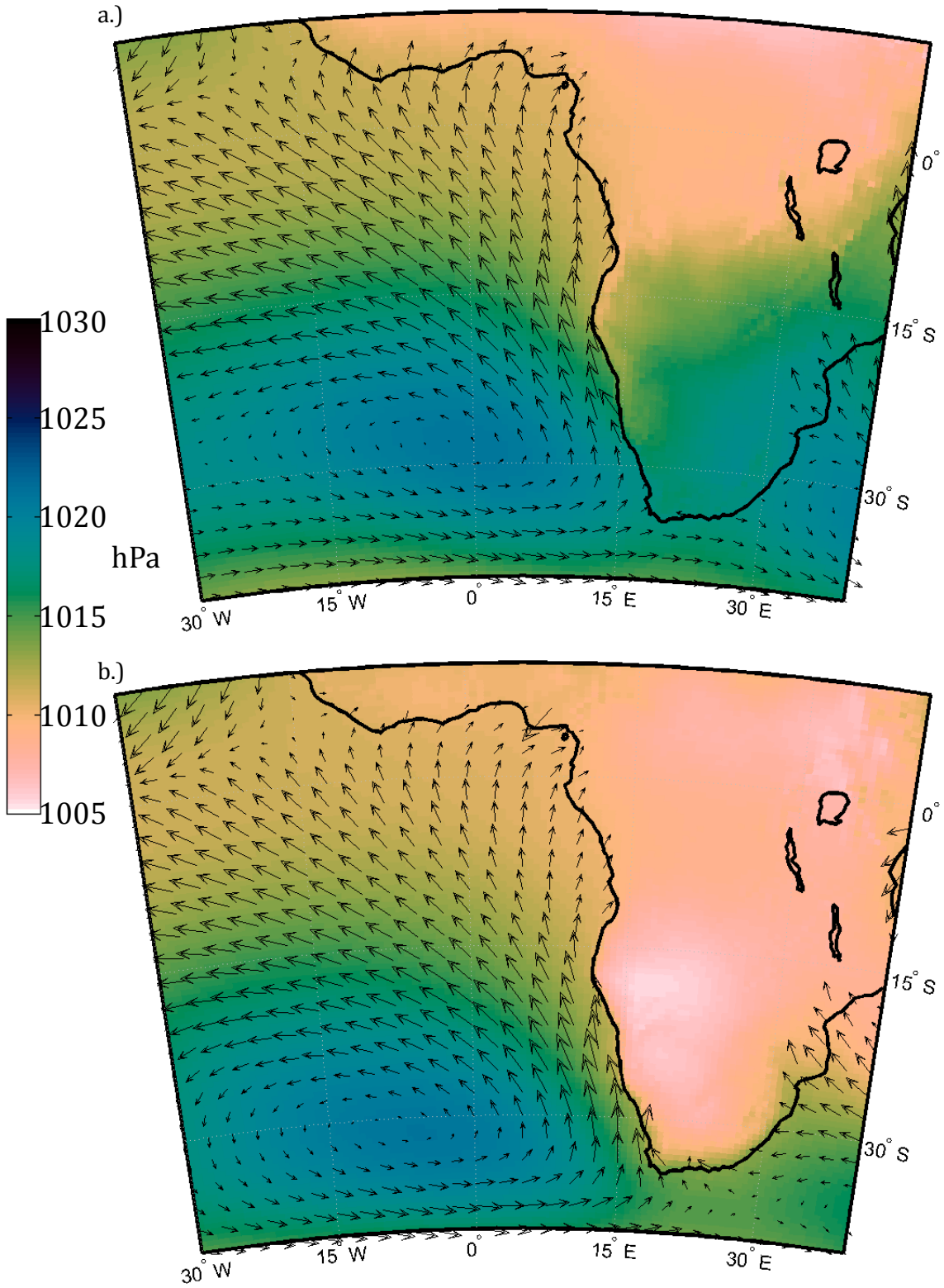


Figure 3.26: MERRA reanalysis mean sea level pressure (shading) and wind vectors (wind barbs) for the months of (a) May and (b) January for the period 01 January 2000 through 31 December 2015. 76

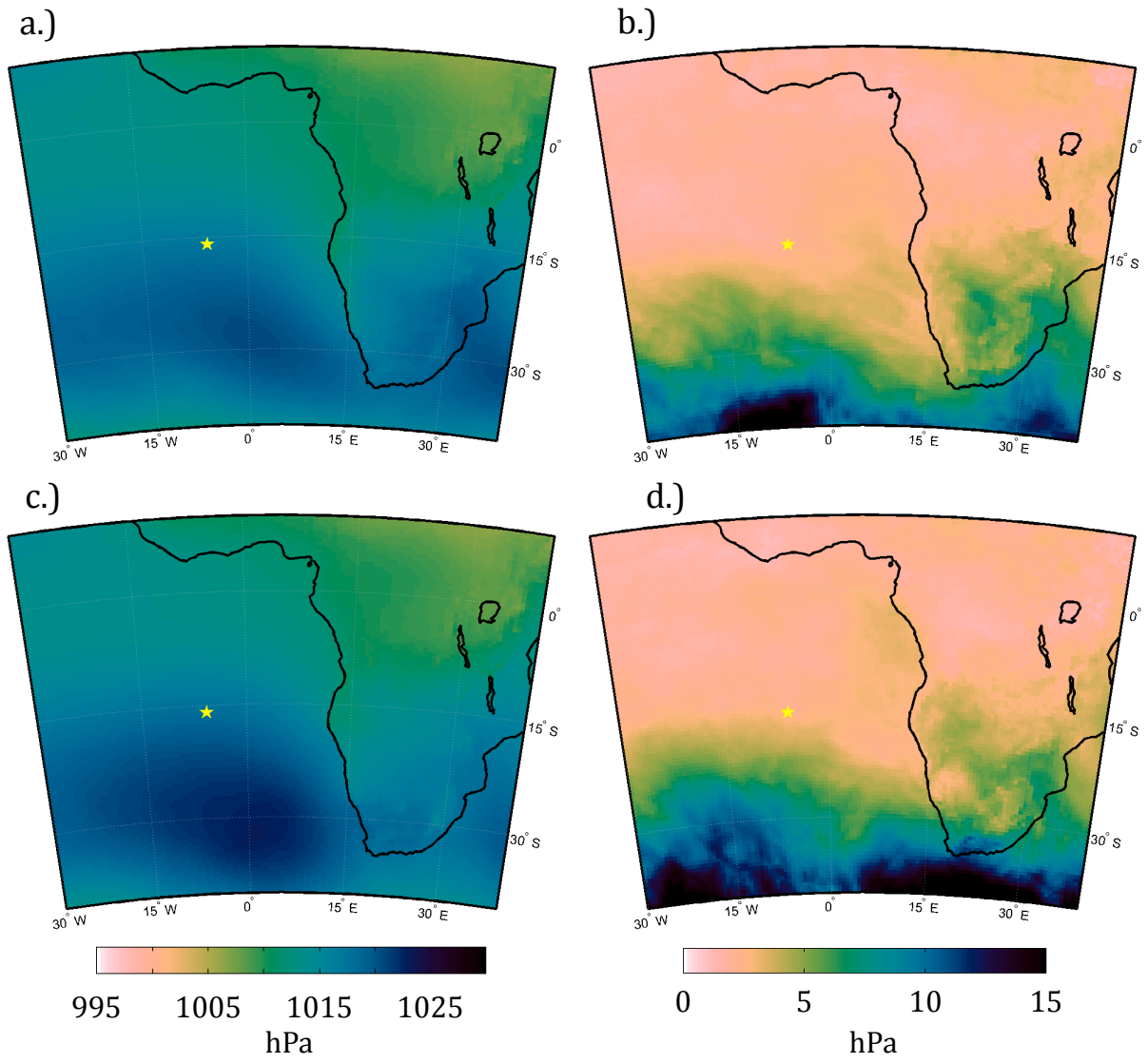


Figure 3.27: (a and c) Mean MERRA reanalysis sea level pressure and (b and d) inner quartile range of MERRA reanalysis sea level pressure at 00 UTC for the period April-June 2013 composited for days on which westward-moving cloud boundaries (a and b) were and (c and d) were not identified in the Terra and Aqua MODIS corrected reflectance images. The location of St. Helena Island is denoted by a yellow star.

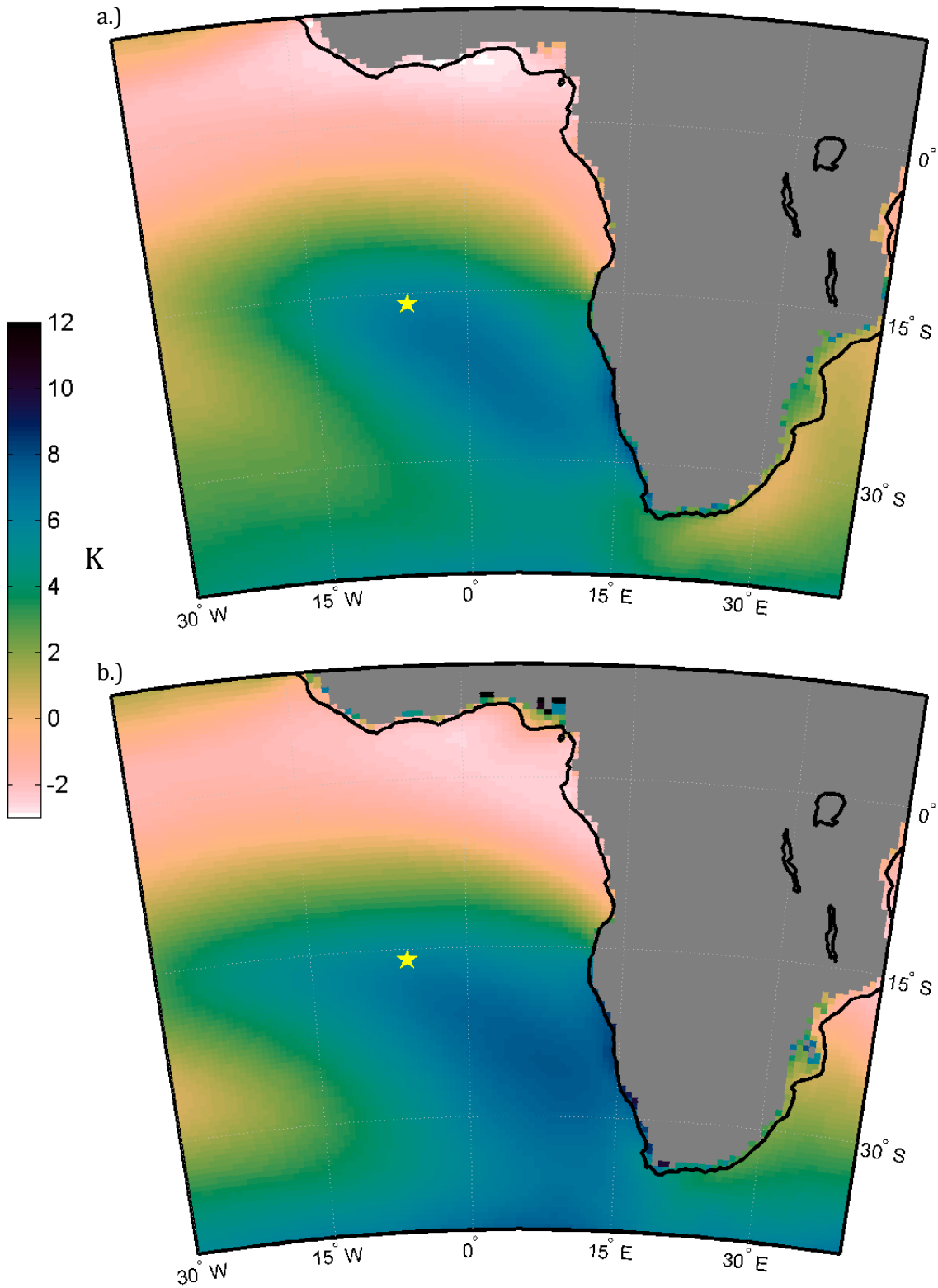


Figure 3.28: MERRA reanalysis mean estimated inversion strength (Wood and Bretherton, 2006) for the months of (a) May and (b) January for the period 01 January 2000 through 31 December 2015. Gray denotes missing data. The location of St. Helena Island is denoted by a yellow star.

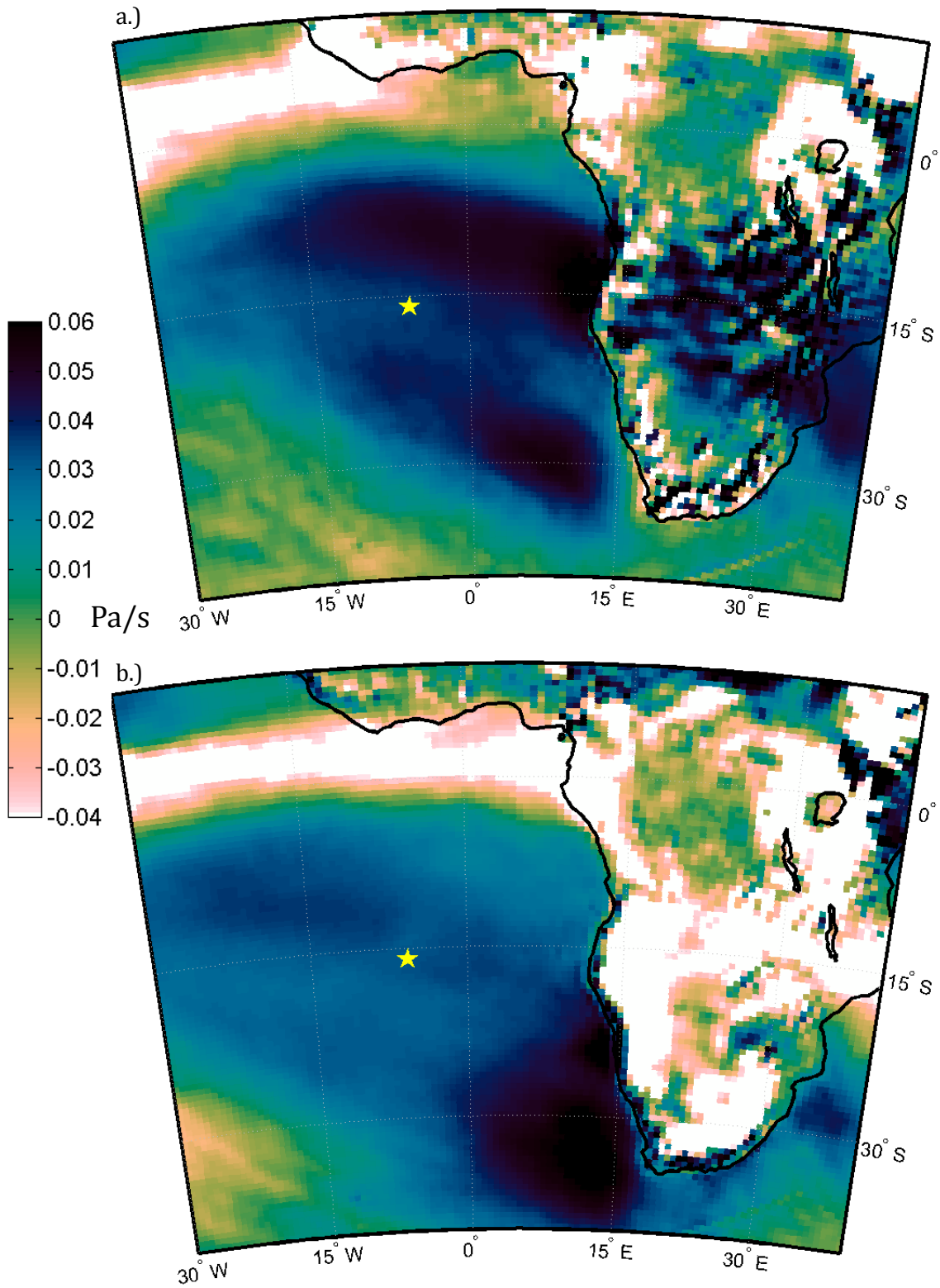


Figure 3.29: MERRA reanalysis mean pressure vertical velocity at 700 hPa for the months of (a) May and (b) January for the period 01 January 2000 through 31 December 2015. The location of St. Helena Island is denoted by a yellow star.

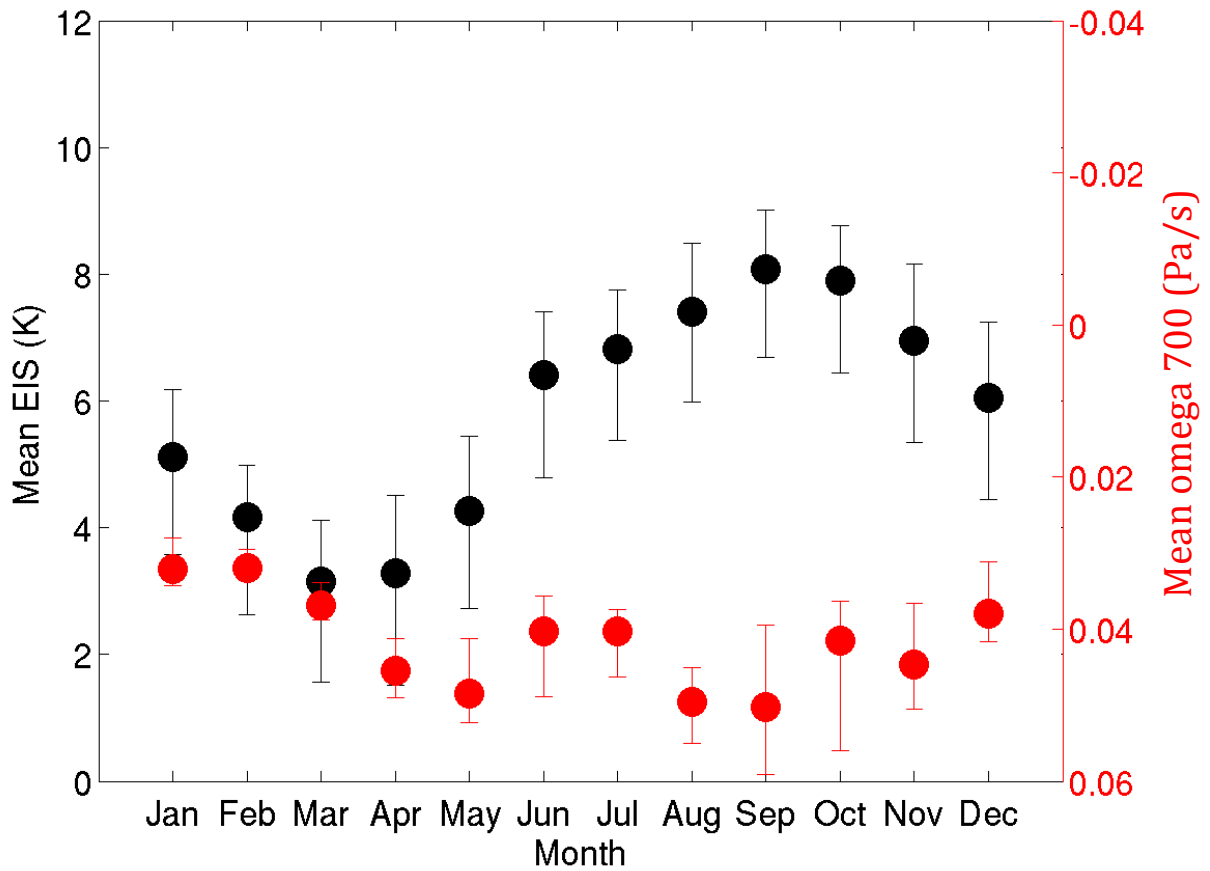


Figure 3.30: Median and inner quartile range of the monthly-averaged estimated inversion strength (EIS; black dots) and 700 hPa pressure vertical velocity (omega; red dots) derived from MERRA reanalysis data from 2000 through 2015 for the area bounded by 0° to 10° longitude, -20° to -10° latitude.

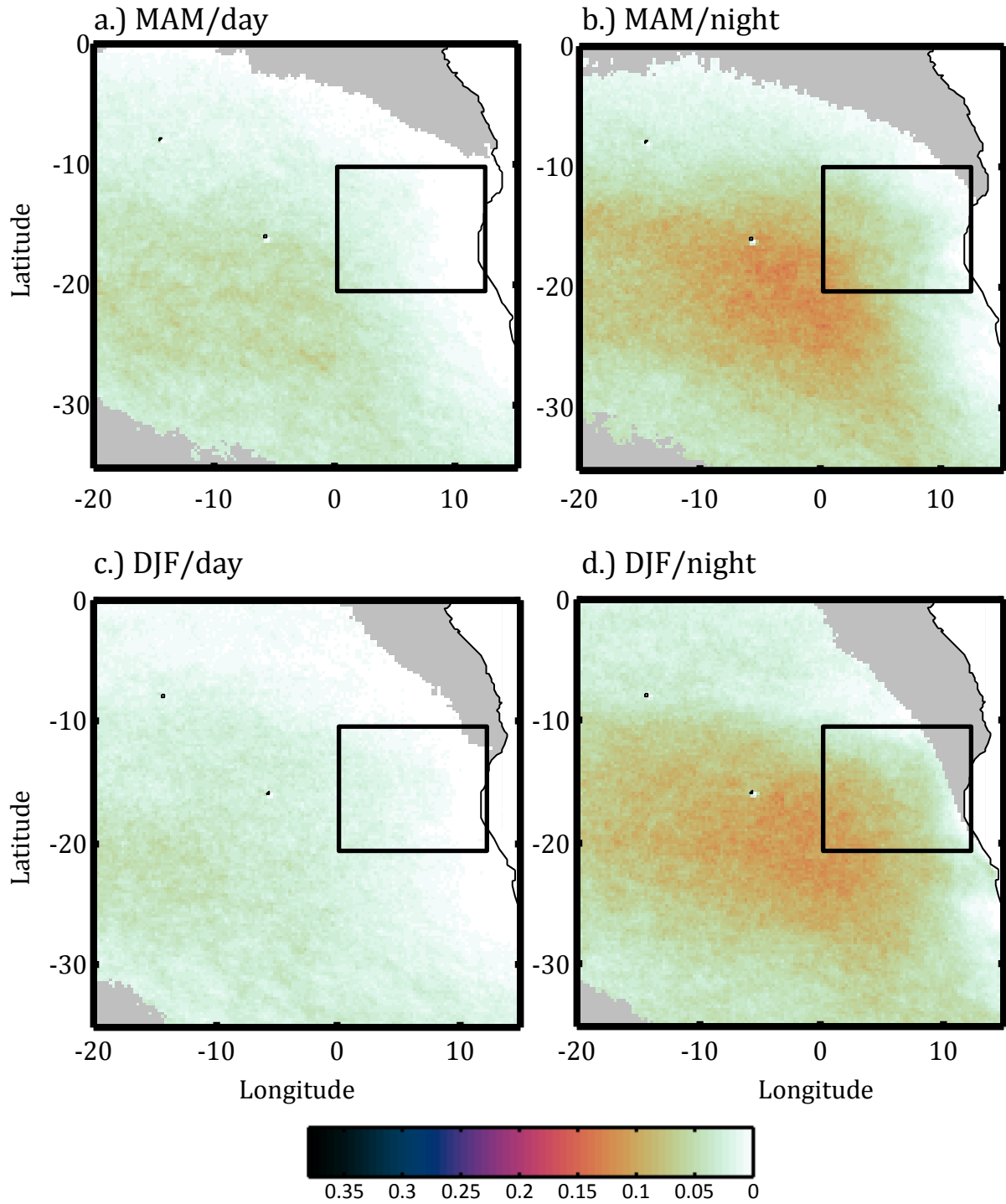
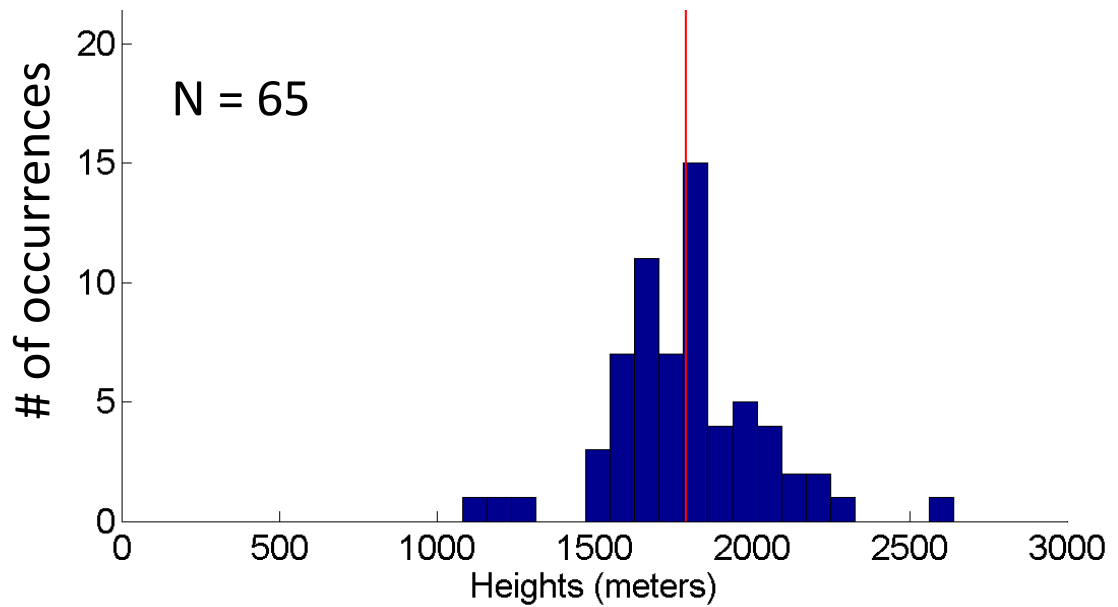


Figure 3.31: Seasonally averaged frequency of heavy drizzle in the southeast Atlantic ocean from September 2002 to December 2011 for (top row) March/April/May, (bottom row) December/January/February, (first column) daytime, and (second column) nighttime. Drizzle frequency is based on the 89-GHz detection method of Miller and Yuter (2013). Black boxes in each panel denote the approximate region of the cloud boundary climatology discussed in section 2.2. Figure is from Miller et al. (2016). Images courtesy Matthew A. Miller.

a.) May



b.) January

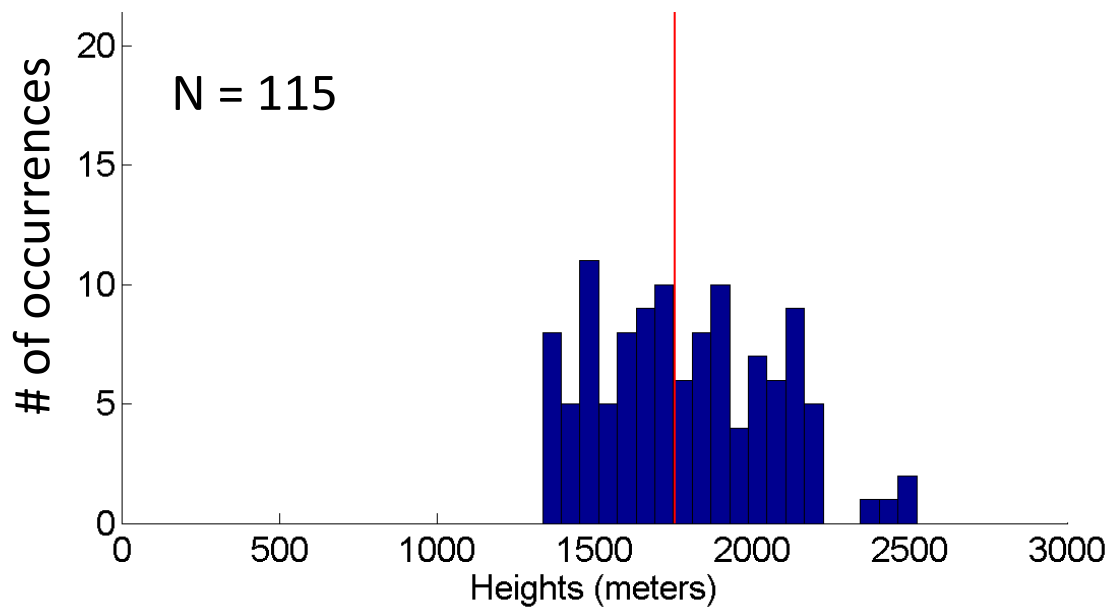
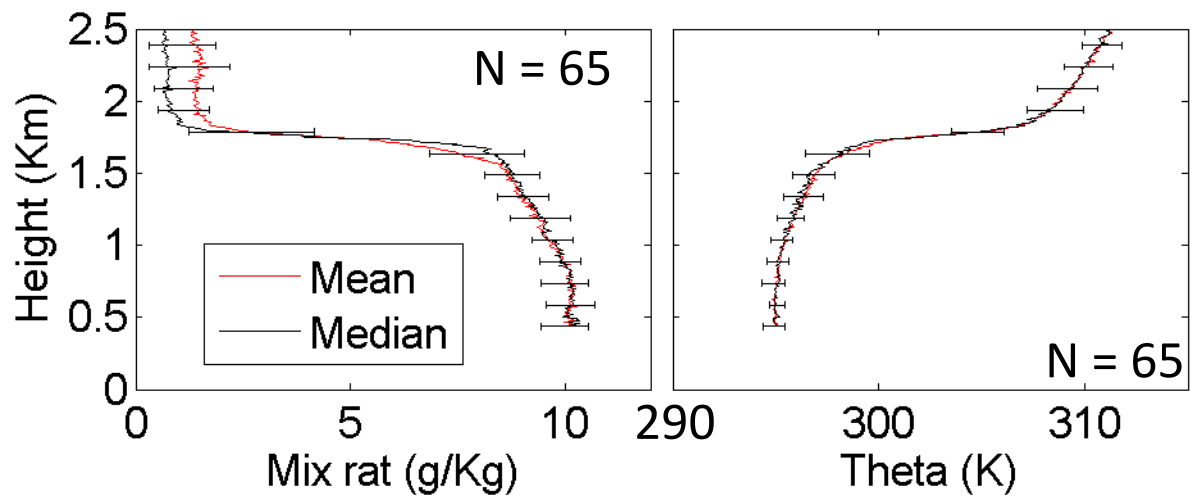


Figure 3.32: Histograms of inversion heights of 'representative' soundings from St. Helena Island (see section 2.4 for details) for the months of (a) May and (b) January for the years 2000 through 2011 that were found to have a 'strong' inversion. The vertical red line denotes the median inversion height for the month. The number in each panel denotes the number of soundings used in the calculations.

a.) May



b.) January

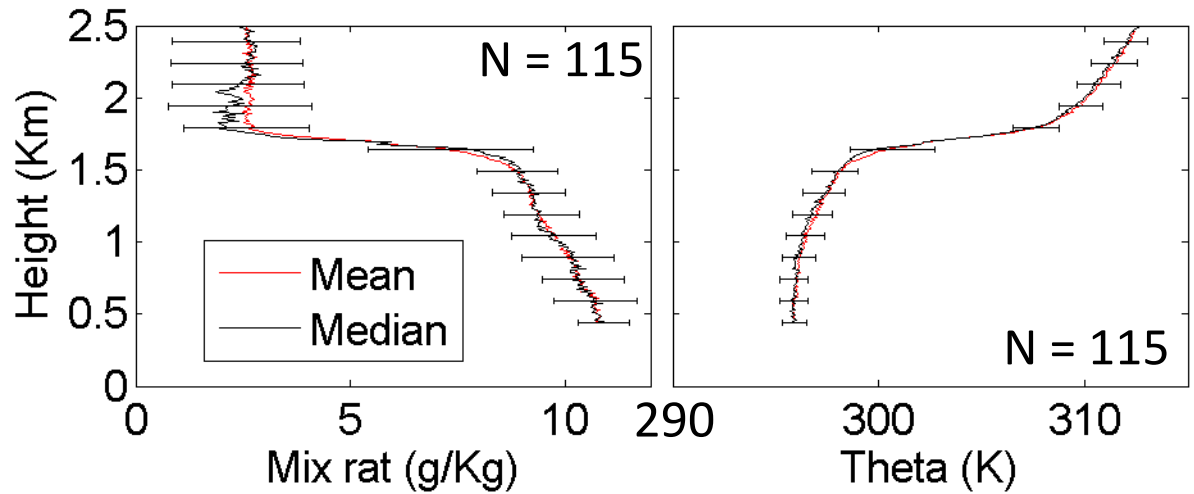


Figure 3.33: Mean, median, and inner/outer quartile values of mixing ratio and potential temperature obtained from 'representative' soundings from St. Helena Island with a 'strong' inversion (see section 2.4 for details) for the months of (a) May and (b) January. The values were calculated for the years 2000 through 2011. The number in each panel denotes the number of soundings used in the calculations.

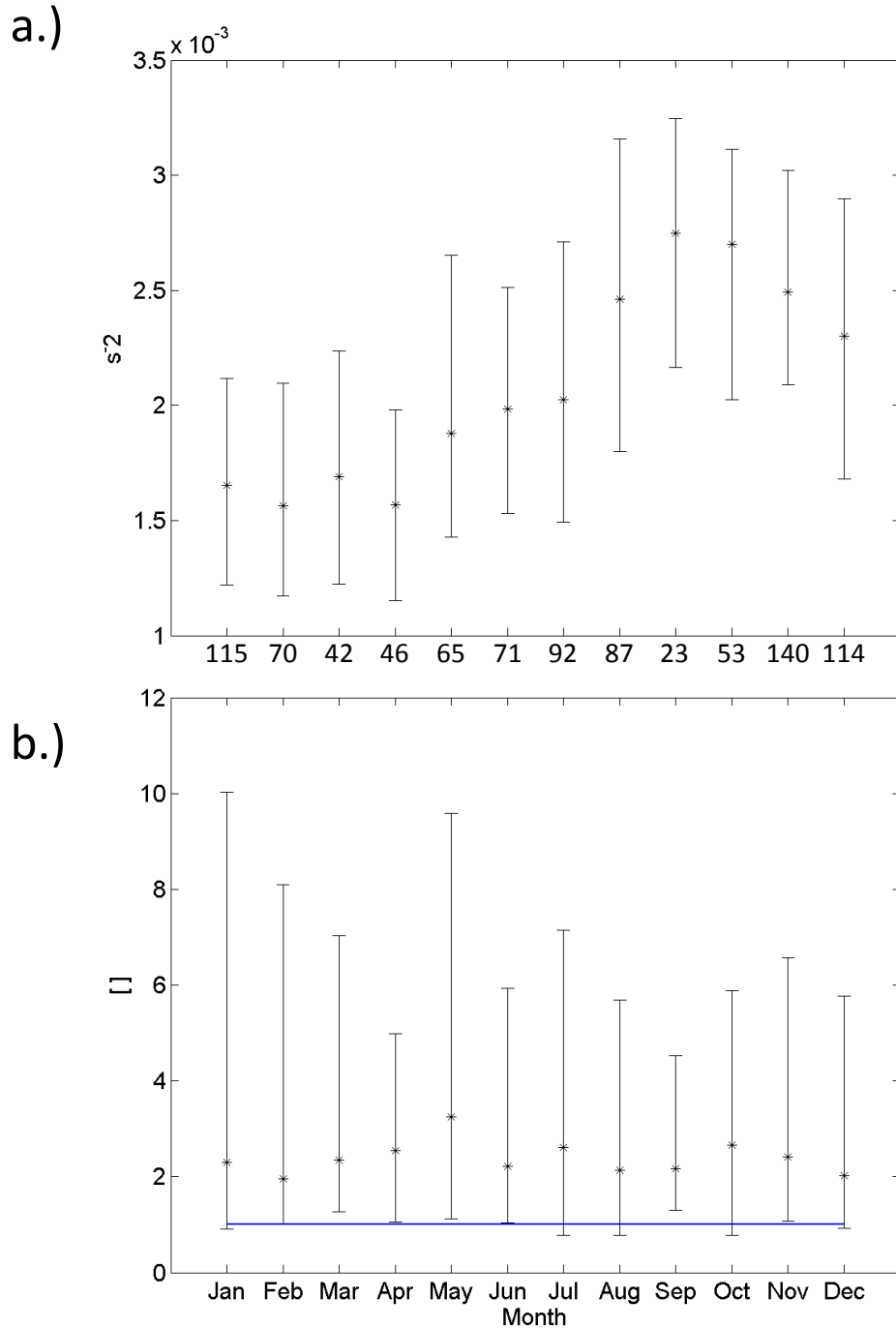


Figure 3.34: Monthly median and inner/outer quartiles of (a) square of the Brunt Väisälä frequency and (b) Richardson number calculated from St. Helena soundings for the period 01 January 2000 through 31 December 2011. Only soundings that were determined to be ‘representative’ of the adjacent marine stratocumulus region and exhibited a ‘strong’ inversion were used in this analysis (see Section 2.4). A blue reference line showing a Richardson number of one is provided in panel b). The number of soundings used for calculation of both parameters is shown in between the panels (note that in March, the number of Richardson numbers was 41).

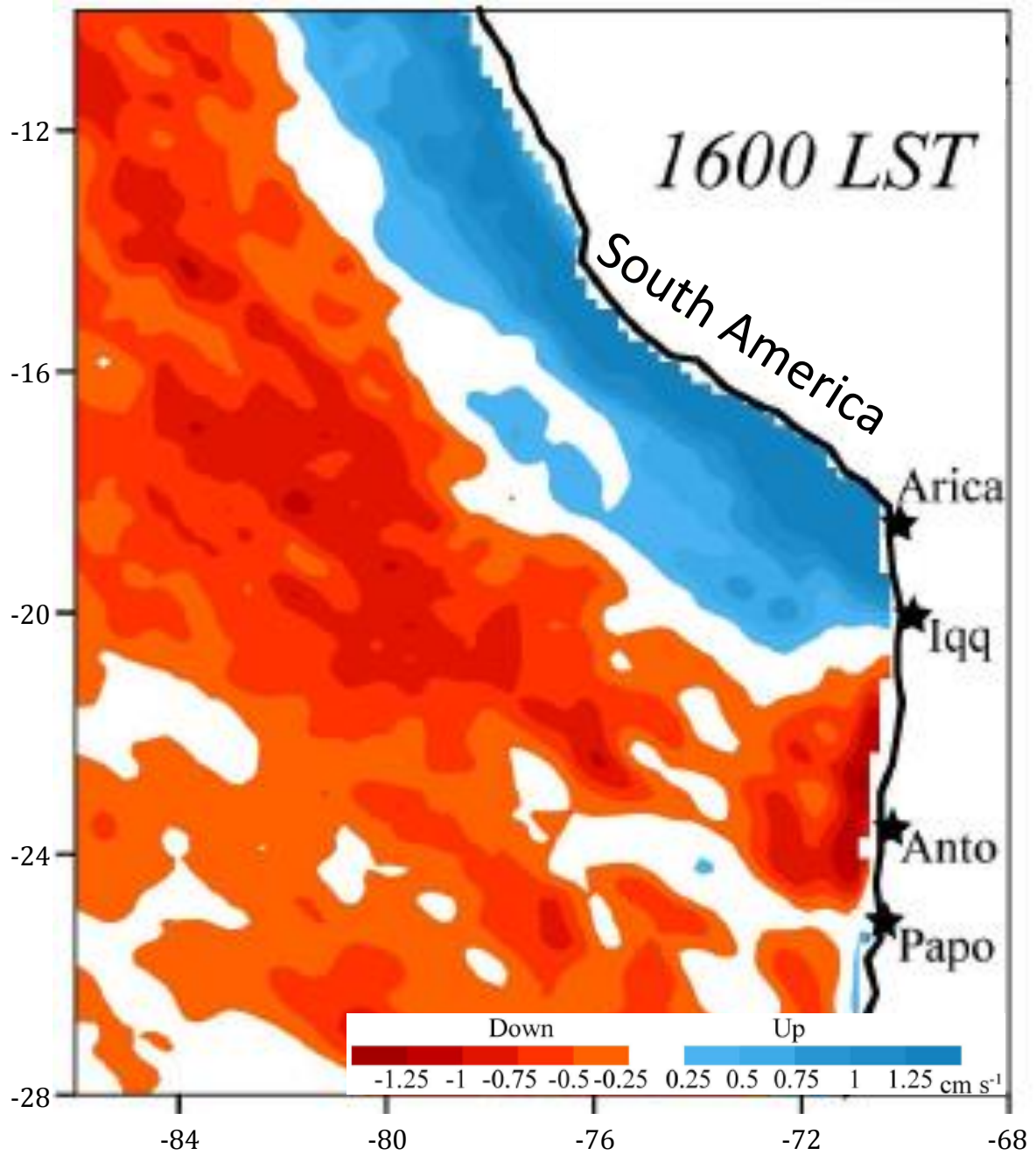


Figure 4.1: From Figure 9 of Rahn and Garreaud, 2010 showing the WRF modeled vertical velocity anomalies associated with the ‘upsidence’ wave for a 2 month period at 2.5 km over the southeast Pacific. Warm colors denote downward motion, while cool colors denote upward motion.

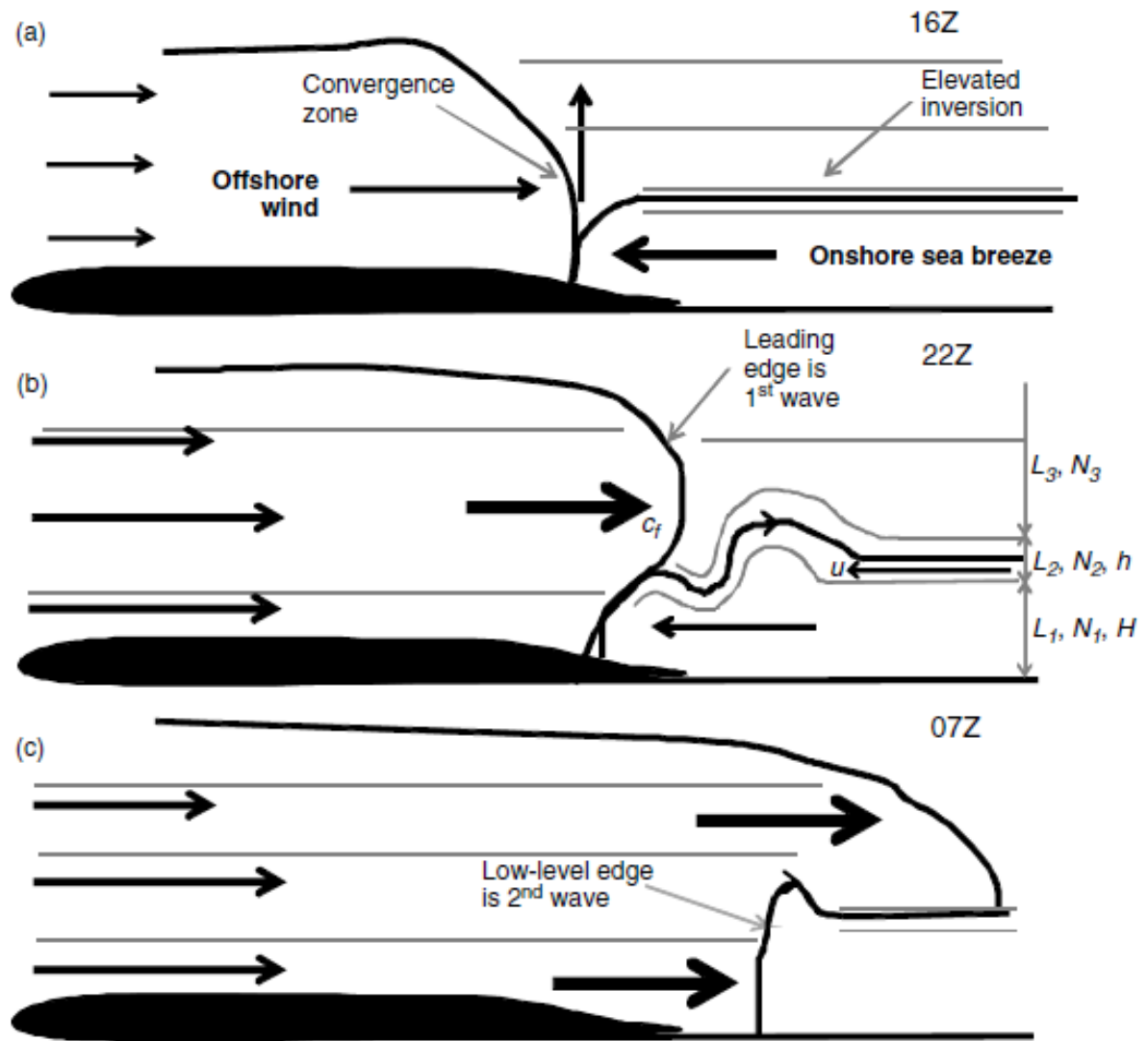


Figure 4.2: Figure 13 of Birch and Reeder, 2013. This diagram depicts the mechanism by which cloud-generating waves are formed along the northwest coast of Australia. Perturbations caused by the confluence of the onshore sea breeze and strong offshore flow generate waves at two different times that propagate along an elevated inversion over the ocean.

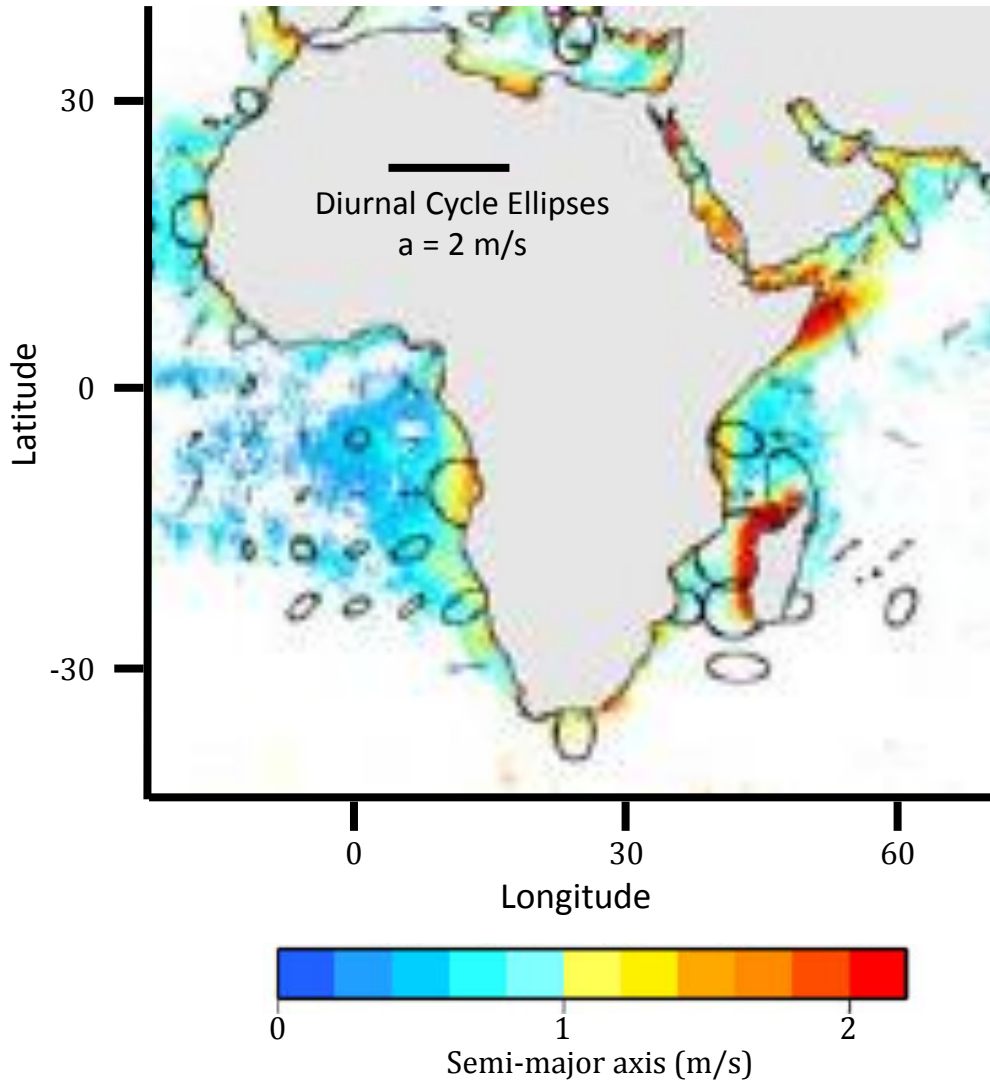


Figure 4.3: From Figure 1 panel a of Gille et al. 2005 depicting the strength of the diurnal cycle in the near-surface wind around Africa. Shading shows (where it is statistically significant) the length of the semi-major axis of elliptical hodographs generated from a least squares fit of the four-times daily wind components (binned into  $.25^\circ$  latitude by  $.25^\circ$  longitude boxes) from QuickScat and ADEOS-II SeaWinds scatterometer data from April-October, 2003. Reference ellipses are plotted every  $6^\circ$  within  $10^\circ$  of land or equatorward of  $30^\circ$ , and a reference semi-major axis length is provided in the figure.

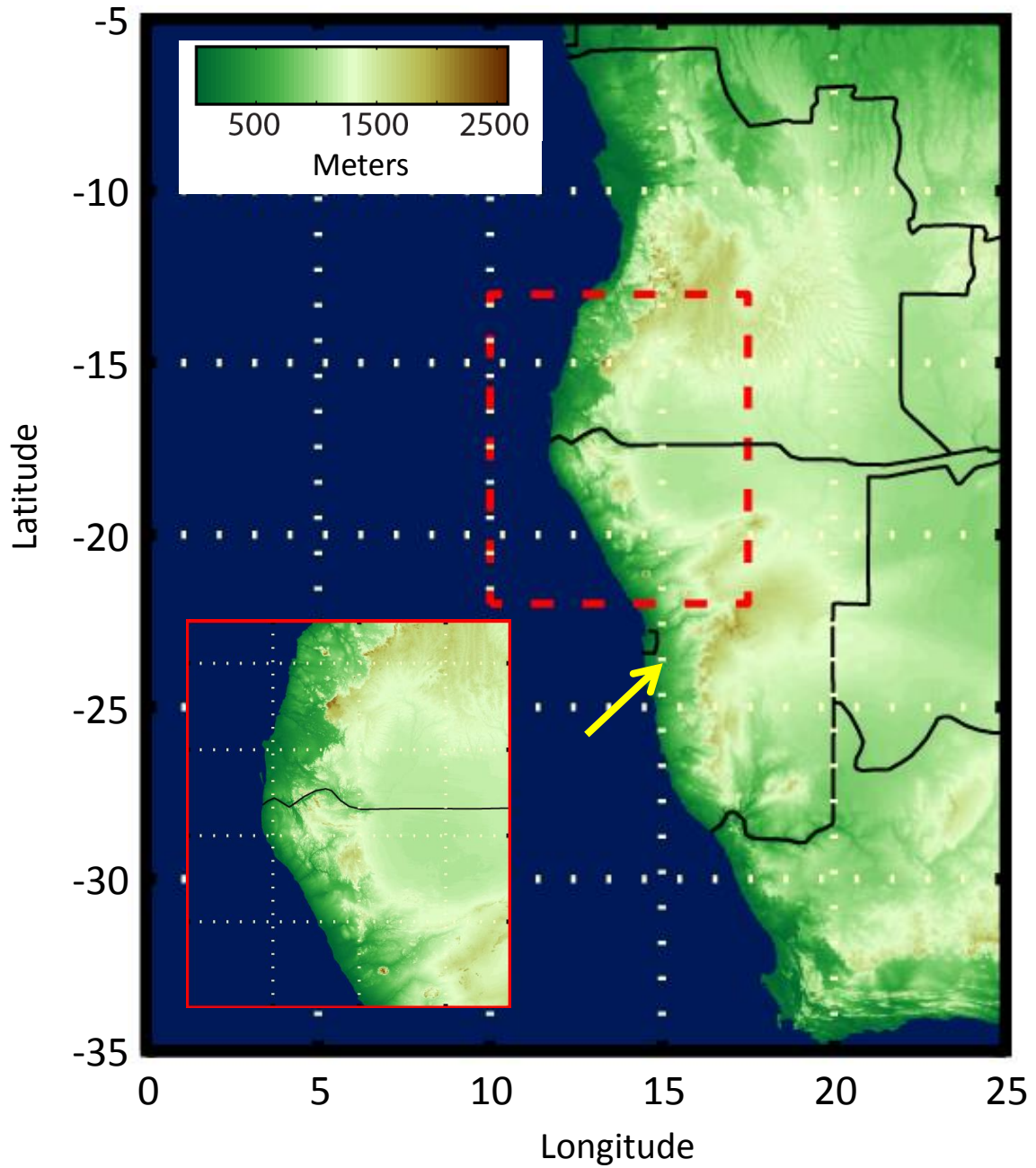
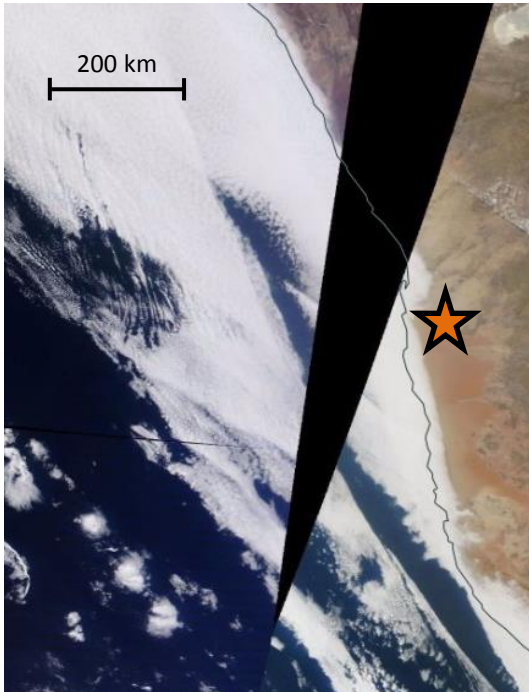
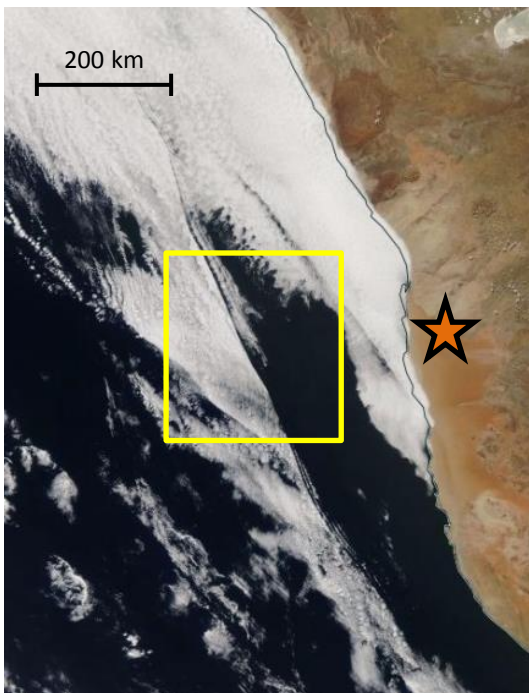


Figure 4.4: Gtopo30 30 arc-second elevation of (wide-view) the southwestern African coast and (inset) the coastal region near the Angola/Namibia border. The approximate location of Gobabeb, Namibia is denoted by an arrow. Data from the United States Geological Survey, figure courtesy of Dr. Matthew A. Miller.

a.) Terra 10:10 (left swath, 08:35 right)



b.) Aqua 12:55



c.) Aqua close-up

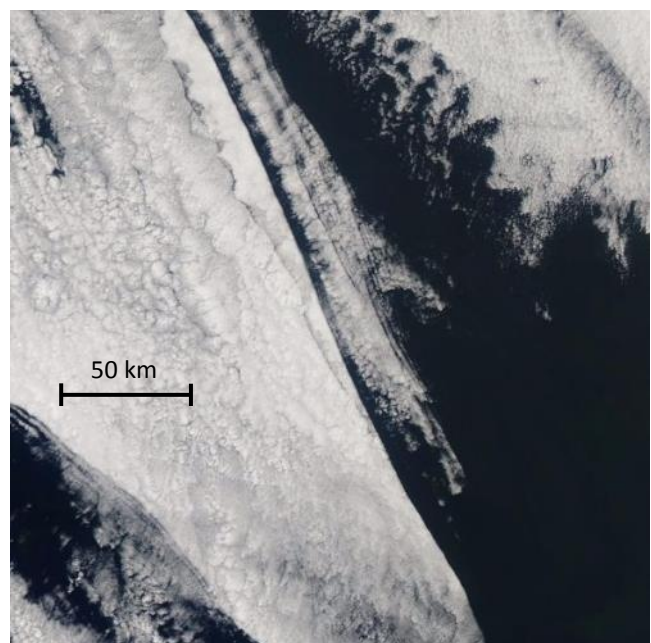


Figure 4.5: Corrected reflectance images from 02 August 2014 from the (a) Terra and (b) Aqua satellite showing an instance of a propagating sharp cloud boundary in the vicinity of Gobabeb, Namibia, the site of high temporal resolution surface meteorological observations. A close-up of the sharp cloud boundary (yellow box in panel b) is shown in panel c. The approximate location of Gobabeb, Namibia is denoted by a star in panels a and b.

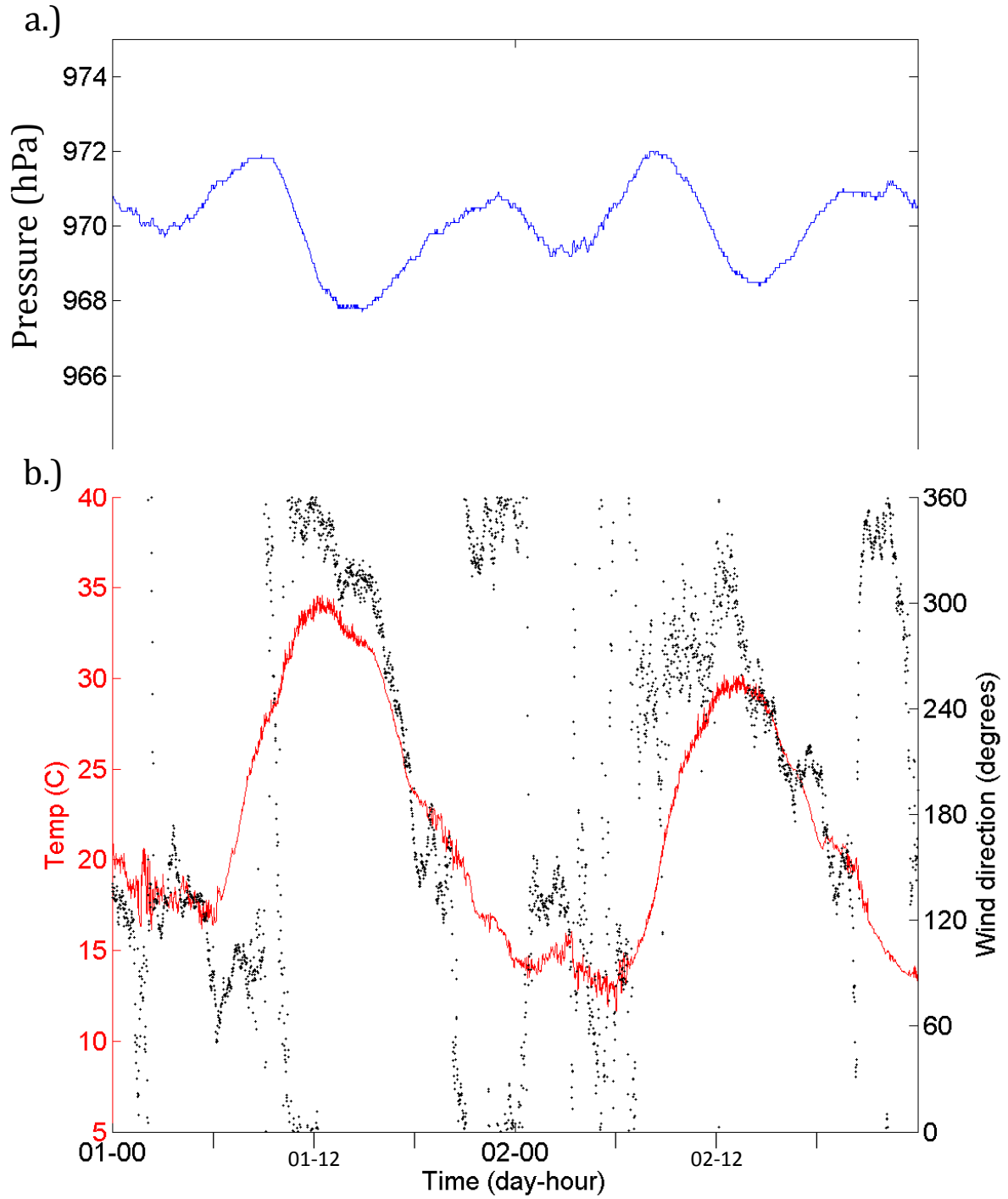


Figure 4.7: Panel a: 1.5 meter surface pressure at Gobabeb, Namibia. Panel b: 24 meter wind direction (black) and temperature (red) from Gobabeb. Variables shown are for 01 August 2014 through 02 August, 2014. Time is in UTC (i.e. 1 hour behind local time). Note that the pressure and temperature/winds are collected at sites ~ 1.5 kilometers apart.

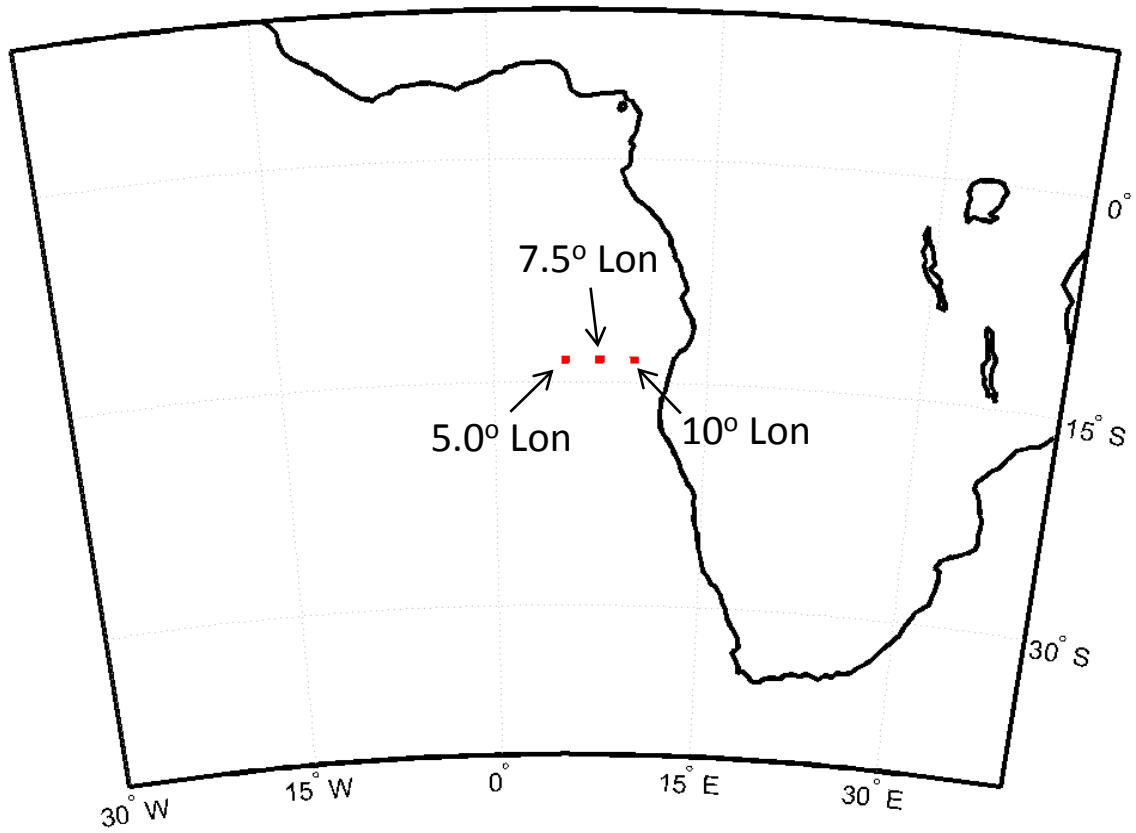


Figure 4.8: Reference map for the three point locations at which the angular difference between the MERRA reanalysis wind field and the reference wind direction of due east ( $90^\circ$ ) is calculated (Figure 4.9).

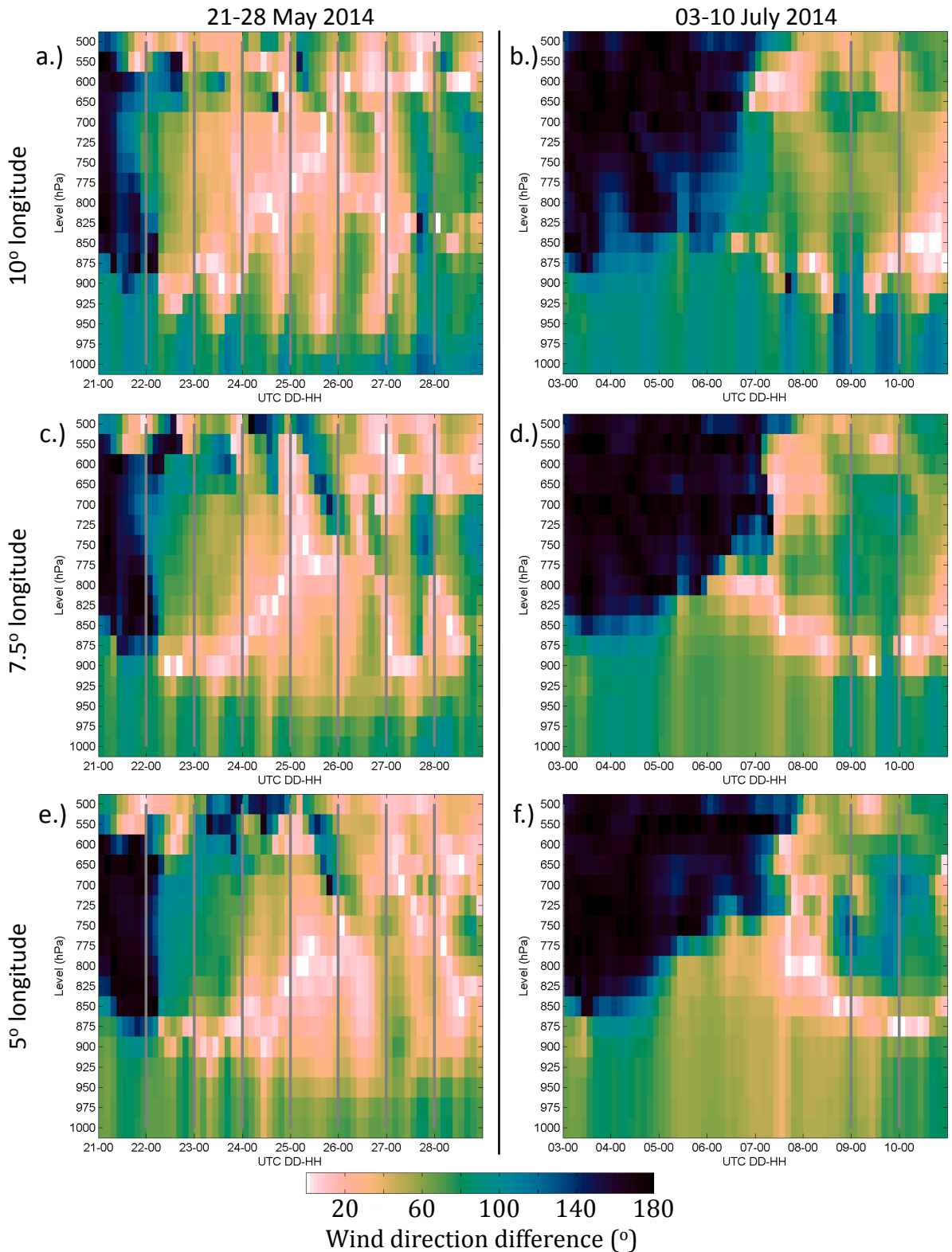


Figure 4.9: Angular difference in the MERRA reanalysis wind direction from due east for (a,c,e) 21-28 May, 2014 and (b,d,f) 03-10 July, 2014 at  $-13.5^\circ$  Lat (a,b)  $10.0^\circ$  Lon, (c,d)  $7.5^\circ$  Lon, and (e,f)  $5.0^\circ$  Lon. See Figure 4.8 for a reference map of these locations. Vertical gray lines denote the start of days on which westward-moving cloud boundaries were identified in the Aqua and Terra corrected reflectance images. Note that the cloud boundaries do not necessarily always extend to  $5^\circ$  longitude.

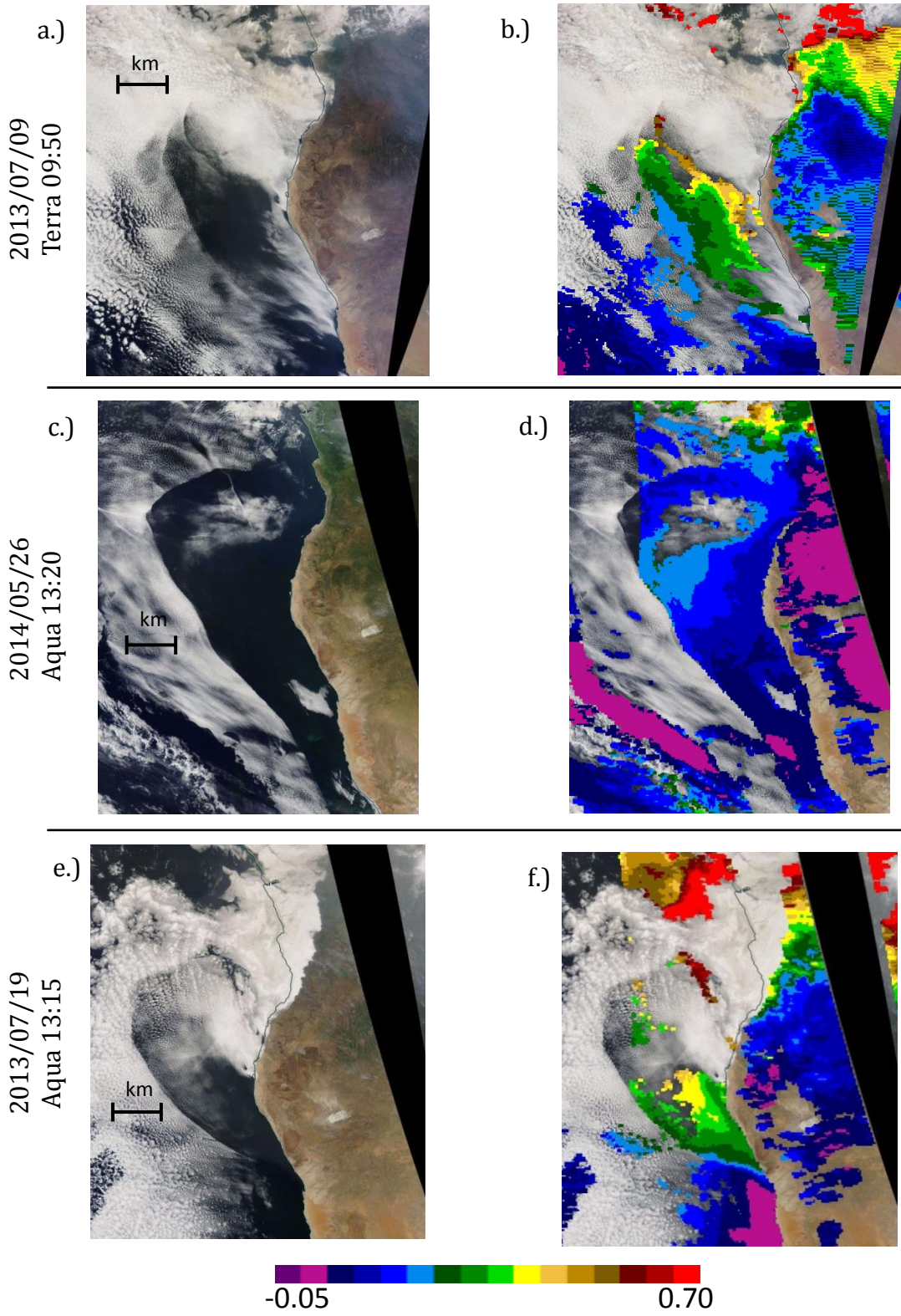


Figure 4.10: MODIS Aqua or Terra corrected reflectance images and aerosol optical depth (AOD). The first column shows just the corrected reflectance, the second column shows the same images as in the first column with the AOD overlaid. Images obtained from NASA's EOSDIS Worldview tool (<https://worldview.earthdata.nasa.gov>).

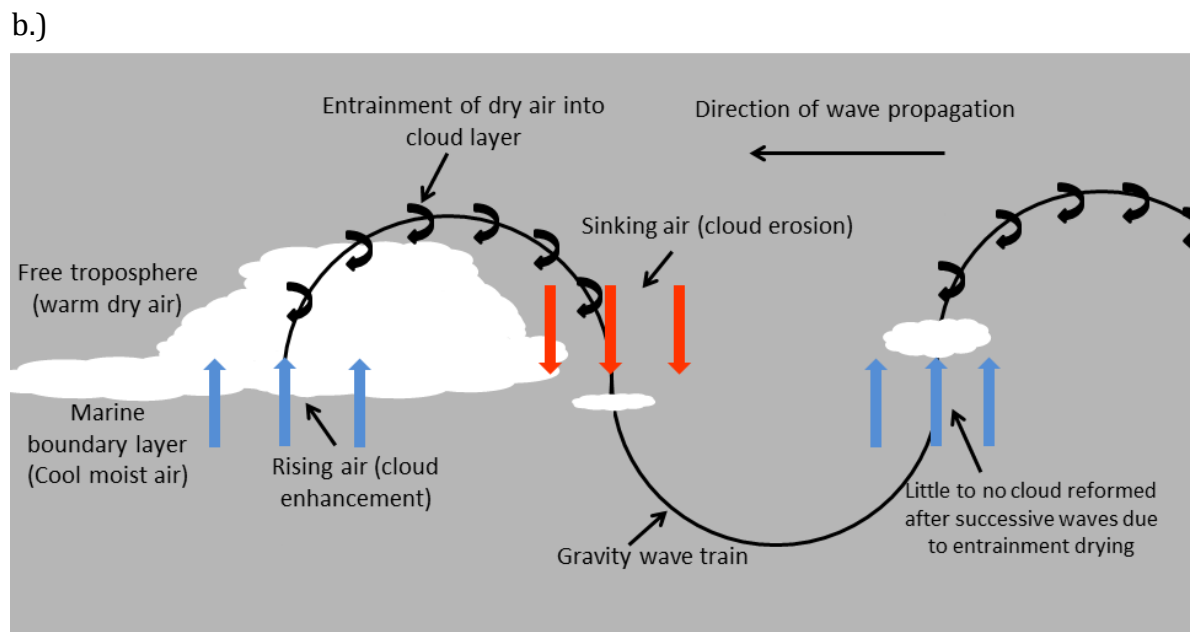
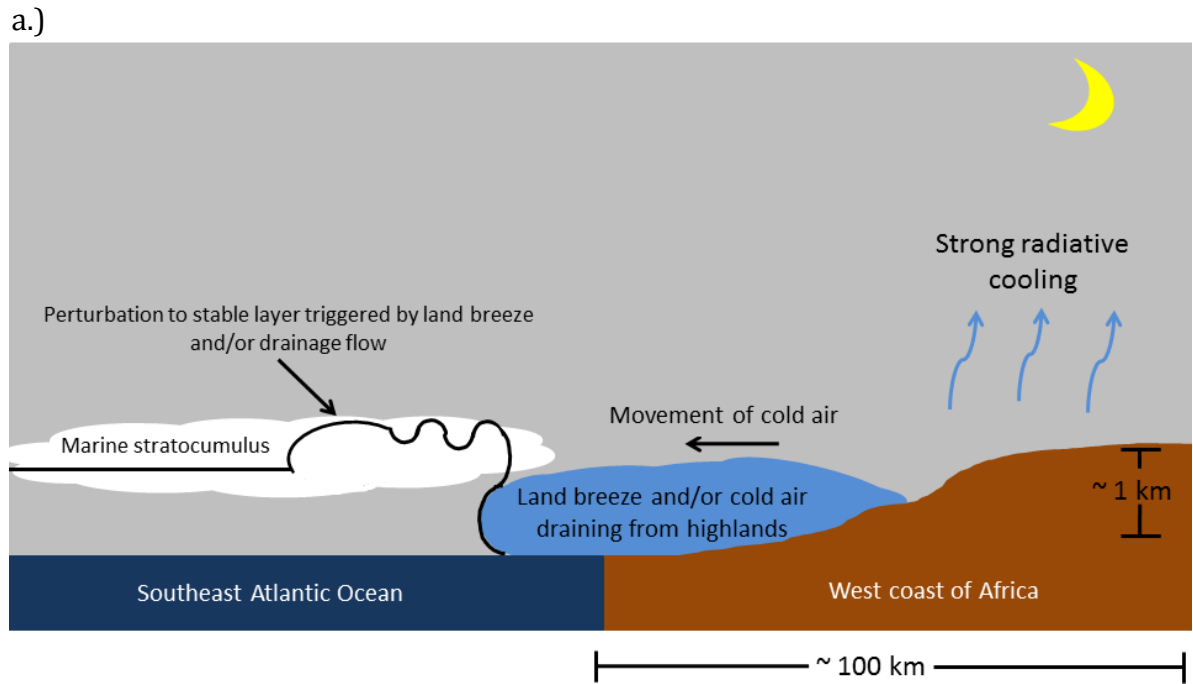


Figure 4.11: (a) Schematic illustration of hypothesized wave-generating mechanism along the African coast. (b) Schematic illustration of a possible cause of cloud erosion associated with the passage of gravity waves.

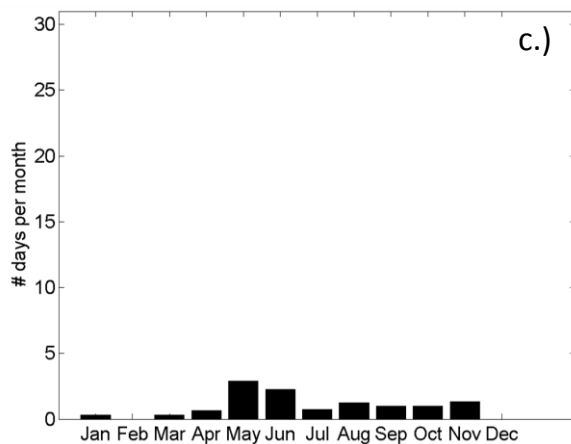
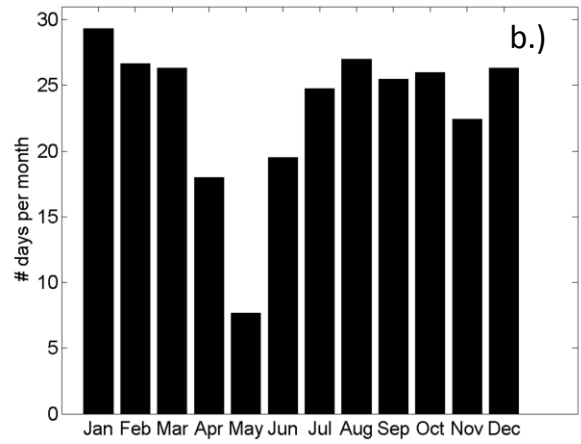
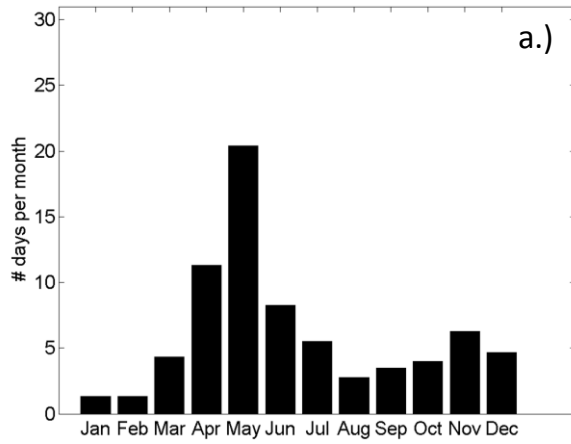


Figure B1: a.) Same as Figure 3.20; the monthly frequency occurrence of days on which cloud boundaries were identified in the cloud boundary climatology ('yes' days; see Section 2.2). b.) As in a, but for the days on which a cloud boundary was not identified in the cloud boundary climatology ('no' days). c.) As in a, but for days on which a determination as to whether a cloud boundary was or was not present was not able to be unambiguously made ('maybe' days).